The Pennsylvania State University
The Graduate School

AURALIZING IMPULSIVE SOUNDS OUTDOORS AMONG BUILDINGS

A Dissertation in
Acoustics
by
Amanda B. Lind

Submitted in Partial Fulfillment
of the Requirements
for the Degree of

Doctor of Philosophy

December 2017

The dissertation of Amanda B. Lind was reviewed and approved* by the following:

Victor W. Sparrow
Professor of Acoustics
Head of the Department of Acoustics
Committee Chair
Dissertation Advisor

Ute Poerschke
Associate Professor of Architecture

David C. Swanson
Associate Professor of Acoustics and Senior Research Associate

Michelle C. Vigeant
Assistant Professor of Acoustics and Architectural Engineering

*Signatures are on file in the Graduate School.

Abstract

Industry partners have identified a market for at least 450 supersonic business jets. Since The Concorde, current legislation prohibits overland supersonic flight, due to the human and environmental impact of the sonic booms generated all along the supersonic flight path.

In the 1970s, new theory relating the cross-sectional area of the aircraft with the sonic boom waveform on the ground was introduced - allowing for next generation supersonic aircraft to be designed with sonic boom mitigation in mind. As such, NASA, the FAA, and industry partners such as Gulfstream, Lockheed Martin, and Cessna have partnered to quantify the human impact of these proposed designs prior to aircraft construction.

The human impact of these next generation sonic booms are predicted through simulation of the Computational Fluid Dynamics (CFD) around the aircraft, non-linear propagation, and propagation through the turbulent boundary layer prior to reaching listeners over infinite level ground. Simulations, and recordings of measured sonic booms are reproduced in sonic boom simulators for subjective testing.

The role of this work is to offer a tool for simulating listenable sonic boom waveforms, a process known as auralization, in more realistic listening environments than infinite level ground.

In order to increase the fidelity and perceived realism of synthesized sonic booms, a model superimposing direct sound, specular reflections and diffracted contributions was implemented. Simulations of sonic booms in various listening environments were performed with this model, and compared against recorded sonic booms. The impact of specular reflections and diffracted contributions on human impact

of sonic booms was quantified with the industry standard PLdB metric.

Finite impulse response (FIR) filters characterizing the listening environment and source/receiver orientation are generated using the image source method (ISM) and a time domain edge diffraction model by Biot, Tolstoy, and Medwin (BTM). Using the software tool provided in this work, the generation of an FIR filter predicting specular reflections may be calculated in any planar geometry: reflections from more complicated terrain and structures could be approximated by thoughtfully created planar geometries.

The ray based Image Source Method (ISM), common to architectural acoustics, was adapted for outdoor applications and sonic boom excitations. Accounting for reflections from the ground and vertical structures was shown to dramatically alter subjective loudness metrics.

This work was motivated by two goals:

1. Provide a tool to enable better prediction the impact of specular reflections on PLdB in more complicated geometries. The tool offers a means of improving the fidelity of, and expanding the collection of sonic booms available for subjective listening tests.

2. Identify if and when simulating diffracted contributions is required for accurate PLdB prediction.

More complicated geometries simulated in this body of work have demonstrated that idealized **specular reflections alone** yield a variation in PLdB from -99.3 dB due to complete occlusion, to $+14.2$ dB due to constructive interference and coincident building reflections. These simulations were performed at listener height around a building with an 'L-shaped' foot print, and at ground level around a multi-family residence.

Specular fields simulated around an isolated wall showed excellent for microphone positions that were not occluded from the direct sound. Microphone positions behind occlusions were better modeled through an edge diffraction model.

Analysis of the diffracted impulse responses (IRs) around the isolated wall showed that for receiver positions located closer to the diffracting edges and closer to shadow boundaries exhibited more impulsive diffracted IRs. PLdB is proportional to, and highly dependent on the rise time of the shocks of the sonic boom. The rise time of the boom is decreased when convolved with a less impulsive IR. As such, the diffracted contributions exhibit the high PLdB of the incident wavefront when close to the edge, and/or close to the shadow-zone boundary. Our edge diffraction model greatly improved prediction of sonic boom wave forms and metrics in the shadow zone, exhibiting an error of 14 PLdB. This compares to an error if 93 PLdB when the diffracted model is omitted.

Table of Contents

List of Figures

List of Tables

Acknowledgments

I would like to thank Dr. Sparrow, the The PARTNER Center of Excellence, the FAA, NASA, the Graduate Program in Acoustics, and the Applied Research Laboratory for the opportunity to do this work. Penn State appreciates the sonic boom measurement data provided by NASA.

The opinions expressed in this thesis may not be shared by the FAA, NASA and/or Transport-Canada.

Much appreciation to my committee members Michelle Vigeant, Dave Swanson, Ute Poerschke, and Victor Sparrow. Their support and feedback has been illuminating, and their critique engaging.

Dedication

Dedicated to Mercy Bennie, Alexis Martinez, and Francis Lind.

Thanks to those who offered support, motivation, and refreshment: particularly, Mark Winkel, Angela Chu, Ysiad Ferreiras, Michelle Easter, Isis Anchalee, Eileen Esposito, Matt Goodman, Jesse Levinson, SQ, Akil Davis, Tim Kentley-Klay, Dave Kotch, and Damian Doria.

Chapter 1

Introduction

1.1 Motivation

In light of proposed next generation low amplitude boom (low-boom) supersonic aircraft, blanket restrictions on civilian overland supersonic flight are being reviewed.

The goal of this work, is to increase our understanding of the diffraction of sonic booms around buildings, and to offer a tool to best simulate the effects of the listening environment on a given incident sonic boom waveform. The results include source code, resulting simulations, comparisons to data, as well as documentation of the tool for generating further simulations.

Waveforms output by a sufficiently accurate model would find application in listening tests and utility in predicting surface pressure loading for the calculation of sound transmitted indoors. Such listening tests would provide useful information for the public and policy makers regarding sonic boom perception and possible legislative changes regarding overland supersonic flight.

1.2 Prior Related Work: M.S. Thesis

The implemented specular model (ISM) is based on Image Source Theory, as presented by Mechel [33], but tailored to outdoor applications and planar incident wavefronts. This method is purely specular, diffracted and diffuse energy is omitted. Therefore the model erroneously predicts silence in the shadow zones and discontinuities across shadow boundaries. ISM, and other ray-based approaches are often said to be “high frequency models", accurate down to a cutoff frequency, the wavelength of which is often defined by the smallest facet in the 3D geometry.

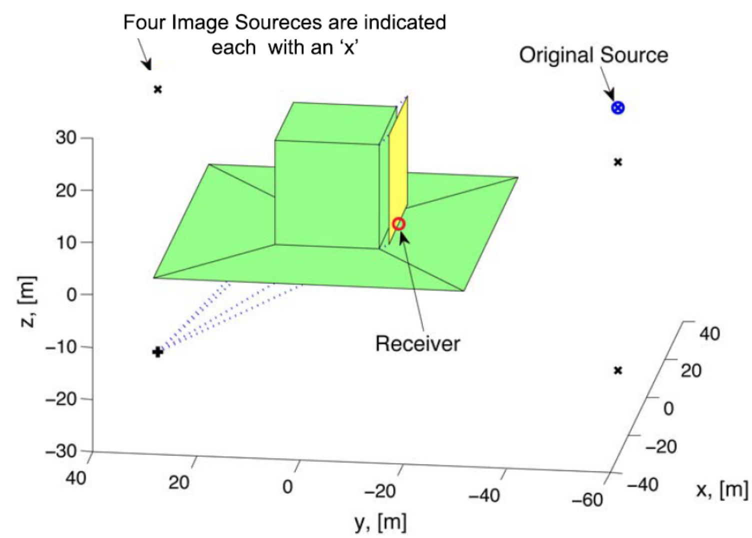

*Figure 1.1: This image illustrates application of the image source model, specifically the last step: the audibility test. Illustrated here is a ray-path which was first reflected on the ground, then reflected again by the rightmost vertical wall. The dotted blue lines outline the **field angle** subtended by the reflecting wall. A plane parallel to the wall including the receiver position is projected. If the receiver point falls within the yellow plane defining the field angle then the image source is flagged as audible.*

Two well known heuristic statements about diffraction:

1. Energy at low frequencies effectively propagates past acoustically small obstacles without reflection or occlusion.

2. The width of the shadow boundary transition is proportional to wavelength.

These observations led to an initial pragmatic approach: each specular reflection was high pass filtered with a frequency roll-off based upon the pressure reflected by a finite disk.[1]

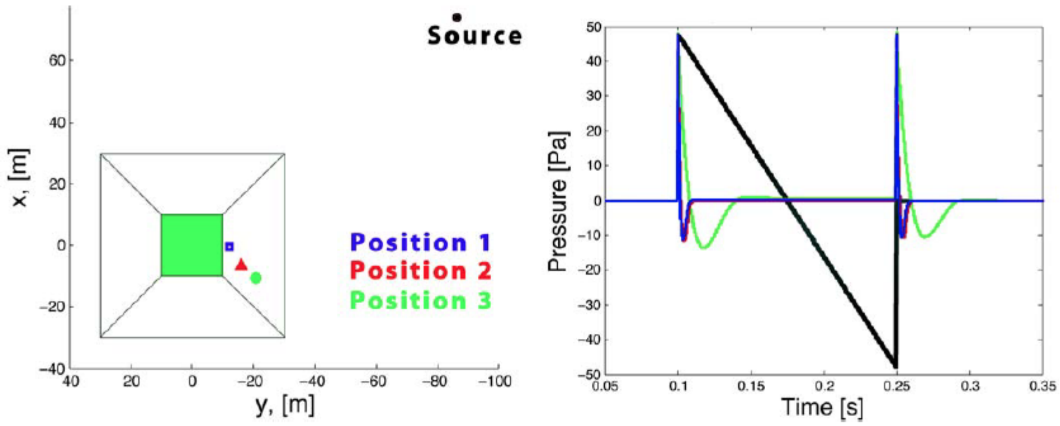

Figure 1.2:
Left: *Top down view of source, geometry, and receiver shown in Fig. 1.1 . The green box represents a large, acoustically rigid, rectangular building on flat ground.*
Right: *N-waves filtered by Minimum Phase High Pass Filter (HPF) with magnitude given by the disc approximation, the Black 'N-Wave' is the idealized incident sonic boom. The red, green, and blue waveforms reflect the predicted frequency content at the three listener positions, prior to application of propagation time delays.*

In order to assess this first approach (ISM + disk approximation), impulse responses were generated for a geometry approximating that of Edwards Airforce base residence instrumented in the 2007 experiment known as HouseVIBES.[2] It was found that when the area of the finite disk was equated with the area of the barrier this approach over-predicted the diffracted field. That is to say, the high pass filter was based upon a reflection from a finite disk, and application to model the effects of the finite size of the reflector was not aggressive enough. It is possible, that a different relationship between the size/aspect ratio/area of the finite reflector to the area of the disk used to model the finite reflector could have been tuned for better agreement. This path however was abandoned, in favor of a semi-analytical model for predicting the diffracted energy presented here in Chapter 4.

This document captures the application of the same ISM Model, now implemented in C++ to enable more realistic geometries. The specular model is combined with the BTM solution for edge diffraction.

The practical implementation of the specular model for a simple rectangular geometry is outlined in detail in the M.S. Thesis [3] available here:

`http://etda.libraries.psu.edu/catalog/10520`

1.3 Scope and Dissertation Structure

This work built on that of the M.S. Thesis. The algorithm written to model specular reflections - optimized for plane waves in outdoor geometries, was translated from Matlab code to C++, enabling simulation of more complicated and more realistic geometries than the box shaped building included in the precurser MS Thesis. These specular reflection simulations are presented in Chapter 3.

In lieu of further exploring the finite disk model as an approximate diffraction, methods developed by Medwin (1980), from the Biot-Tolstoy Approach (1957) were instead employed. This theory and implementation is discussed in depth in Chapter 4. Only first order edge diffraction is implemented in this work. Higher order diffraction requires reframing the semi analytical diffraction solution as a collection of point sources, these diffracted point sources, arranged along the diffracting edge, are then treated like original sources and give rise to additional specular and diffracted and fields. For the purposes of this document, in Chapter 4 we constrain ourselves to calculating the first order diffracted field in a single geometry: the Isolated wall.

The models implemented neglect the following phenomenon:

1. nonlinear propagation,
2. atmospheric refraction and meteorology,
3. diffuse reflections,

4. non-idealized impedance. Realistic impedance is easily incorporated into the ISM model, however acquiring accurate impedance or reflection coefficient values down to 5 Hz was not attempted.

A presentation of data acquired in applicable field tests (Chapter 5), and an assessment of the efficacy of our Specular & Diffracted models in light of the field test data (Chapter 6), illustrate conclusions summarized in Chapter 7. Chapter 8 briefly discusses the software tool used to predict these specular and diffracted fields, in hopes that others will find utility in it's reuse and further development.

This work has utility in increasing the quantity and quality of synthesized outdoor sonic booms for use in subjective listening tests. No such tests are described in the current work.

1.4 Background

In light of proposed next generation low amplitude boom (low-boom) supersonic aircraft, blanket restrictions on civilian overland supersonic flight are being reviewed. These restrictions were instituted in response to the human impact of conventional amplitude sonic booms generated by Concorde and similar first generation Supersonic Transport (SST) vehicles. These early aircraft generated booms exhibiting over-pressures on the order of of 96 Pa (2 pound-force/ft^2); the subsequent legislation may be overly prohibitive for supersonic aircraft designed with the minimization of human impact in mind.

By altering the nose and tail of the aircraft, many shocks can be created. If the many shocks are spaced far enough apart, and if the aircraft is flown closer to the ground, the many shocks do not coalesce into the two discontinuities shown in Fig. 1.3. Fig. 1.4 shows how this canonical shock wave develops during non-linear propagation.

The aim of this work is to contribute to the assessment of the human impact that would result if and when these developing next generation aircraft designs are implemented. Gulfstream Aerospace Corporation predicts a worldwide demand for somewhere between 250 and 450 supersonic business jets (SSBJs).[4] However the operation of supersonic business jets will only be economically feasible if civilian

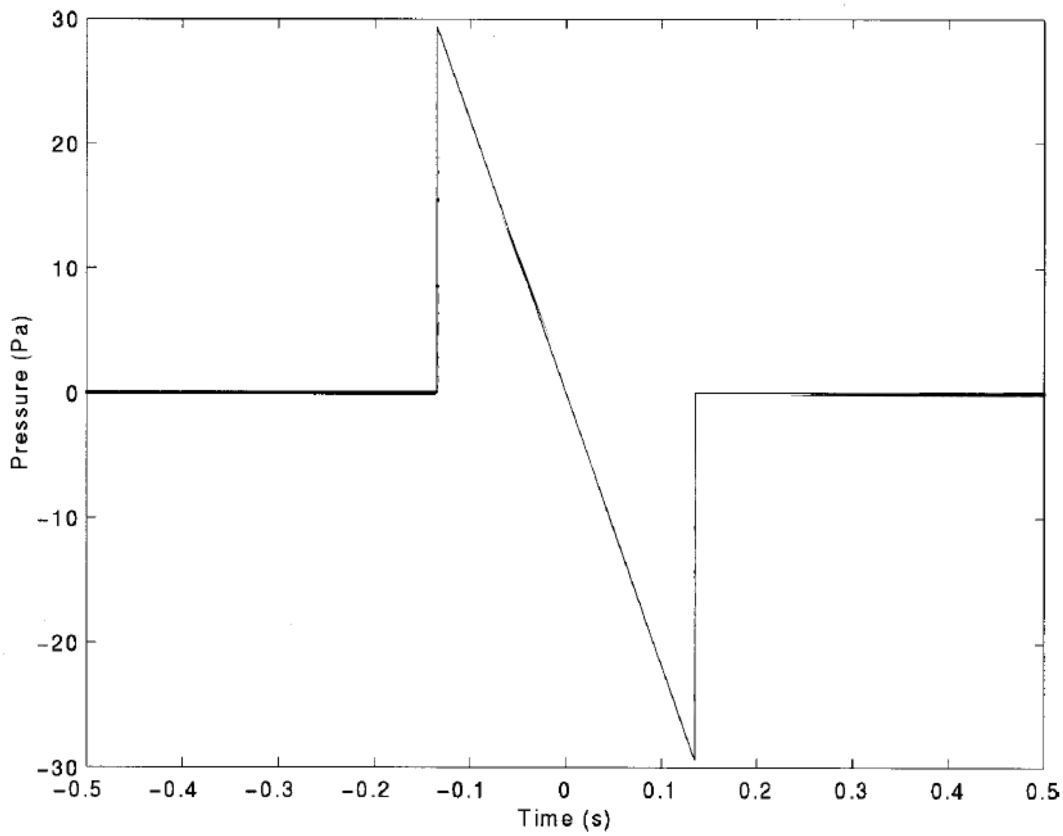

Figure 1.3: Time domain waveform of the computed sonic boom.

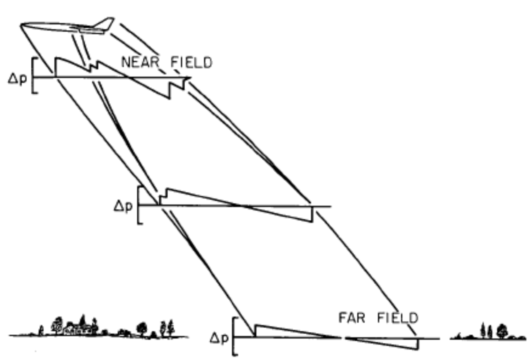

Figure 1.4: Development of the conventional sonic boom waveform through nonlinear propagation, from the first conference on sonic boom research in 1967.

overland supersonic flight is permitted in the United States. In an effort to ensure that policy makers are equipped to make informed decisions regarding these restrictions, four simulators, two constructed by NASA, Gulfstream, and Lockheed Martin are available for use in listening tests. These simulators are capable of faithfully reproducing the high amplitudes and low frequency content present in sonic booms.[5] Since a complete low-boom aircraft has yet to be constructed, recordings of low-boom flyovers are not available for playback.

Although recordings of conventional sonic booms may be reproduced in these simulators, the low-amplitude booms that would be generated by the next iteration of supersonic aircraft are best approximated by two categories of signals:

1. recordings of the low amplitude sonic booms (generated by a conventional supersonic aircraft performing a novel dive maneuver [6]),

2. and synthesized signatures (generated by industry partners based on CFD from novel aircraft design, nonlinear propagation models, and ground reflection models implemented herein).

Synthesized signatures are of particular utility as they may be created for a variety of potential aircraft designs, flight characteristics, and propagation circumstances. What follows is the motivation, and the methods employed, to model and include specular reflections from terrain and structures, as well as post boom noise in synthesized outdoor sonic boom signatures. The aim of this work is to increase the quantity, and improve the fidelity, of synthesized low amplitude outdoor sonic boom signatures available for playback in listening tests. The filters output by the methods described herein provide an incremental improvement to synthesized outdoor sonic booms by including the effects of terrain and buildings by modeling specular reflections and diffraction.

1.4.1 Supersonic Bodies as Sources

The salient features of the source which provide both convenience and complication are the expansive geometry of the sonic boom wavefront, impulsive nature and the abundance of low frequency content. The frequency content of the canonical sonic boom from Fig. 1.3 is shown in Fig. 1.5.

The current work is limited to listener positions directly under the flight path. The under track wavefront may be conveniently approximated as a plane wave, or

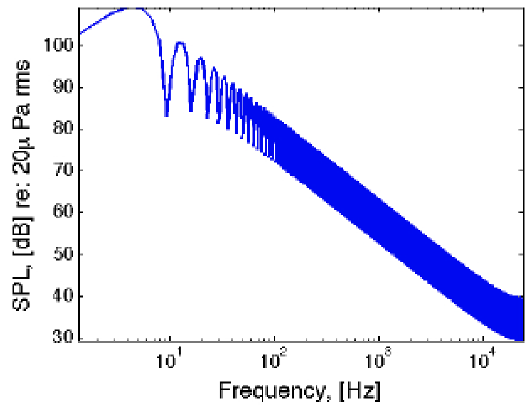

Figure 1.5: Sound Pressure Level (SPL) of a 30 *Pa, 150 ms duration N-wave sonic boom.*

as a distant spherical source.

The impulsive nature of sonic booms requires that multiple contributions should be summed in the time domain to prevent destructive interference between signals which, in-fact, do not overlap in time. Faithfully reproducing the relative delays between the incident waveform and reflections are also of particular significance due to psychoacoustic phenomena such as temporal masking (pre and post) and the precedence effect. If the delay time is less than approximately 32 ms, the level of reflection can be as much as 5 dB higher than that of the primarily sounds without the echo becoming audible.[7]

The high amplitude, low frequency, content of the boom poses unique challenges. Although it is often quoted that the range of human hearing is 20 Hz to 20,000 Hz, the statement only holds for nominal amplitudes. The infrasonic threshold of human hearing does not increase as abruptly as the ultrasonic threshold. Content below 20 Hz may be audible provided the amplitude is high enough.[8] The absence of content below 7 Hz makes no significant impact on the realism of listening tests [5], but faithful prediction of content just above that poses difficulties with regards to scattering and band pass filtering.

The downstream mach angle is $\Theta_{mach} = \sin^{-1}(1/M)$, where M is the Mach number. The elevation of the incident wavefront is then $\theta = 90° - \theta_{mach}$. In the current implementation of the ISM model the source is positioned relative to the receiver such that this incident elevation angle is satisfied. It is assumed that the receiver is directly below the flight path, and that the atmosphere is completely homogeneous, so atmospheric refraction is neglected.

1.4.2 The Assessment of Human Impact of Sonic Booms

The development of military supersonic aircraft and NASA's High Speed Civil Transport (HSCT) program in the 1980s and early 1990s marked a substantial effort towards getting a civilian aircraft capable of acceptable overland supersonic flight off the ground.[9] Employing the NASA Langley simulator, constructed as part of the HSCT program, it was shown that by increasing front-shock rise time and/or decreasing front-shock over-pressure, the subjective loudness of the resulting boom could be reduced.[10] In an effort to quantify this reduction, various measures of subjective loudness, such as A-weighted, C-weighted, and unweighted sound exposure level (SEL), Zwicker Loudness Level (LLZ) and the Steven's Mark VII Perceived Loudness metric (PLdB) were compared with responses to listening tests.

It was shown that PLdB, which is generally proportional to the rise time of the sonic boom signature, is an effective metric to quantify the subjectiveloudness of a variety of outdoor signatures : conventional booms, shaped booms, as well as composite booms (booms consisting of a direct component summed with a single delayed identical reflection).[11] Even in more recent analysis of sonic boom metrics, PLdB continues to be a contender for use in a sonic boom certification requirement.[12] As PLdB is an accurate representation of subjective loudness, the terms will be used synonymously from now on unless explicitly stated otherwise. Although other contributors to the human impact of sonic booms exist, such as startle and rattle, this work is limited to outdoor booms and only has implications regarding perceived loudness.

1.4.2.1 Shaped Boom Program

Recently, with the application of George-Sebass's shaped boom theory in the design of DARPA's Quiet Supersonic Platform (QSP) in 2000, and the successful flight of the Shaped Sonic Boom Demonstrator (SSBD) in 2003, optimism regarding the acceptability of overland supersonic flight has been reinforced. The SSBD, a modified F-5E, exhibited a 'flat top' signature that persisted during propagation through the atmosphere. The SSBD demonstrated that the over-pressure at the ground may be reduced by shaping the aircraft.[13] For more detail regarding the SSBD and the QSP see [14, 15].

1.4.2.2 Synthesized Waveforms

Supersonic aircraft designers can synthesize sonic boom signatures of hypothetical aircraft based on computational fluid dynamics (CFD) and sonic boom propagation codes. Even when care has been taken so that these signatures are appropriate for listening tests, some real world characteristics are typically absent. Specifically the effects of atmospheric turbulence, ground reflections, distortion by structures, and post boom noise. Synthesized waveforms are also typically monaural, lacking the effects of scattering by the human body approximated by the Head Related Transfer Functions (HRTFs).

1.4.3 Perceptual Effects of the Ground Reflection

When an incident wave is superimposed with the wave reflected by rigid ground, constructive and destructive interference occurs.

The significance of a single ground reflection on the subjective loudness of simulated booms was explored via a listening test employing the NASA Langley simulator in 1993.[11] Until this NASA study, typical recordings of sonic booms had been acquired using microphones on the ground: the ground reflection was coincident with the direct component resulting in recorded waveforms with amplitudes that were nearly double that of incident waveform. In order to approximate the ground reflection, it was common practice to double synthesized waveforms for use in listening tests. Sullivan's work illustrated that this oversimplification results in erroneously higher perceived levels.[11]

The study modeled the ground reflection as an exact copy of the free field incident waveform delayed in time. The delay is determined by the receiver height, and incident elevation angle. The PLdB of these composite waveforms are at a

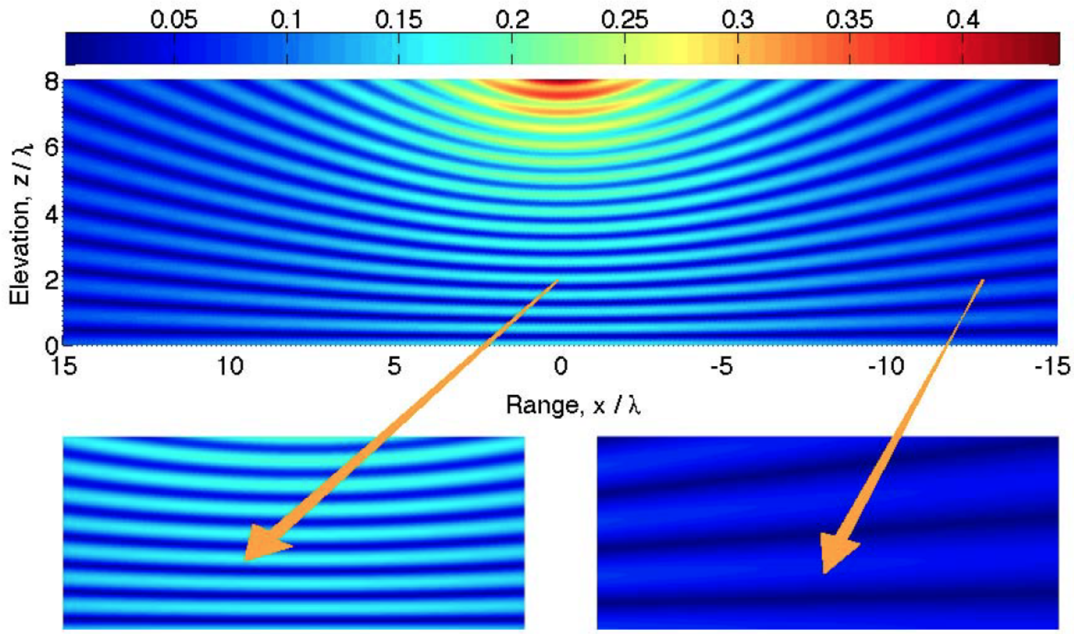

Figure 1.6: Magnitude of the total pressure field generated when a harmonic spherical source, impinges rigid ground. Locations of constructive and destructive interference become further apart with increasing incident elevation angle. The elevation angle of the incident wavefront is $0°$ *in the left inset and is compared to the higher incident angle inset to the right.*

minimum when the delay between direct and reflected components approaches the rise-time of the incident waveform. Under these circumstances the PL of the composite waveforms exhibit attenuation in the range of -4 to -7 dB (depending on incident signature) when compared to composite waveforms using the common practice assumption that the direct and reflected components are identical and coincident.[11]

The approximation for the ground reflection employed by Sullivan is appropriate for illustrating the significance of the delay before the ground reflection, but neglects some finer details about the total waveform that would reach a listener on an impedance plane. Simply summing a direct component with a delayed and identical reflection neglects that the reflection coefficient of the ground is less than unity, frequency dependent, and complex. Since the frequency domain reflection coefficients are complex, accurate locations of constructive and destructive interference depend upon realistic ground impedance. When the ground impedance also varies with incident angle, that is, if the ground is not locally reacting, a possible evanescent contribution from a surface wave may need to be accounted for. Non-locally reacting ground surfaces, for example thick freshly fallen snow, have been demonstrated to occur rarely in nature. [16] For common surfaces however, such as wet or dry turf, it is an accurate assumption that the acoustic impedance of the ground is independent of angle of incidence.

1.4.4 Perceptual Effects of Specular Reflections from Vertical Structures

To date, the effects of vertical structures have not been included in the synthesized outdoor booms played in listening tests. Booms are initially simulated as though the listener is in the free field. As stated above, the ground impedance may then be used to calculate a ground reflection coefficient, thus including the specular reflection from the ground and introducing variability in peak pressure up to +6 dB (depending upon listener position, grade, and incident angle).

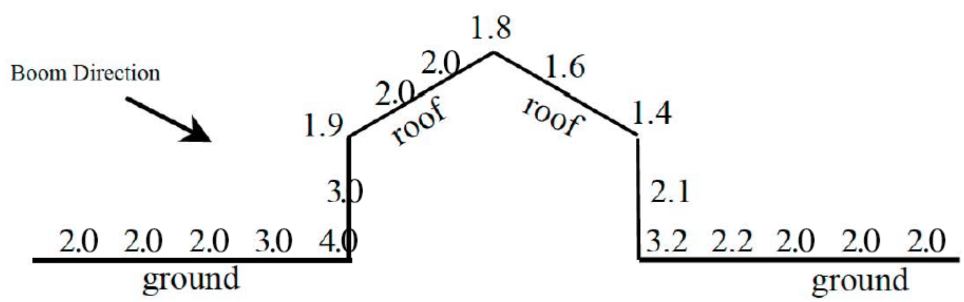

Figure 1.7: Hypothetical amplification of the peak pressure around a single residence. On the side of the structure facing away from wavefront, the ratio of the peak of the total waveform with that of the incident waveform is diminished. Much of the incident energy is occluded by the structure. Only the portion of the incident energy that diffracts around the structure is doubled on the surfaces.

The introduction of vertical structures into our simulated boom listening environment has the potential to introduce variability up to +12 dB depending on geometry, incident angle and listener position. The impact on PLdB may be greater, as it's likely the rise time of the waveform will be impacted. This variability makes room for the generation of a variety of filters, expanding the available database of synthesized outdoor booms and exploring worst case scenarios.

It should be noted that for very large vertical structures, such as the Rocky Mountains, the boom carpet formed by the terrain intersecting the the incident wavefront cone at various heights results in a large variety of peak pressures and varying incident angles across the carpet. This is out of the scope of the current work, however, given the extent of the boom carpet, the incident wavefront may still be locally considered planar (away from the carpet edge). The method presented here would be applicable to predicting a few seconds of specular reflections, even in these environments, as long as the model was supplied with the appropriate incident waveform and wavefront.

1.4.5 Perceptual Effects of Diffraction

The total field given by Mechel's MSM is exact provided that the reflecting surfaces are planar, infinite, and the incident waveform is a plane wave. When the reflecting surfaces are finite, and exhibit geometrical or impedance discontinuities the field predicted by the MSM is also discontinuous.

The edge diffracted contributions sum both constructively and destructively with specular reflections, depending on time and location, and effectively smooth the discontinuities which would be found in the purely specular field.[17]

The second dominant perceptual impact of the diffracted field, is that the pressure behind occluders is more accurately predicted.

The Biot Tolstoy analytical solution for diffraction around wedges, explained by Medwin (BTM) for application to finite edges, has been shown to be an appropriate approach for modeling edge diffraction about structures.[18] The fundamental questions addressed surrounding the perceptual effects of diffraction in this work are:

1. In areas where the direct field is not occluded, does including the diffracted

field impact the rise time of the sonic boon, and thus, is PLdB impacted?

2. In shadow zones, what is the PLdB of the predicted diffracted sonic boom?

These questions are addressed in Chapters 4-7. The code used to validate our BTM model can be found in Appendix A.

1.5 Available Comercial Software

This thesis focuses on an outdoor propagation problem - the impulsive nature of sonic boom waveforms, and the importance of capturing the rise time for accurate perceptual metrics necessitates a time-accurate solution. The desire for a time-accurate outdoor propagation solution is not common. In the acoustic consulting industry, outdoor problems typically involve generators, condensers, and fans, that are continuous sources. In these cases, in consulting applications, the Maekawa curves find use.[19]

Before proceeding with presentations of my own simulations, I'd like to highlight some available commercial solutions.

1.5.1 CATT Acoustic

CATT Acoustic finds frequent use in modeling indoor spaces, and includes options for modeling outdoor spaces, as well as barrier focused indoor problems, such as rows of cubicles.

Despite this published functionality, CATT (v9) has the following limitations with regards to this application:

1. The software tool [20] find great utility in auralization of performance spaces, but is typically not trusted above 8 kHz. When diffraction modeling is implemented, the low frequencies are unrealistically amplified, this fact is at informally acknowledged by it's authors, who offer a high pass filter which is to be applied to its output auralizations in practical application. The high pass filter compensates for the over-predicted diffracted field.

2. One of the largest detractors from the use of CATT acoustics is that the code is not easily parallelizable. Due to superposition, geometrical acoustic models are prime candidates for parallel processing. In order to compensate for needing to run the entire simulation in a single thread, the number of rays is in practice reduced below what theory suggests.

3. Lastly, CATT acoustics approximates edge diffraction by generating diffuse rays if an incident ray strikes within a wavelength of an edge, and turns off diffracted contributions if one face has a high absorption coefficient. Neither of these approaches reflect the underlying physics.

1.5.2 ODEON

Odeon 11 (the current version at the time of this publication being Version 14) [21] offered a radio button which allows inclusion of "Screen Diffraction". Odeon reports that the model implemented implemented is that which was presented by Allan D. Pierce.[22]

This model assumes a continuous wave excitation and is thus not appropriate for our application, due to the impulsive nature of the sonic boom source excitation.

1.5.3 Motivation & Goals Summary

Industry partners have identified a market for at least 450 supersonic business jets. Since The Concord, current legislation outlaws overland supersonic flight, due to the human and environmental impact of the sonic booms generated all along the supersonic flight path. In the 1970s, new theory relating the cross-sectional area of the aircraft with the sonic boom waveform on the ground was introduced - allowing for next generation supersonic aircraft to be designed with sonic boom mitigation in mind. These circumstances have opened the door to a whole suite of research questions. Those addressed in this work are as follows:

1. Provide a tool to enable better prediction the impact of specular reflections on PLdB in more complicated geometries. The tool able offers a means

of improving the fidelity of, and expanding the collection of sonic booms available for subjective listening tests.

2. Identify if and when simulating diffracted contributions is required for accurate PLdB prediction.

Chapter 2

Analytical, Wave Eq. Based & Decompositional Approaches

This Chapter begins with an exploration of canonical scattering problems, scattering by a rigid sphere (Section 2.1.1), and reflection by a finite disk (Section 2.1.2). These two analytical expressions allow us to build an intuition surrounding how large planar wavefronts (like that of a sonic boom) interact with obstacles.

As we understand scattering among acoustically large, and acoustically small obstacles, we begin to distinguish what is captured in the wave equation, but lost in ray based models (often referred to as geometrical acoustics models), as well as where ray based models perform well and offer computational tractability.

Next, in Section 2.1.2, we mention simplified ways to compensate for wave-like low frequency behavior, and inaccuracies of ray based/specular models without rigorously calculating diffracted components.

After briefly mentioning wave equation based approaches, and distinguishing impulsive and continuous sources, we introduce the decompositional approach employed in this thesis: calculating the diffracted field with a semi analytical model, and then combining it with the specular solution via superposition.

2.1 Analytical Scattering Solutions

2.1.1 Plane Wave Scattering by a Sphere

Recall that the general form of an analytical scattering solution is that the total field is equal to the incident field plus the scattered field, as is given by Eq. 2.1 .

$$p_t = p_i + p_s \tag{2.1}$$

The incident plane wave is described in Eq. 2.2 below, first in cylindrical coordinates, and then expressed as the sum of spherical harmonics.

$$p_i(r,\phi) = e^{-jk_0 r \cdot \cos\phi} = \sum_{m \geq 0} (2m+1)(-j)^m \cdot P_m(\cos\phi) \cdot j_m(k_0 r) \tag{2.2}$$

The scattered wave has been shown [23] to take the following form:

$$p_s(r,\phi) = \sum_{m \geq 0} D_m \cdot (2m+1)(-j)^m \cdot P_m(\cos\phi) \cdot h_m^{(2)}(k_0 r) \tag{2.3}$$

where $P_m(z)$ is the Legendre polynomial, $j_m(z)$ is the spherical Bessel function, and $h_m^{(2)}(k_0 r)$ is the spherical Hankel function of the second kind.

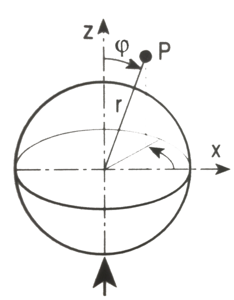

Figure 2.1: The arrow below the sphere indicates the arrival direction of the incident wavefront, and P is the field point where pressure is evaluated, and is located at spherical coordinates $[r, \phi, \theta]$, but independent of θ.

$$D_m = -\frac{(-jG + m/k_0 a)j_m - j_{m+1}}{(-jG + m/k_0 a)h_m - h_{m+1}} \tag{2.4}$$

Where G is the surface admittance, if Z is the impedance, R the resistance and X the reactance: $Z = 1/G = R + jX$. h_m is the Hankel function of the first kind.

For the sake of the calculations and illustrations below, the amplitude of the plane wave is 1 [Pa], and the receiver is $10,000$ Hz from the center of the scattering sphere. Note that the solution to the expression above is accurate in both the near and far field. A far field assumption is imposed if we assume the asymptotic approximation of the Hankel function.

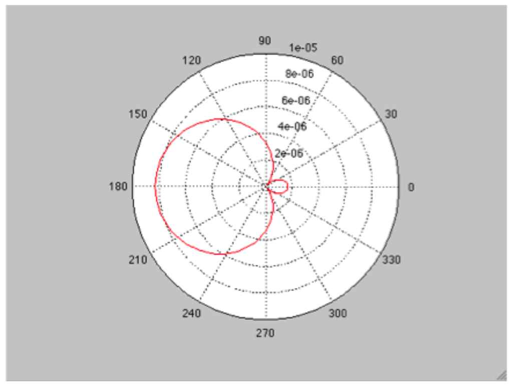

Figure 2.2: $ka = .1$, if $a = 10$ Hz then $f = 5.3$ Hz, A small ka means low frequencies and acoustically small objects. As such, the wavefront passes through the object, almost as though the occluding obstacle is not present. The scattered field is dominated by forward-scatter. Note: the incident wavefront is approaching from $0°$, contrary to Fig. 2.1

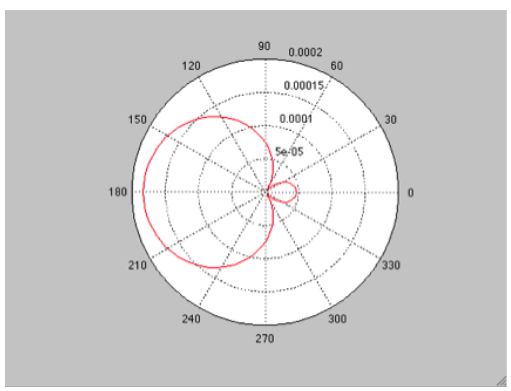

Figure 2.3: $ka = .5$, if $a = 10$ Hz, $f = 27$ Hz Note: the wavefront is approaching from $0°$, contrary to Fig. 2.1 .

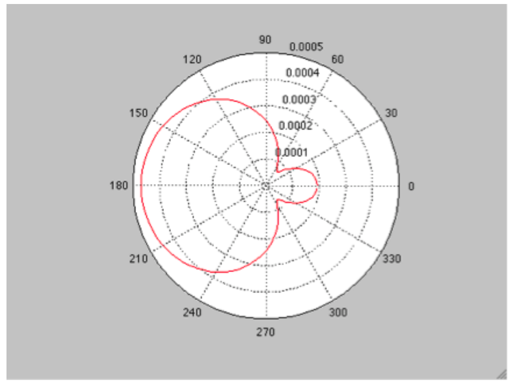

Figure 2.4: $ka = 1$, if $a = 10$ Hz then $f = 53$ Hz Note: the wavefront is approaching from $0°$, contrary to Fig. 2.1.

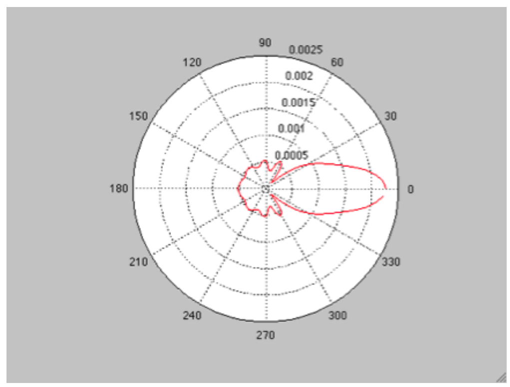

Figure 2.5: $ka = 6$, if $a = 10$ Hz then $f = 323$ Hz Note: the wavefront is approaching from $0°$, contrary to Fig. 2.1

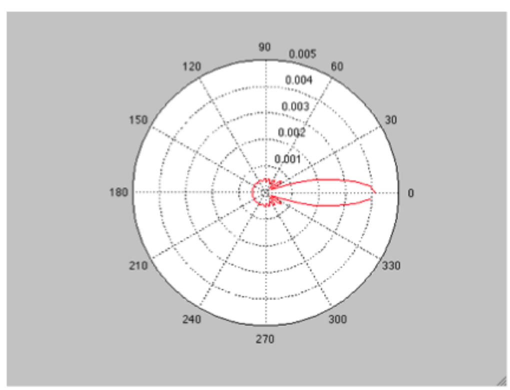

Figure 2.6: $ka = 10$, if $a = 10$ Hz then $f = 538$ Hz. A large ka expresses high frequencies and acoustically large obstacles. As such, the wavefront reflects off the object, approaching specularity. The scattered field is dominated by back scatter. Note: the incident wavefront is approaching from $0°$, contrary to Fig. 2.1

2.1.2 Reflection from a Finite Disk

When combining a wave based low frequency model and a high frequency geometrical acoustic model:

1. If both models possess an overlap in their range of validity in the frequency domain,
2. and most planes in the ISM model are of comparable size,
3. as long as the magnitude response of both the high pass and low pass filters sum to unity,

then the roll-off at the transition should not be so critical.

When condition 1 above is not met, more computation time should be for the low frequency model - extending it's range. The less desirable solution is that the geometry for the high frequency model would be simplified, and more diffusion should be included to compensate for the smaller scale geometries that are omitted.

When condition 2 is not met there are two potential solutions. The first solution implements a different geometrical acoustics model for different frequency ranges. While it could be automated, this approach is currently labor intensive, and has not been widely implemented or validated.

A more practical solution for when reflecting surfaces vary widely, is to define the cutoff frequency for each reflection automatically, based on the dimensions of the reflector, and to use a lower cutoff frequency for the entire geometrical model. Each reflection posses it's own High Pass Filter (HPF), defined by the smallest plane involved in the generation of that reflection.

When implementing the latter approach, the cutoff frequency alone is not sufficient - the roll off of the high pass filter becomes significant: a resource that approximates the frequency content of a specular reflection from a finite surface was needed. Basing the frequency content of each reflection on a physical model eliminated the problem of ringing associated with the steep roll-off employed to satisfy the valid frequency range of the model in previous work.

It is notable, that while this approach improves the physical accuracy of the reflected frequency content, the diffracted low frequency content is still neglected, and would ideally be addressed by the low frequency wave based model.

The analytical solution for the frequency content of an on axis specular reflection from a finite disk was chosen to approximate the frequency content of a specular reflection from a finite plane, and is given [29] by:

$$|p|^2 = p_{max}^2 \sin^2\left(\frac{ka^2}{2\breve{R}}\right), \qquad \text{where} \qquad \frac{1}{\breve{R}} = \frac{1}{2}\left(\frac{1}{d_{s,o}} + \frac{1}{d_{o,r}}\right), \tag{2.5}$$

Since $d_{s,o}$ and $d_{o,r}$ are the distances from the point of specular reflection on the disk to the source and receiver, $\breve{R}$ reduces to $2d_{o,r}$ for plane wave incidence. Again, as the receiver moves away from the surface, the cut-off frequency increases, and less low frequency content is heard at the receiver.

If we take p_{max} to be unity for every frequency by assuming pressure doubling on the surface, then $|p|/p_{max}$ serves as the transfer function between the pressure reflected from an infinite rigid plane, to that reflected by a finite rigid disk. This approximation neglects the possibility that the reflecting plane is tilted relative to the incident plane wave.

The initial increase in $|p|/p_{max}$ with frequency is due to the fact that low frequencies pass the disk undisturbed and without reflection. From another perspective, the roll off at low frequencies is due to destructive interference from the diffracted contribution.

X is the non-dimensional frequency, $X = a(k/2\breve{R})$. In Fig 2.7, as X increases, the nulls in the reflected pressure capture interference of the incident and reflected waves. Since the phenomenon of destructive interference is already represented by the positions of the image sources, when modeling the frequency content of a

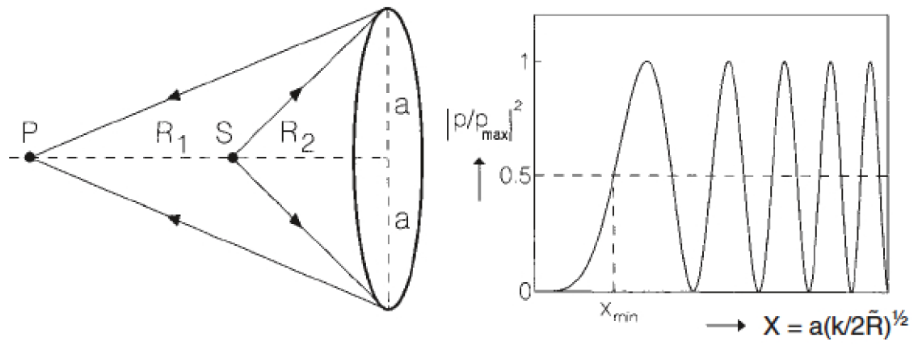

Figure 2.7: The power reflection coefficient for a reflection from a rigid disk as given by Eq. 2.5 (left) geometry (S = point source, P = listening point), (right) normalized amplitude of the pressure of reflected wave squared. [29]

singular specular reflection, oscillations above the initial peak are set to unity, as shown in the desired magnitude response for the high pass filters shown below.

A minimum phase FIR filter was chosen to realize the magnitude responses. The minimum phase $\angle H(e^{j\omega})$ was calculated from the magnitude response $H(e^{j\omega})$ with the following expression, given by [34] [35]:

$$\angle H(e^{j\omega}) = -\frac{1}{2\pi}\int_{-\pi}^{\pi} \log\left|H(e^{j\phi})\right| \cot\left(\frac{\omega-\phi}{2}\right) d\phi \tag{2.6}$$

The code for this calculation, an integration across dummy variable ϕ for each frequency bin, is given in Appendix B and Appendix C.

2.1.3 Finite Reflecting Surface Cut-Off Frequency: ISO Standard 9613-2 (1996 Edition)

This section describes the bandwidth limitations of ray based models and geometrical acoustics models, and associated relationships.

The guiding principle of geometrical acoustics is that it is only applicable when wavelength is much much smaller than the dimensions of the reflecting plane. The question that arises is: How much is smaller than a wavelength is much much smaller? ISO Standard 9613-2 [59] addresses this point and requires that the lowest specularly reflected frequency obey:

$$1/\lambda = \left[\frac{2}{(l_{min}\cos\theta)^2}\right]\left[\frac{d_{s,o}d_{o_r}}{d_{s,o}+d_{o,r}}\right] \tag{2.7}$$

where l_{min} is the smallest dimension of the reflection plane and $d_{s,o}$ and $d_{o,r}$ are the distances from the point of specular reflection on the plane to the source, and receiver, respectively.

An intuitive description of this behavior would be to say, that the further either the source or receiver are from the point of specular reflection, the larger the finite reflector needs to be for the same frequency content. The angle between the incident ray and the surface normal, θ, is the angle between the incident ray and the surface normal. As θ approaches grazing, the size of the reflector needs to become larger for the reflection to retain the same frequency content.

Equation 2.7, which captures the valid frequency range for geometrical acoustic models is written for spherically spreading point sources/receivers. Modification for application to plane waves may be achieved by applying L'hôpital's rule. For a plane wave $d_{s,o}$ goes to infinity, and Eq. 2.7, reduces to:

$$1/\lambda = \left[\frac{2}{(l_{min}\cos\theta)^2}\right] d_{o,r}. \tag{2.8}$$

Again, the cut-off frequency increases with distance from the reflector and for near grazing incidence.

2.2 Numerical Wave Eq. Based Approaches

One may solve for the pressure field at various locations in an ensonified geometry by using wave based solutions such as

1. Finite Element Method (FEM, also known as Finite Element Analysis or FEA),
2. Finite Difference Time Domain solutions (FDTD),
3. and Boundary Element Methods (BEM).

These wave equation based solutions can be applied to curved surfaces, textured surfaces, and surfaces of finite impedance - provided a fine enough lattice or surface mesh. Wave equation based solutions capture diffraction phenomena without extra consideration.

Both FEM and FDTD solve for the time domain pressure waveform at every point in the domain. FDTD marches the wavefront through the geometry calculating the time domain waveform at every point in the mesh. BEM typically calculates the spectra at a given field point by integrating over boundaries.

2.2.1 Finite Reflecting Surface: Boundary Element Method Study

As mentioned in Section 2.2, time domain boundary element method is another time accurate approach to solving the wave equation. Though it can still become computationally unwieldy for large domains, or closed volume domains, it offers some insight regarding the expected scattered time domain waveform from a single finite reflector.

Fig. 2.8, was given by Rendall Torres, and is an Illustration of the impulse response when both a source and receiver are oriented directly above a finite reflector. This image was generated using a BEM simulation solving the KHIE and using the Kirchhoff Approximation. The IR illustrates the specularly reflected impulse, as well as the edge diffracted portion, arriving later. [17] The Kirchhoff Approximation is defined in the glossary in Section 4.1.2..

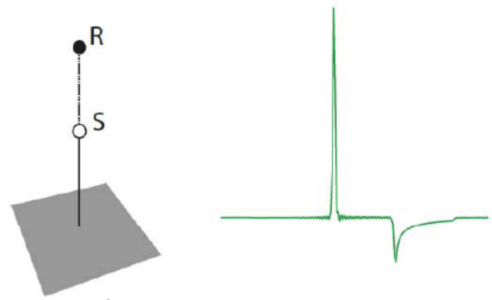

Figure 2.8: Time domain boundary element method solution for a point source reflection from a finite plane, reproduced from [17]

2.2.2 Continuous Wave Sources

Let's briefly compare the most common wave equation based methods, in the context of calculating fields arising from continuous wave, time harmonic sources.

All other things kept equal (geometry size, mesh density & accurate bandwidth of the solution), BEM is the fastest solution as it is not necessary to make calculations for every point in the geometry in order to calculate the resulting pressure at a single field point. Both FEM and FDTD require a volumetric mesh, where BEM only requires that boundaries and the field point of interest be discretized. As such, the FEM and FDTD method require more memory storage and are often more computationally intensive. If the effects of refraction and any non-linearity arising due to focusing are negligible, BEM is offers computational efficiency over FDTD and FEM without a loss of accuracy. BEM is limited, however, in that it is most commonly solved in the frequency domain. Wave equation based solutions in the frequency domain assumes that the source is continuous - as result BEM is not easily applicable for impulsive sources.

2.2.3 Impulsive Sources & Time Domain Accuracy

In this study, the simulated waveforms are intended for human listening, and the sources are impulsive. These requirements limit us to time domain accurate approaches. In frequency domain models, all contributions to a field point are assumed to interfere with each other. If the source excitation is impulsive, it's quite likely that that various arrivals aren't coincident in time and don't have the opportunity to interfere. In such a circumstance a time domain model is required. FEM can be calculated in both the time and frequency domains, whereas BEM is most commonly calculated in the frequency domain.

> "Although the time-domain BEM exists, its application to real-world problems is scarce and the limited amount of accessible literature on this topic makes it challenging to apply it to problems with realistic 3-D geometries like houses. The FDTD approach requires only a single run to obtain the desired time-domain result, making it a more attractive option." [30] [31]

While both FEM and FDTD are time domain accurate, FDTD algorithms are most easily adapted to new geometries. As such, FDTD was selected by Cho when approaching the task of auralizing sonic booms among buildings via a wave based approach.[31] Even with a powerful cluster, computational limitations limited the bandwidth of Cho's implementation to frequencies below 400 Hz. As such, a hybrid approach, incorporating a ray traced hybrid solution provided by Riegel [74] to predict the high frequency content, was required.

As we mentioned, FDTD, the most tractable wave based solution for this application required too dense a mesh for accuracy above 400 Hz. Cho [31] and Riegel [74] addressed this by filtering the input waveform at approximately 400 Hz, and applying the wave based solution at low frequencies, and ray based solution at high frequencies. An alternative to this hybrid approach, is the family of decompositional approaches described in the following section.

2.3 Decompositional Approach

In the family of decompositional approaches, the acoustic field is often predicted with models for separate phenomena - specular, diffuse, and diffracted. Instead of dividing the simulation based on frequency - and specular vs. wave based regimes, we leverage the fact that diffraction is defined as the portion of the pressure field that is missing in the specular solution. Let us assume the implemented diffraction model is accurate, and sufficiently tractable without too many compromises. By definition, super-imposing the diffracted and specular fields will provide the same solution offered by the wave equation.

While a decompositional approach would ideally also superimpose a model of diffuse reflections, these are outside of the scope of this document. Diffuse reflections are not of immediate interest, given the fairly regular structure of the house and low frequency content of the excitation. It is notable however, that some have adopted the perspective that the diffuse field is approximately the small scale diffracted field, and recent dissertation have documented an attempt at that simulation approach with some success [32].

This thesis addresses the question of whether the diffraction model implemented, when combined with the specular solution, approaches the wave based solution at low frequencies. This question is approached through comparison of the simulation results with experimentally measured results in Chapters 5 and 6.

Chapter 3

Specular Model: Image Source Method (ISM)

3.1 Image Source Model

This section begins with a review of a specular reflection model implemented in Matlab in fulfillment of a M.S. in Acoustics at Penn State [3]. The model, takes the form of a growing tree of image sources calculated via nested 'for' loops. The model was translated into C++ so that simulation of more realistic and complicated geometries was tractable. Specular reflections of three geometries were then calculated using the C++ implementation of the model.

The three geometries input into the model are:

1. A simple wall geometry, (Section 3.2.1)
2. an L shaped building, (Section 3.2.2)
3. and an actual building on Edwards Airforce Base that was instrumented for a NASA field test (Section 3.2.3).

Both the Isolated wall and Blackbird Geometry possessed specific microphone positions corresponding to the experiment. While discussing the simple wall geometry, we go into a bit of detail regarding specific specular reflections at microphone positions in Section 3.2.1.2.

The format of the output files is discussed in 3.2.1.3, with more detail regarding explaining program use and functionality offered in Chapter 8.

3.1.1 Review of Image Source Model

The Mirror Source Model (MSM) presented recently by Mechel has been implemented to determine the arrival times of specular reflections within a planar geometry.[33] The model is based on canonical image source theory. The implementation is described in detail in the accompanying masters thesis [3], but is reviewed here. The masters thesis implemented Mechel's model, adapting it to outdoor geometries with facets that vary widely in size, and applying it to a very simple geometry.

When provided with the following inputs:

1. maximum order of reflection,
2. 3D geometry of boundaries/reflecting surfaces,
3. complex impedances of reflecting surfaces,
4. an incident wavefront direction or sound source position,
5. and listener positions,

the MSM outputs the amplitude and phase of each frequency component in each specular reflection.

Mirror source contributions are then summed in the time domain, this eliminates the assumptions that the source is continuous and make the implementation appropriate for impulsive sources.

The following pages (Fig. 3.1, and 3.2)offer a flowchart for understanding the first order and higher order MSM model, respectively.See the associated M.S. Thesis [3] for images clarifying each portion of the flowchart. Zooming in a digital copy of this flowchart should offer an understanding of the model.

3.1.1.1 First Order Source Calculation Flowchart - View Digitally

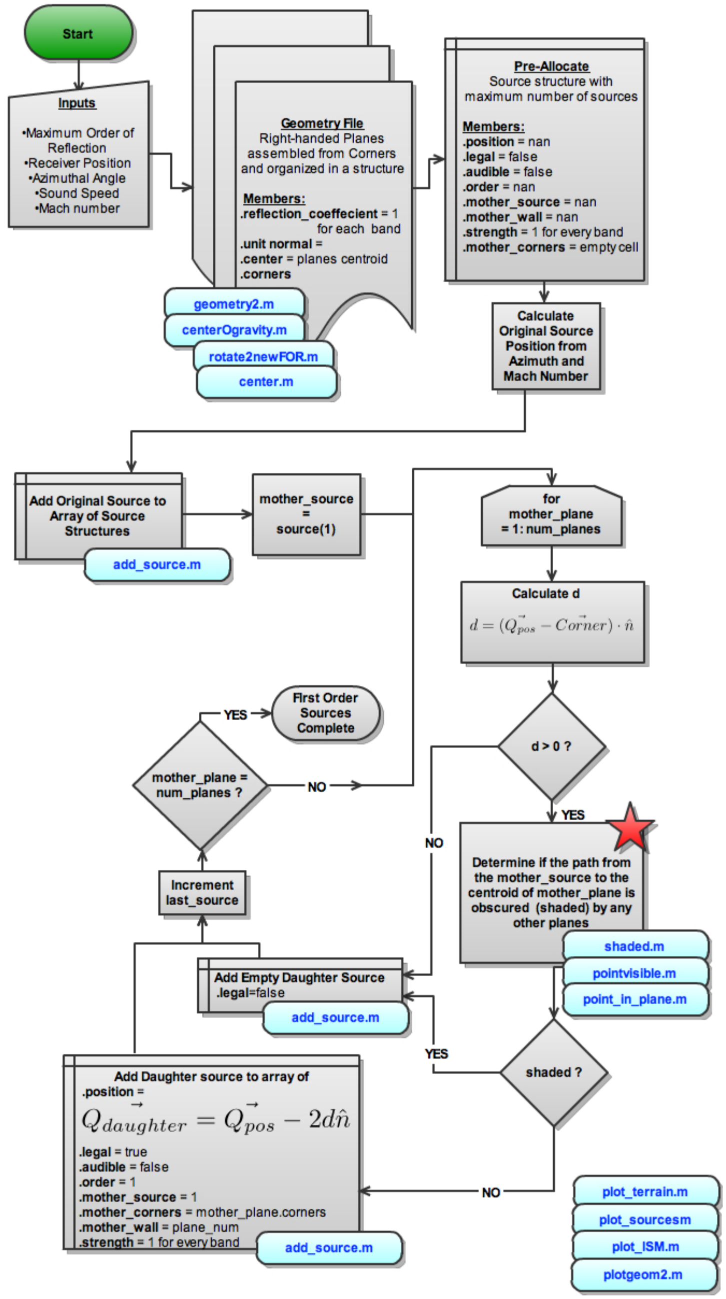

Figure 3.1: $\vec{Q}_{pos}$ is the source position vector. $\hat{n}$ is the surface normal of the reflecting surface. $\vec{Q}_{daughter}$ is the position of the new image source. The sign of d answers the question of "Legality": is the original source on the reflecting side of the surface. The occlusion calculation, shown with the star, is the slowest portion of the algorithm. The occlusion calc tests for validity, and at the end for audibility.

3.1.1.2 Higher Order Source Calculation Flowchart - View Digitally

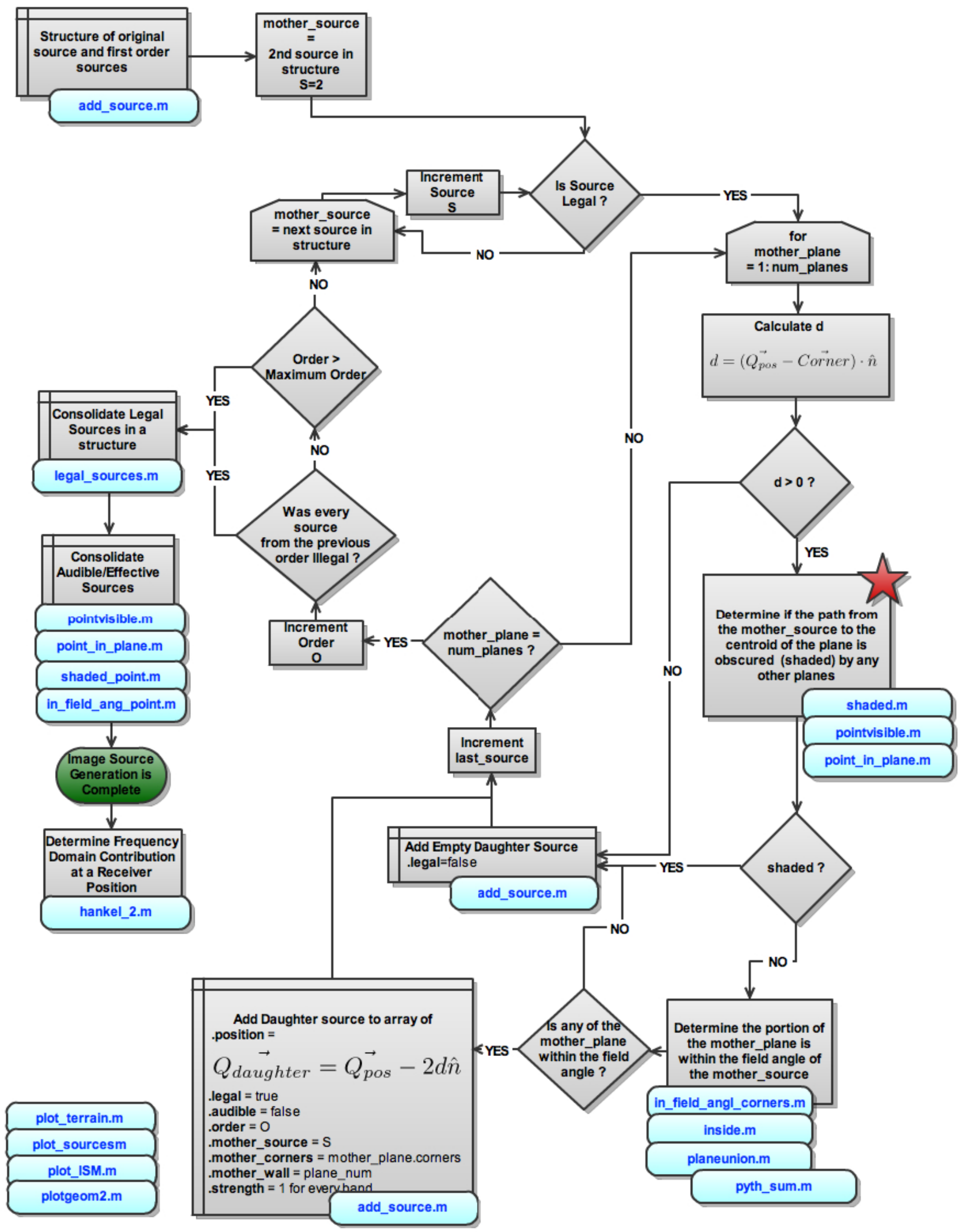

Figure 3.2: $\vec{Q_{pos}}$ is the source position vector. $\hat{n}$ is the surface normal of the reflecting surface. $\vec{Q}_{daughter}$ is the position of the new image source. The sign of d answers the question of "Legality": is the original source on the reflecting side of the surface. The occlusion calculation, shown with the star, is the slowest portion of the algorithm. The occlusion calc tests for validity, and at the end for audibility.

3.1.1.3 Surface Impedance

It should be noted that Mechel's presentation makes no mention of how to handle the finite nature of each plane: the amplitude of each specular reflection provided by the MSM depends ONLY upon the reflection coefficient or impedance of the reflecting planes. Since the impedance of a reflecting surface is typically frequency dependent, each reflection is not simply a scaled replica of the incident time domain waveform, but a filtered replica. It is helpful to think of these reflection coefficients as filters, because then other phenomena that filter each reflect path may be combined with the reflection coefficient filter. Due to the properties of linear time invariant systems, all the phenomena which attenuate a specular reflection, may be accumulated into a single filter via multiplication in the frequency domain. One of the conclusions of the M.S Thesis was that provided the magnitude spectrum of each reflection, that the corresponding phase for that magnitude should be "minimum phase". An approach provided by Damera-Venkata [34] [35] was quite useful for calculating the appropriate phase response.

Details regarding assumptions of locally reacting surfaces and surface impedance models are explored in detail in the M.S. Thesis.[3]

When all reflecting surfaces possess infinite impedance, the impulse response (IR) consists of delayed pulses of unity magnitude. Such is the case with the final output of this implementation of the MSM. In Chapter 5, we compare simulation to experiment, look for alignment of arrivals in the time domain, and comment on what appropriate reflection coefficients might be.

3.1.1.4 Finite Reflecting Surface

Although Mechel did not discuss reflections off finite surfaces, it is known that the image source model is only valid for frequencies with wavelengths smaller than the smallest reflecting plane, in my masters thesis, the question 'how much smaller?' was discussed by drawing from ISO standard 9613-2, as well as modeling specular reflections from finite surfaces, as those reflected by finite disks of comparable size. This was reviewed in this document in Section 2.1.3.

As mentioned above, in the accompanying masters thesis work, we accounted for the limited valid bandwidth of MSM, and the effects of diffraction by using the spectrum for the continuous wave solution for the reflection from a finite disk - filtering spectral content of each reflection. The approach in the work described herein is to calculate the time domain accurate impulse response that is the superposition of an idealized specular reflection and an edge diffraction model. Our intention is to effectively perform the high pass filtering of each reflection, and to solve for the low pass filtered diffracted field in cases of specular occlusion. This is an approach to compensating for the limitations of MSM is detailed in Chapter 4.

3.1.2 Application Specific Considerations

An implementation of Mechel's Mirror Source Method (MSM), an architectural acoustics technique rooted in Image Source Theory [33], is used. The MSM yields the positions of image sources, from which complex amplitudes of individual specular reflections may be calculated and summed.[33] Transforming the sum of the complex amplitudes of each source to the time domain yields a finite impulse response (FIR) filter. This filter may then be applied to sonic boom signatures of arbitrary shape to approximate the total pressure waveform heard among structures and terrain.

3.1.2.1 Large variety of facet sizes for outdoor geometries

When a small facet gives rise to a reflection off a larger facet, the smaller illuminated portion may be stored as it's own reflecting surface. Decisions regarding trade offs of regarding how to manage this growing tree of reflecting surfaces were covered in the M.S. Thesis.[3]

3.1.2.2 Long Propagation Distance

Plane waves are approximated by placing spherical sources very far from the geometry and receiver. Very long propagation distances require an alternative to the procedure described above; one must represent each reflection as a delayed ideal impulse in the time domain, and then filter each impulse so it contains desired frequency content, thus avoiding the calculation of relative phase and the associated round off error. This is addressed in greater detail in the M.S. Thesis.[3]

3.1.2.3 Diffraction

Since the MSM is a ray based geometrical acoustics model, when used alone it is best suited cases when specular reflections dominate, for example early reflections and higher frequencies. Compensation for this limitation by filtering informed by a finite disk, and superposition with diffracted contributions are the core focus of Chapter 2 and Chapter 4.

3.1.2.4 Diffusion and Refraction

For cases dominated by diffuse reflections such as very rough facades, or cases with refractive meteorology, stochastic ray tracing would be a better choice.

3.2 Simulated Specular Fields

In this Section, we will explore simulated specular reflections around three geometries: an isolated wall, an L shaped building, and a multiple family dwelling on Edwards Airforce Base.

Both the isolated wall, and multi-family dwelling geometries simulated below correspond to real building geometries from NASA field tests. The isolated wall geometry is simple enough for human inspection and comparison of each reflection, providing a good opportunity to validate our implementation.

Here we consider simulated specular reflections around an isolated wall in the greatest detail in preparation for comparison with measured data in Chapter 5

3.2.1 Isolated Wall

3.2.1.1 Simulated Geometry

Renderings of the isolated wall simulated are shown in Figs. 3.3 and 3.4. The geometry mimics that of the concrete masonry unit (CMU) wall shown in photographs in Chapter 5, Figs. 5.2, 5.4, 5.7. Seven microphones were placed around the CMU wall, the corresponding microphone locations are shown as red spheres in the renderings. The computation time required to calculate the specular and diffracted impulse responses for these seven receiver positions is less than two seconds, and consumes 15 MB of storage with a sampling rate of 48 kHz.

This and the following sections offer acoustic contouraround the isolated wall and other scattering building geometries. In order to generate these maps, a mesh of listener positions is generated 3.175 [mm] (1/8") and 1.2 [m] above the ground plane. These meshes correspond to potential microphone positions on the ground, and describe the field at listener height. In the interest of faster simulations, despite long span seven microphone locations shown in the renderings, the listener mesh was constrained to the area in close proximity to the wall, as shown in Fig. 3.3.

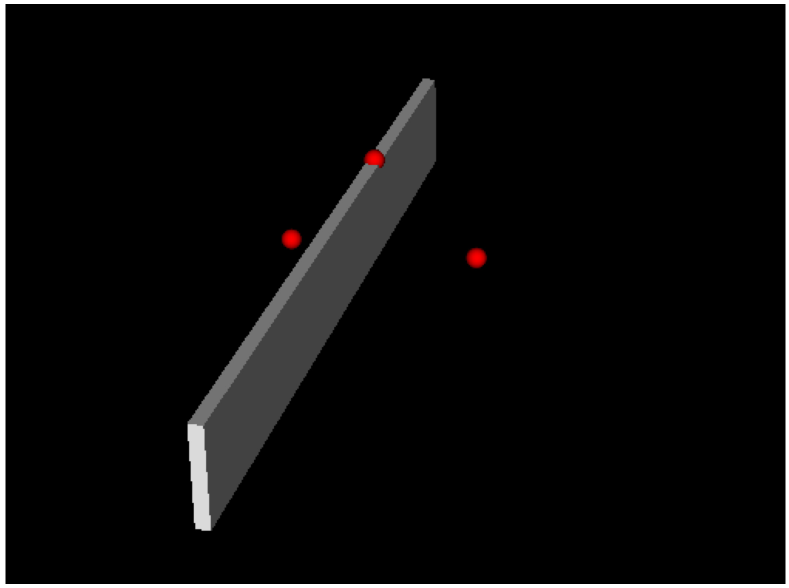

Figure 3.3: Simulated Isolated Wall - microphone positions near the wall, from left to right Microphones 201, 203, 202. Sonic boom is incident from the right. The ground plane is flush with the bottom of the wall, and has been eliminated from the figures for clarity.

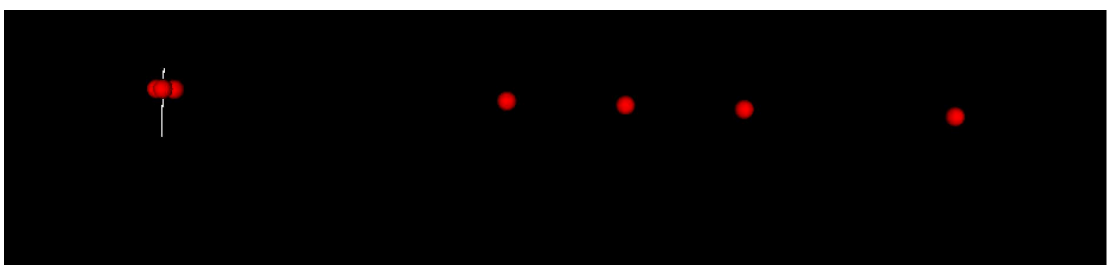

Figure 3.4: Simulated Isolated Wall - shown again from directly above, here are all the microphone positions from the field test. From right to left the microphones are 190, 204, 188, 189 , 202, 203, 201. Microphone 190 was a distant microphone and was approximately 81.08 [m] (266') from the house. Microphones 189, 188, and 204 were approximately 35.31 [m] , 47.37 [m] (115'10", 155'5") and, 59.64 [m] (195'8") from the back wall of the house, respectively. Channels 202 and 201 were approximately 0.91 [m] (3') from the wall on either side. The incident wavefront approaches from the right, and microphones are numbered from right to left in the discussion below

The actual instrumented wall, shown in Chapter 5, Fig. 5.2, is larger than was rendered and simulated. The actual wall bends west, sheltering microphone position 6 (microphone 201, as given in Table 3.1 and shown in Fig. 3.4) from the north. In this paper, we explore only a single actual boom event around the wall, an event with an elevation angle of 20 degrees from grazing. The event has an elevation angle far enough from grazing that - for specular reflection simulation purposes - it's unnecessary include the north masonry unit wall.

3.2.1.2 Simulation Results - Valid and Audible Image Sources

The ISM specular reflection model predicts all the image sources, based on the original source location (or wavefront incident angles), and the scattering geometry. After the growing tree of image sources is pruned based on validity of each image source, the audibility of the valid sources at a particular receiver position is determined. Here we discuss the calculated audible image sources for each microphone location.

Table 3.1: Simulated audible image sources for a single boom event with a corresponding measurement. Impulse responses 0-6 (IR Number) correspond to microphone locations illustrated in Fig. 3.4, and again in the photograph given in Figure 5.4 where their distances from the wall are listed.

IR Number	Mic Number	Audible Image Source IDs
0	190	0, 8
1	204	0, 8
2	188	0, 8
3	189	0, 8
4	202	0, 3, 8, 26
5	203	0, 5
6	201	-

Microphones 0-3 (mics 190, 204, 188, 189 in shown in Fig 3.4) are quite far from the wall, and receive the direct sound and the ground reflection.

IR 4 represents a microphone that sits in the corner formed where the wall and ground meet, facing the original source. That location receives the direct wavefront, the ground reflection, a first order reflection off the wall, and a second order reflection involving both the ground and the wall.

IR number 5 captures the simulated field at the microphone position on top of the wall. In this position, the direct wavefront and the reflection off the top of the wall exist.

IR number 6 is shielded from the direct wavefront by the wall, and does not receive a reflection from the ground, as the ground below it is occluded from incident sound.

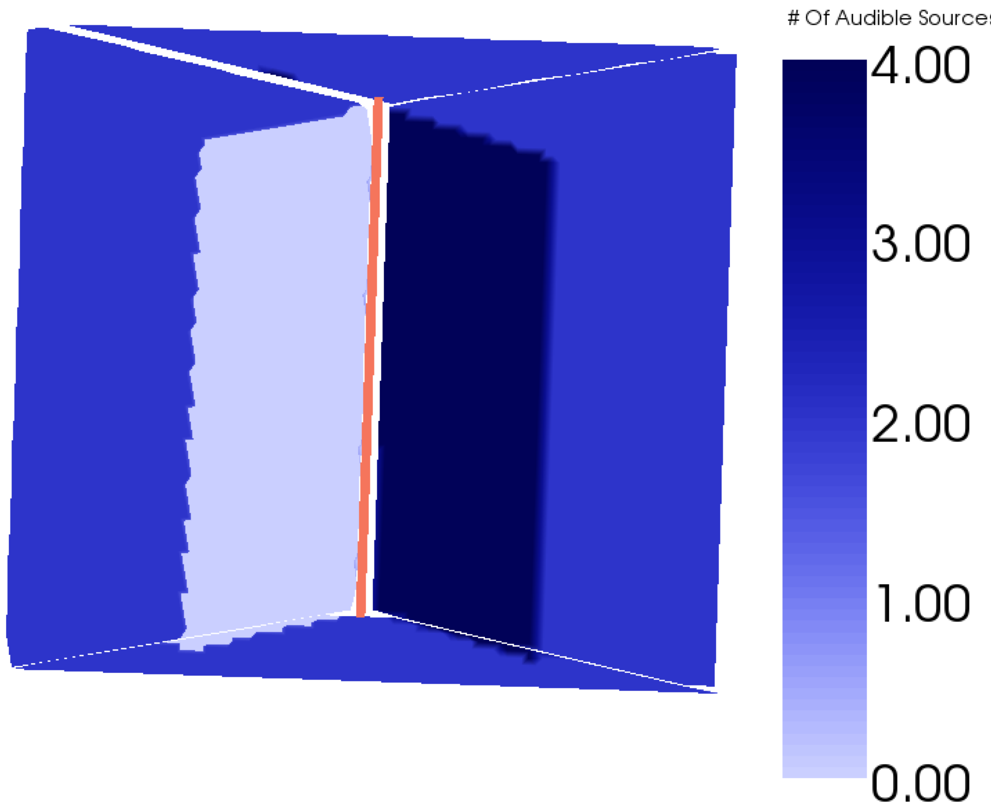

Figure 3.5: For the isolated wall geometry, a carpet of virtual microphones, or field points are placed on a plane 3.175 [mm] (1/8") above the ground. Visualized here are the number of audible image sources, at each field point. The incident angle of the sonic boom corresponds to that of from the experiment described in Chapter 5. For the isolated wall, the resolution of observer points is 10 microphones per meter, distributed in a grid.

Simulating a mesh of listener positions, we are able to render acoustic pressure contours. This heat map visualizes the number of audible image sources around the wall (shown from above, in orange). Images communicating the count of audible sources has been a useful debug tool to ensure the simulation is performing as expected.

3.2.1.3 Simulated IRs - Output Files and Printed Results

Running the application generates many files, the first of which are shown in this figure. The first two files document the simulation. The first file stores valid sources in the geometry, such that audible sources may be calculated for new receiver positions without having to repeat the entire simulation. The second file stores the final wall structure, which lists the original planes as well as plane instances that are generated when a reflection illuminates only part of the surface. The rest of the generated files contain impulse responses for each microphone position in the geometry. An option in the software asserts that ground planes should be subsampled. Surface loading, or the pressure at listener height may be represented with a mesh of virtual microphones. Generation of contours yields many text files, and enables the generation of the pressure contours.

```
Isolated_Wall_sim__1_sources_77.193000 az_20.264000 el.txt
Isolated_Wall_sim__1_walls_77.193000 az_20.264000 el.txt
Isolated_Wall_sim_1_0000000_IR_77.193000_az_20.264000_el_Ppos_81.027410i_-2.829540j_0.003175k.txt
Isolated_Wall_sim_1_0000001_IR_77.193000_az_20.264000_el_Ppos_59.399793i_-2.074286j_0.003175k.txt
Isolated_Wall_sim_1_0000002_IR_77.193000_az_20.264000_el_Ppos_47.215220i_-1.648792j_0.003175k.txt
Isolated_Wall_sim_1_0000003_IR_77.193000_az_20.264000_el_Ppos_35.030647i_-1.223297j_0.003175k.txt
Isolated_Wall_sim_1_0000004_IR_77.193000_az_20.264000_el_Ppos_0.913843i_-0.031912j_0.003175k.txt
Isolated_Wall_sim_1_0000005_IR_77.193000_az_20.264000_el_Ppos_-0.063461i_0.002216j_0.917575k.txt
Isolated_Wall_sim_1_0000006_IR_77.193000_az_20.264000_el_Ppos_-0.913843i_0.031912j_0.003175k.txt
```

Figure 3.6: Shown here are the list of files generated when a simulation including an acoustic pressure contour is run.

While the simulation is running, source and wall information is printed to the screen for debug purposes:

SrcNumber: 9
SrcPosition: 29308.603289 , 6662.516948 , -11096.712366
Order: 1
MotherSource: 0
MotherWall: 8

WallNumber: 8
FloorPlane: 1
NumberCorners: 4

WallCenter: (-65.558147, 1.816370, 0.000000)
WallNormal: (0.000000, 0.000000, 1.000000)
Corners:
CornerInd[12]=(-103.429032, -96.449133, 0.000000)
CornerInd[11]=(-0.297121, -4.869397, 0.000000)
CornerInd[9]=(-0.052461, 2.136733, 0.000000)
CornerInd[15]=(-96.449133, 103.429032, 0.000000)

This printout aids in validation, and reflects some of the data stored in the source and wall structures as the simulation runs.

3.2.1.4 Simulated PLdB/Pmax - Input Waveform

Having generated thousands of impulse responses around the listening environment, the next step in calculating the pressure waveform at each of the virtual microphone locations is convolution with an input waveform. Recorded waveforms from the NASA field test are plotted in figure 5.3.

Many of these microphones are very far from the scattering building, such that they are out of range of the building's affect. While the relationship between the incident waveform at the microphones near the building, and the recording made at the far field microphones is not ideal, it was simplified in the following way:

1. Meteorology was neglected (straight rays were assumed).
2. It was assumed the ground is locally reacting (impedance does not vary with incident angle).
3. The ground is infinitely rigid (2x multiplier of pressure expected at the surface of the ground).
4. The planar wavefront is a good approximation. Conventional sonic boom wavefronts are conical with very large cross-sectional radius at the ground.

Making assumptions the waveform incident at positions 190, 204, 188, 189 should be identical. As may be seen in figure 5.3, they are not identical. While similar, they do vary in maximum pressure (Ranging from 55 dB to 71 dB) and

PLdB (ranging from 95-100 PLdB). Microphone 190 is a bit of an outlier - the other 3 records exhibit perceived loudness between 99 and 100 PLdB.

For the following Pmax and PLdB simulations, the record from microphone 188 was scaled by .5 and used as the input waveform as shown in figure 3.7.

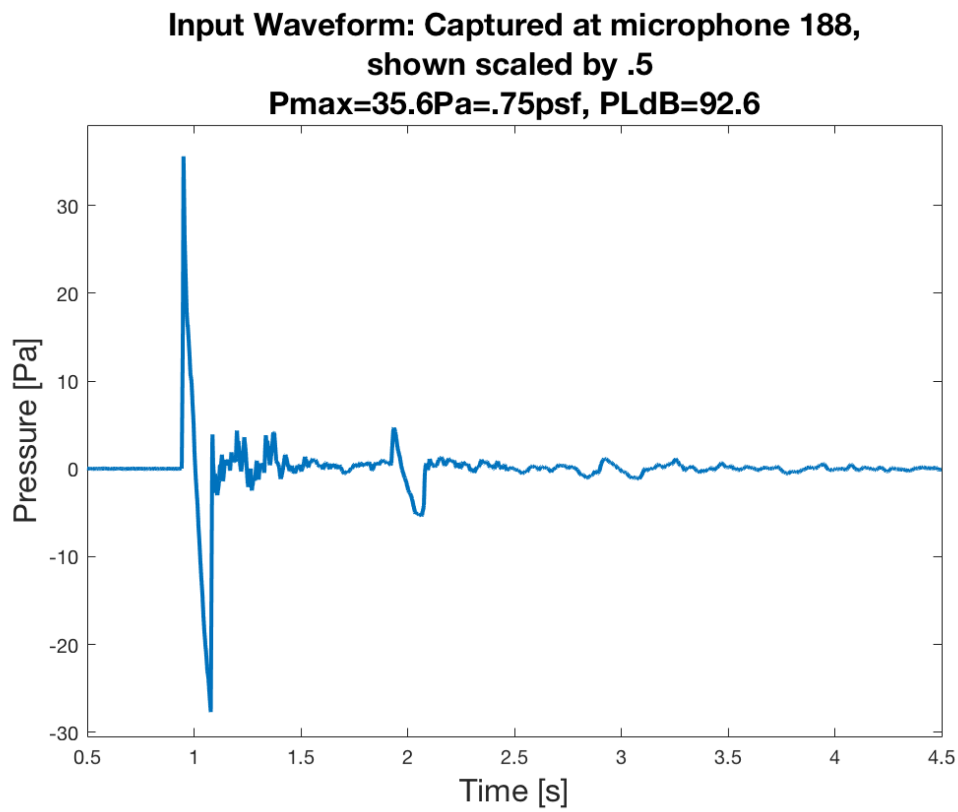

Figure 3.7: Best approximation for the incident waveform, and input waveform used in all the "isolated wall" and "L-shaped building" simulations. This waveform was acquired from microphone 188 as part of the 2006 field test documented in [46]

3.2.1.5 Simulated PLdB/Pmax - Contours

Calculating impulse responses characterizes the source-path-receiver relationship, meaning it captures the effect of the listening environment. But more steps must be taken to identify the perceptual results of the impact of the listening environment. We must next calculate time histories of pressure at each location - given a particular incident sonic boom, and then calculate the perceived loudness of each time history. As discussed in Chapter 1, Perceived loudness (PLdB) is an accurate metric for the perception of sonic booms. Maximum pressure is only offered for code validation and curiosity purposes.

The following Pmax and PLdB contours were generated with the input waveform presented in Section 3.2.1.4.

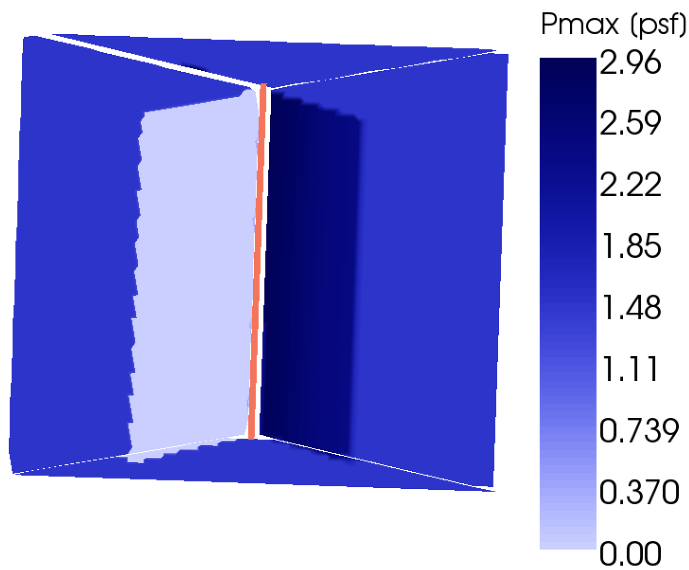

Figure 3.8: This contour illustrates the maximum pressure of the sonic boom waveform measured 3.175 [mm] (1/8") above the ground surface. This heigh was selected as it's the diameter of the smallest microphones tasked with such a measurement, and is likely the radius of the microphone actually used. This close to the ground, the direct and reflected wavefronts are effectively co-incident, and are often modeled with pressure doubling. The incident wavefront approaches from the east (to the right, in this image). Recall, the input maximum pressure was 35.6 *[Pa], or* $35.6 * .021 = .75$ *[psf]. As you can see, no pressure is predicted in the shadow zone, pressure doubling occurs on the ground, and amplification up to pressure quadrupling occurs on the ground in front of the illuminated side of the wall.*

The processing to generate these contours currently occurs in Matlab. The Matlab code reads each impulse response file, performs convolution of the impulse response with the incident sonic boom, and calculates three parameters for each time series (the number of reflections, the maximum pressure, and the PLdB). A contour file for each parameter is generated. The NASA code which calculates the PLdB from the pressure time history was written in Fortran, and was initially offered to us with a Matlab wrapper. The contour file is then read by the C++ application, and visualized as an overlay in the simulation geometry.

The three contours which follow are all representations of the same data. The first contour offers the change in PLdB due to the listening environment, relative to the input waveform. The following two images offer the change in PLdB due to environment, relative to the pressure double waveform. Comparing to the pressure doubled waveform essentially ignores the impact of the ground reflection.

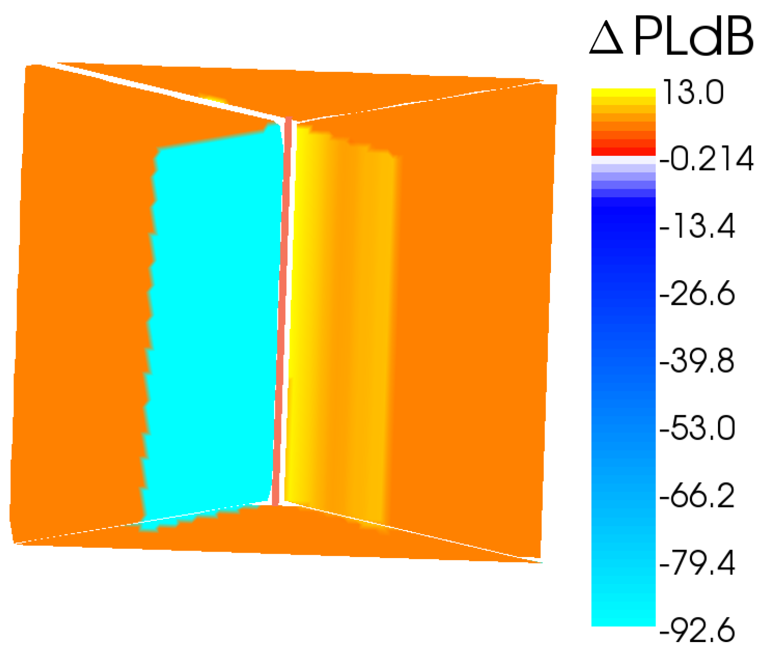

Figure 3.9: This contour illustrates the change in PLdB relative to the incident wavefront. The PLdB of the input wavefront 92.6. As expected, the field points where a direct and ground reflected wave front are present, illustrate a change in PLdB of approximately 6 dB (6.69 exactly). While pressure doubling is associated with a change of 6 dB, PLdB is a measure of rise time, not power: this explains the slight departure from an exact 6 dB change.

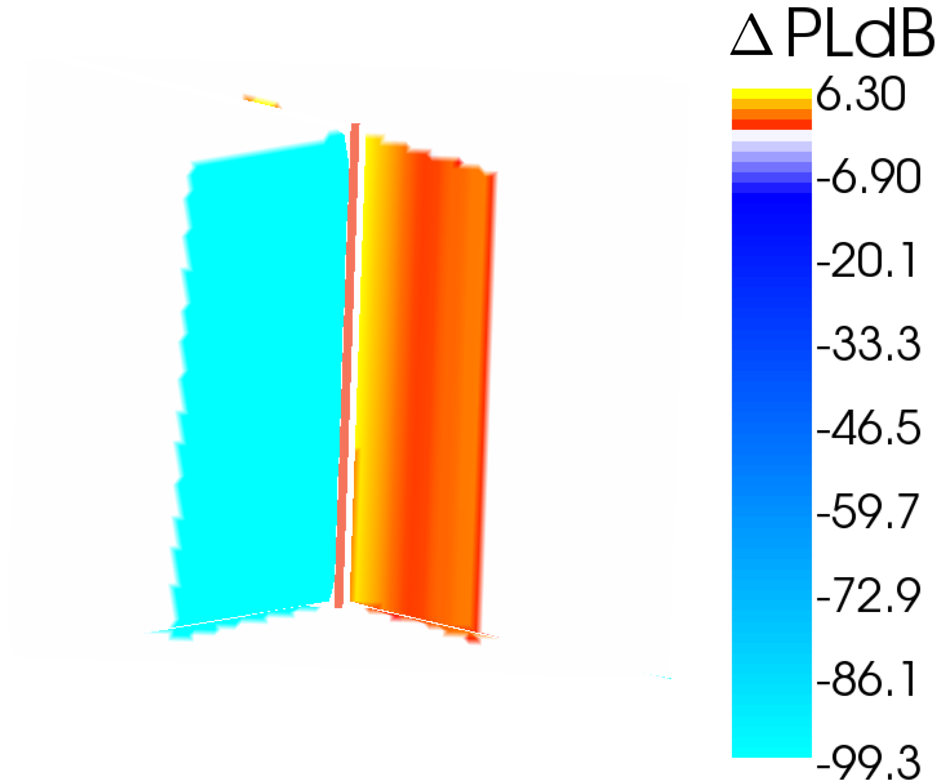

Figure 3.10: This contour illustrates the change in PLdB relative to the pressure doubled wavefront. The PLdB of the input wavefront AFTER pressure doubling was 99.3. This focuses on the effect of the vertical structures on perception.

Contours like this are particularly illuminating, as it is difficult to accurately intuit the impact of constructive interference on rise time with various delays.

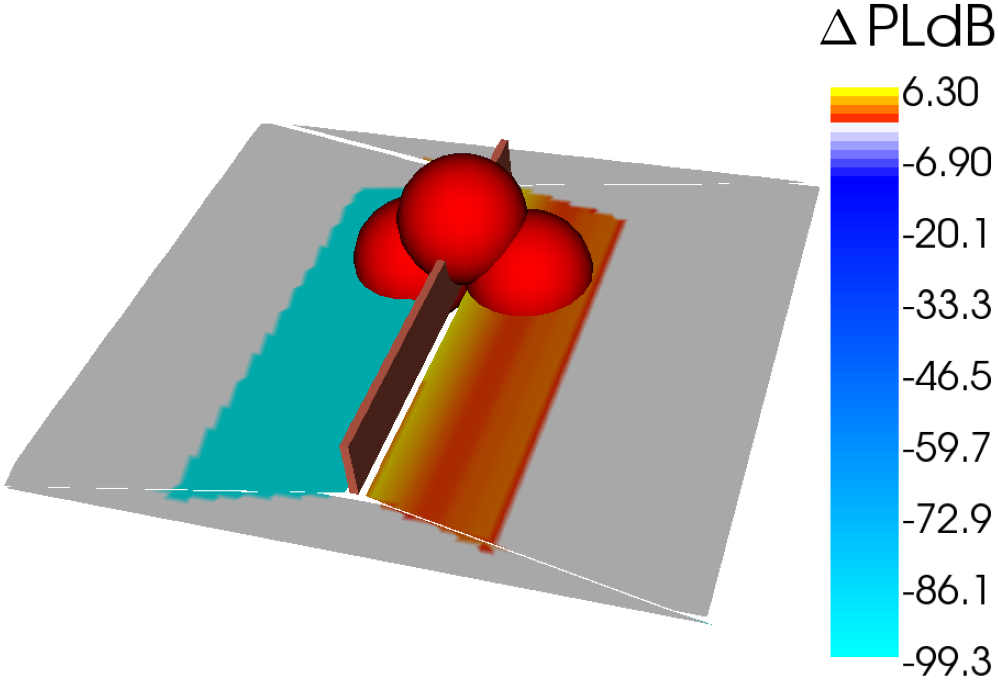

Figure 3.11: This contour is another visualization of the same data presented in the previous figure. It illustrates the change in PLdB relative to the pressure doubled wavefront. The PLdB of the input wavefront AFTER pressure doubling was 99.3. This focuses on the effect of the vertical structures on perception. The locations of microphones 201, 202, and 203 are shown with red spheres.

While figure 3.10 offers accurate colors for comparison with the color scale, figure 3.11 offers perspective on the geometry. The pressure time histories of the three microphones will be addressed next.

3.2.1.6 Simulated Results - Time Series

The utility of the contours, is that they communicate how values or metrics vary with space. Having identified where in the contours the actual microphones were placed, we are able to compare the recorded pressure time histories with the simulated time histories. In this section, we present plots of the simulated time histories at the three microphone locations.

In Chapters 5 and 6, these time histories are compared to the measured sonic boom waveforms, with and without considering the diffracted contribution.

Recall that from right to left, the microphones are 202 203 and 201. Details regarding what image sources are valid at each microphone locations were given in Table 3.1.

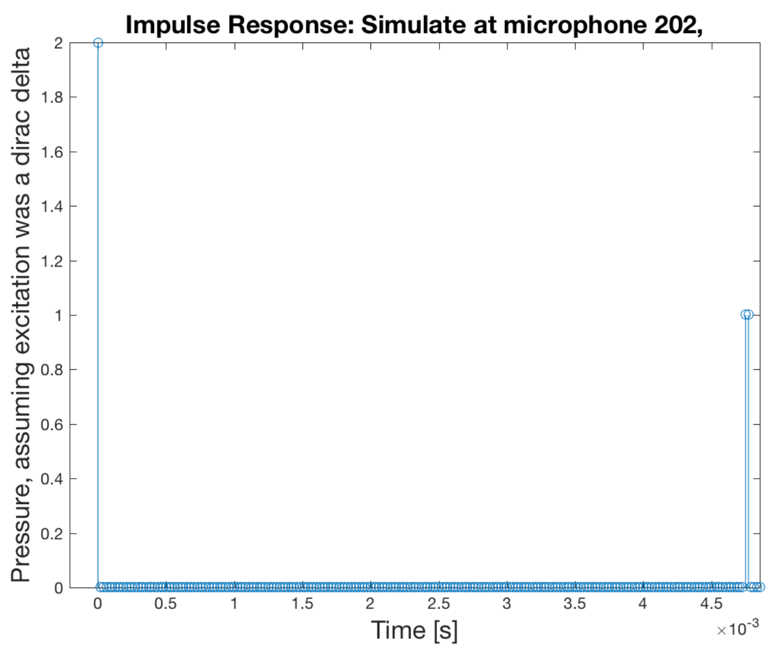

Figure 3.12: This is the impulse response at Microphone 202, the microphone receives a ground reflection co-incident with the direct sound, as shown by the initial impulse with a magnitude of two. Approximately 4.75 ms later, the two second order reflections involving the wall and ground arrive.

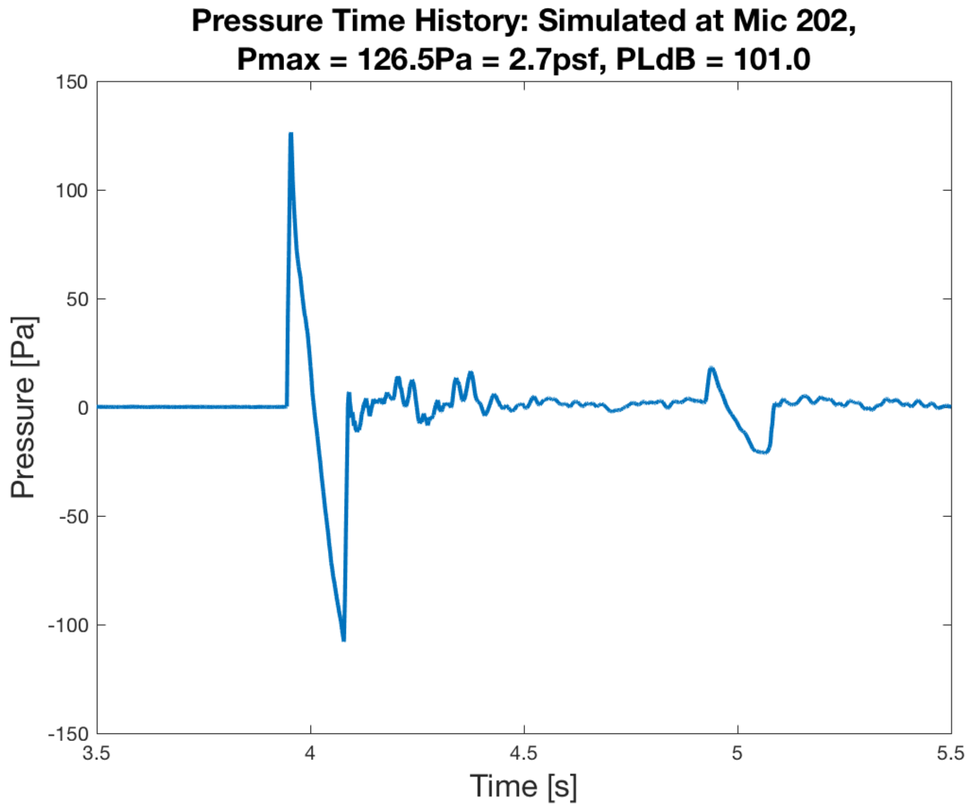

Figure 3.13: This waveform is our best approximation for the time history at microphone 202, and the result of the convolution of the impulse response in figure 3.12 with the input waveform shown in figure 3.7.

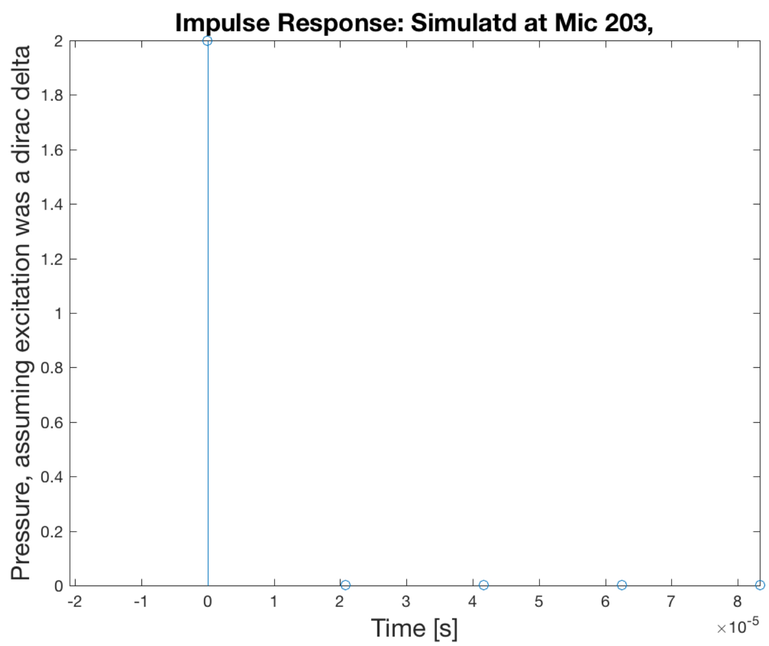

Figure 3.14: This is the impulse response for microphone 203, the microphone on top of the wall. It receives only the direct and 'ground' reflected contributions. In this case 'ground' refers to the surface on top of the wall. This is expressed as the initial sample with value 2, as though two coincident dirac deltas had been summed.

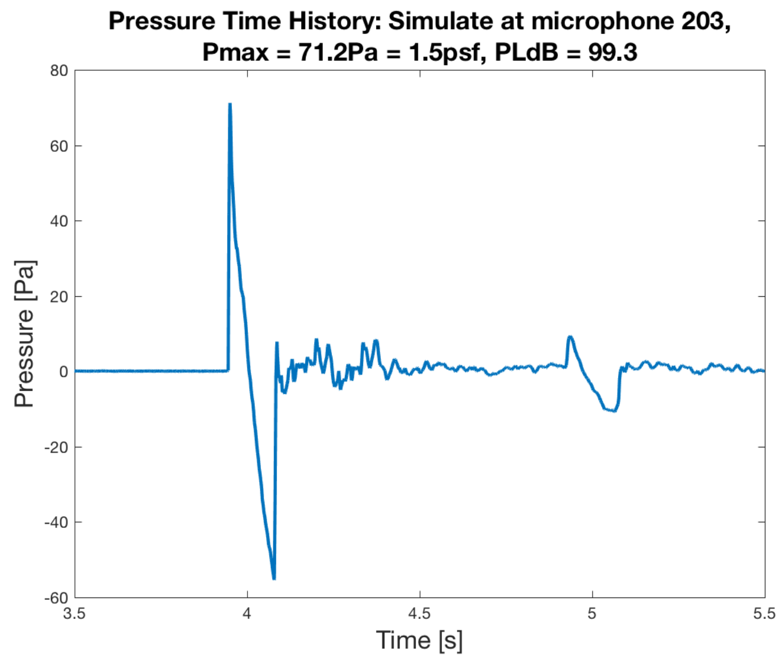

Figure 3.15: This waveform is our best approximation for the pressure time history at microphone 203, and is the result of the convolution of the impulse response in figure 6.12 with the input waveform shown in figure 3.7.

The impulse response in the shadow zone, where microphone 201 resides is all zeros. While this case is the least interesting specular case, it is the most interesting diffracted case in the subsequent chapter.

3.2.2 L Shaped Building

While the isolated wall geometry will be the focus of the remaining chapters, to bolster confidence in the specular reflection code, we will explore two more complicated geometries.

The resolution of the placement of observer positions around the L- Shaped building is 2 microphones per meter, distributed in a rectilinear grid above each ground plane. The L shaped building has a 45.72 [m] (150') x 38.1 [m] (125') overall footprint, with a thickness of 12.192 [m] (40') and height of 3.048 [m] (10').

These simulations vary significantly from those presented for the isolated wall, in that this simulation was performed at listener height, 1.2 [m] above ground level.

As such, the shadow zone is more complicated, there is a thin perimeter where the incident wavefront is present, but the ground reflection is not valid: the field point is not in the field angle, or frustum formed by the image source, and illuminated portion of the ground plane.

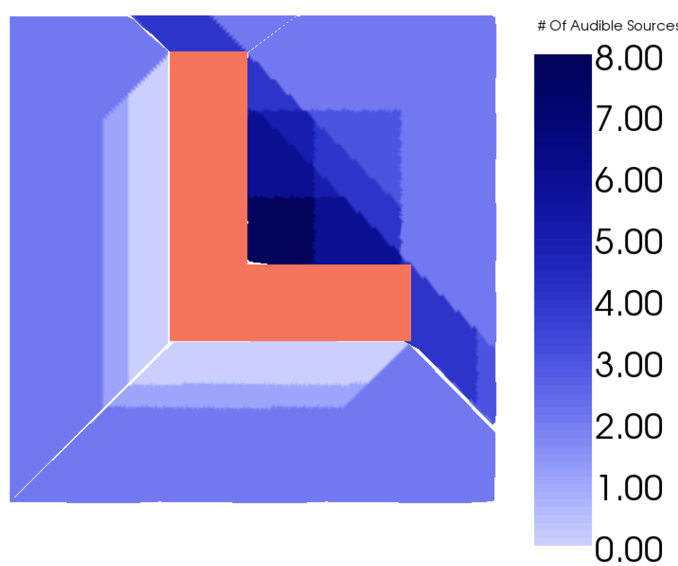

Figure 3.16: The number of reflections matches with what one would intuitively expect if envisioning reflection and occlusion of light by a mirrored surface. The building structure is shown in red only for contrast.

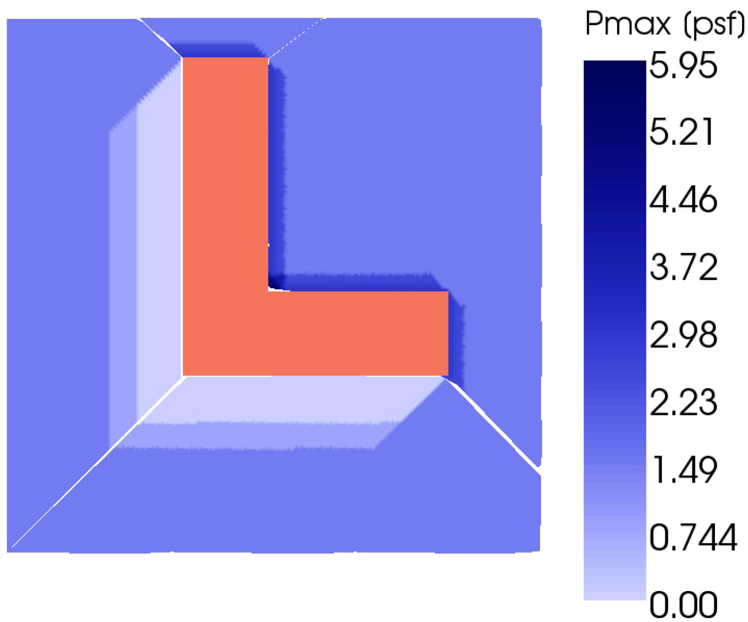

Figure 3.17: Maximum pressures reflect constructive interference. They are interesting in that the locations where they meaningfully vary depend strongly on the shape of the waveform. The period of our input is 140 ms, so constructive interference only happens when delayed less than 70 ms, which corresponds to about 24 meters of propagation. Recalling that the incident wavefront exhibit a maximum pressure of 35.91 [Pa] (.75 psf), a maximum pressure of 8x that, approximately 287.28 [Pa] (6 psf), aligns with expectations.

As in the previous section the two contours which follow are all representations of the same data. The first contour offers the change in PLdB due to the listening environment, relative to the input waveform. The second image offer the change in PLdB due to environment, relative to the pressure double waveform. Comparing to the pressure doubled waveform essentially ignores the impact of the ground reflection. However, since this simulation was performed at listener height, the field points which receive only a ground reflection still exhibit a relative change in PLdB, due to the fact that the direct and ground reflected wavefronts are not coincident.

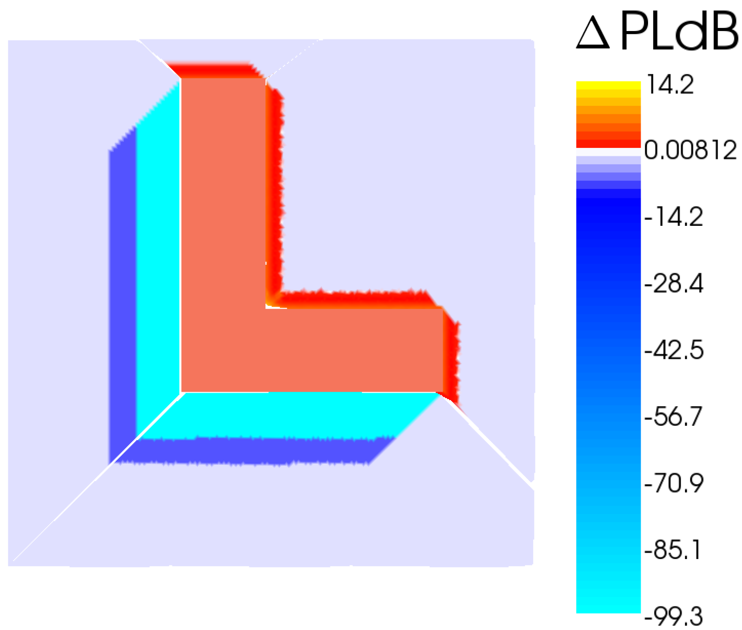

Figure 3.18: PLDB around the L-Shaped Building: A mesh was generated at listener height (1.2 m) comprised of many listener positions. At each listener position, we generated a time domain pressure waveforms that were the result of super-imposing N-waves from from each image source. This time domain waveform was then processed to calculate the PLdB metric. The "hotter" colors here indicate a higher perceived loudness. The PLdB values here are the change in PLdB compared to that obtained with a single ground reflection, in absence of the building.

3.2.3 52 Blackbird at Edwards AFB

The following contours are offered only to illustrative what these contours look like for more complicated geometries . They were generated with a distinct incident sonic boom waveform. While the microphone positions shown in green in in figure 3.21 the diffraction code in the following chapter is not sufficiently generalized to handle such complicated geometries. As such assessment of the simulations for this geometry and agreement with the experimental dataset will be left to future research and publication.

52 Blackbird is the street address of a multi unit dwelling that was heavily instrumented on Edwards Airforce Base. This residence was impinged upon by many sonic sonic booms during a 2007 Field Test, more details about the building and test may be found in the Technical Memo. [73]

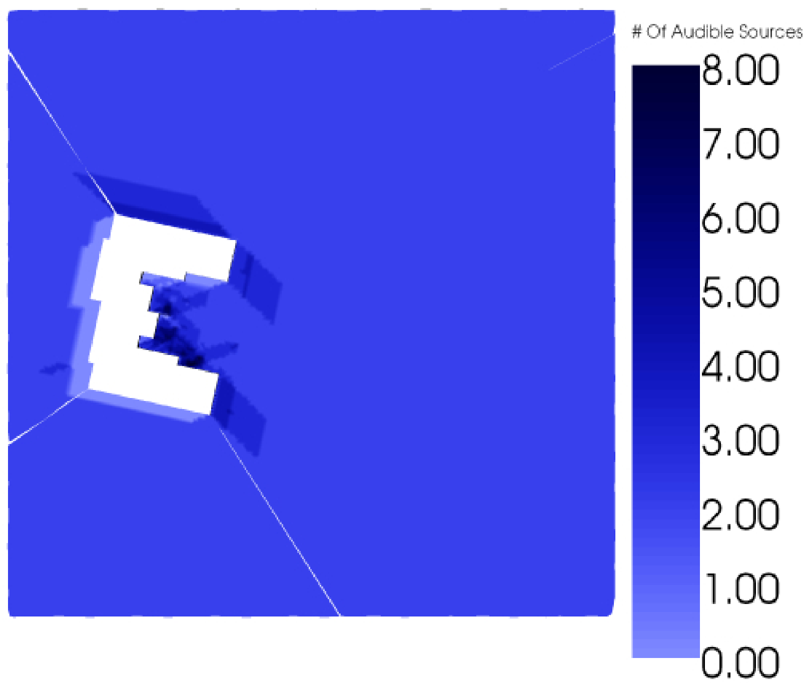

Figure 3.19: 52 Blackbird, Number of Image Sources. The darkest shade of blue in this graphic indicates where there are 8 image sources. The predicted number of image sources at each location matches intuition and our predictions in Fig.1.7.

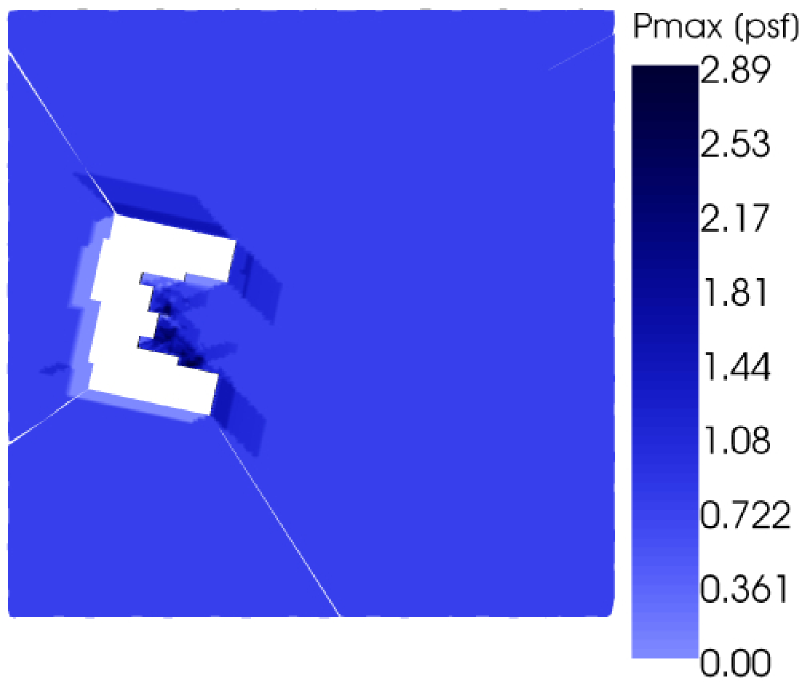

Figure 3.20: 52 Blackbird, Maximum Pressure. This plot indicates the peak pressure in a mesh just above ground level. This peak pressure was calculated by superimposing delayed reflections based on the positions of the image sources in Fig. 3.19.

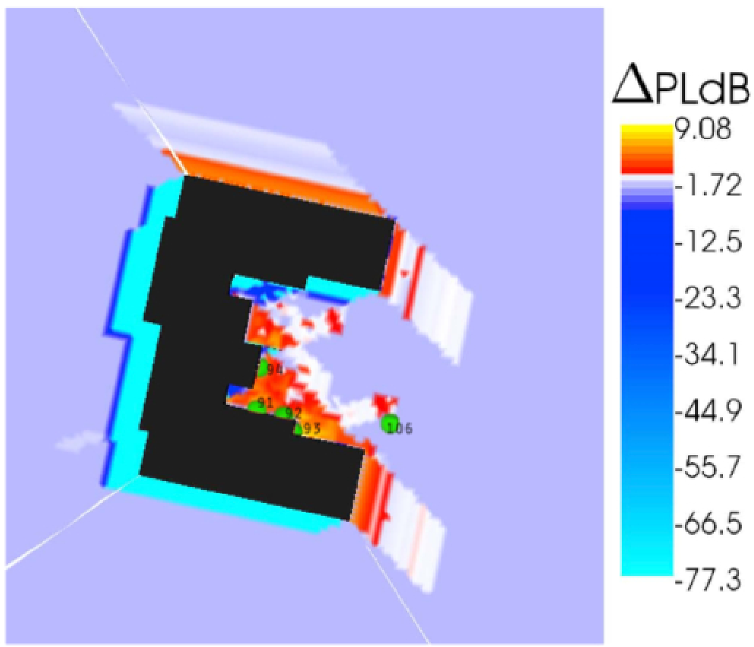

Figure 3.21: Change in PLdB, relative to pressure doubling: A mesh was generated comprised of many listener positions. At each listener position, we generated a time domain pressure waveforms that were the result of super-imposing N-waves from from each image source. This time domain waveform was then processed to calculate the PLdB metric. The "hotter" colors here indicate a higher perceived loudness. The PLdB values here are the change in PLdB compared to that obtained with a single ground reflection, in absence of the building.

Chapter 4

Biot Tolstoy Medwin (BTM) Edge Diffraction

4.1 Introduction

Through Chapter 3, Geometrical Acoustics (GA), specifically the Image Source Method, predicted the time series pressure waveforms in a planar geometry. GA and Image theory are accurate at field points where the incident and specularly reflected fields dominate, that is, when diffracted and diffuse fields are negligible. We initially posit that specular predictions are sufficiently accurate to calculate the correct PLdB at such field points, hypothesizing that the diffracted contributions are negligible from the perspective of PLdB, the validity of that hypothesis is quantified in Section 6.

In shadow zones, which arise when incident waves are occluded and when reflected waves originate from finite reflectors, diffraction is no longer negligible. In fact, in a homogeneous atmosphere, the diffracted waveform completely predicts the pressure waveform in the shadow zone. This chapter offers a general overview regarding diffraction phenomena, and a brief literature review showcasing prominent models and their applicability to the task at hand. Having generally discussed diffraction modeling we focus on implementation with a description of the Biot-Tolstoy-Medwin (BTM) approach to model edge diffraction. Our implementations are validated with comparison to academic cases in Section 4.3.3. Application of the BTM model to our Isolated Wall Geometry occurs in Section 4.3.4.

4.1.1 Frequency Dependent Diffraction Regimes

Diffraction phenomena may be divided into three regimes, distinguished by the relative size of the scattering object to the wavelength. For relatively low frequencies, and long wavelengths, the scatterer is said to be "acoustically small" ($< \lambda/10$); this is Rayleigh Scattering, and exhibited by blue light and the O_2 and N_2 atoms comprising our atmosphere. When wavelength and scatterer dimensions are of the same order, diffraction is said to be in the resonant regime (Mei scattering). In the high frequency regime, above the resonant scattering, the scatterer is said to be acoustically large. In this high frequency regime, geometrical acoustics and ray based solutions are often sufficiently accurate.

As mentioned earlier, Geometrical Acoustics and the ISM model discussed in the previous chapters predict abrupt transitions into a completely silent shadow zone when the wavefront is occluded. This approximation, neglecting diffraction becomes increasingly accurate in the high frequency regime, and as the scattering object becomes larger. Diffraction contributes significantly at the shadow boundary, smoothing the discontinuity at all frequencies. The width of this smoothing zone around the shadow boundary trends with wavelength. Away from the shadow boundary however, it's predicted that the amplitude of the diffracted contribution is inversely proportional to frequency. This is exemplified by the Sommerfeld problem, where the diffracted contribution away from the shadow boundary trends with $O(k^{-1/2})$ [36].

4.1.2 Glossary

In the process of the literature review there were many recurring terms. In lieu of redefining them at every usage, I've collected selected definitions here. Any italicized term encountered through the document and related to diffraction will be elaborated upon here.

Geometrical Acoustic Limit: Geometrical Acoustic models are historically ray based high frequency models and only consist of specular reflections. The geometrical acoustic limit is the frequency below which geometrical acoustics is no longer valid. This limit is highly dependent on the scale of the geometry being modeled.

Decompositional Approach: Instead of solving the wave equation directly, decompositional approaches leverage conservation of energy, and linearity to model propagation via different acoustic phenomena separately, and sum their contributions via superposition. For example: specular, diffracted, and diffuse contributions to an IR are calculated separately.

Kirchhoff Approximation: "In the Kirchhoff theory of diffraction, the wave field in the aperture and on the illuminated surface of the screens is defined as what would be predicted by the incident wave at those locations. The distortion to the wave field in the immediate vicinity of the contour of the aperture is neglected. Thus neglecting the illumination of the screen by diffraction" [38].

Dirac Delta: A delta function, a function with all energy centered around the 0^{th} sample, and an integral of 1 over all samples.

$$\delta_d(n) = \begin{cases} \infty, & \text{if } n = 0 \\ 0, & \text{if } n \mathrel{!=} 0 \end{cases} \tag{4.1}$$

constrained by :

$$1 = \int_{-\infty}^{\infty} \delta_d(n) dn \tag{4.2}$$

Kronecker Delta: A delta function, a function with all value of 1 at the 0^{th} sample, and 0 elsewhere.

$$\delta_k(n) = \begin{cases} 1, & \text{if } n = 0 \\ 0, & \text{if } n \mathrel{!=} 0 \end{cases} \tag{4.3}$$

Doublet Source: A doublet source is generated by an injection of unit volume at a point source. The resulting pressure waveform is the derivative of an impulse. This is expressed mathematically in Section 4.3.

Fresnel Zone: This term finds similar but distinct usage in Optics as well as longer wavelength Electromagnetism (Radio). For our purposes a Fresnel Zone is the area on a radiator/reflector/or aperture which all contributes constructively OR destructively for at a receiver position. The lines demarcating adjacent Fresnel Zones are contours on the reflector - they are comprised of points where the length of the piecewise path from source-to-reflector-to-receiver vary by exactly half a wavelength.

Fresnel Number I: Named after Augustin-Jean Fresnel, The Fresnel Number is the non-dimensional number: $N_F = 2d/\lambda$, where d is the length of diffracted path (shortest path around the barrier) minus the distance between the source and receiver through the barrier. The Fresnel Number increases for larger barriers, and smaller wavelengths. The higher the Fresnel Number, the greater the insertion loss due to the presence of the barrier.

Fresnel Number II: A second definition of the Fresnel number, is the number of Fresnel Zones which fit on a reflector or aperture for a give source/receiver orientation. These two definitions are geometrically similar, but not identical. For a circular reflector/aperture with a source on axis a distance z from the reflector, $N_F(z) = \frac{a^2}{\lambda z}$.

Fresnel Integrals I: $S(x) = \int_0^x \sin(t^2)dt$, and $C(x) = \int_0^x \cos(t^2)dt$ are the Fresnel Integrals, they find utility in the Geometric Theory of Diffraction and Uniform Theory of Diffraction Solutions. These functions are odd, and less than one for all x.

Fresnel Integrals II: $F(\xi) = e^{-i\xi^2} \int\limits_{\xi}^{\infty} e^{is^2}$ This "Fresnel Integral" is less common, and is essentially the scaled and complex version of *Fresnel Integral I*

Error Function: $\mathrm{erf}(x) = \frac{2}{\sqrt{\pi}} \int_0^x e^{-t^2} dt$, Fresnel integrals don't have a closed form solution, and are often solved for numerically in terms of the error function. Approximations of the error function exist in many programming languages.

Semi-Analytical: An analytical expression for an academic/idealized geometry that has been applied to a more realistic geometry through application of general physical, instead of directly through mathematics. In this case, making an infinite integral finite through application of Huygen's principle.

Velocity Potential: The wave equation may be written in terms of pressure p, density ρ, partial velocity $\bar{u}$, temperature T, and velocity potential Φ. Velocity potential is a scalar field, like pressure, and is related to velocity and pressure as such: $\bar{u} = \nabla\Phi$, and $p = -\rho\frac{\partial}{\partial t}\Phi$.

4.2 Literature Review

Analytical, *semi-analytical*, and pragmatic solutions for predicting diffracted acoustic fields, are abundant. We restrict the scope of this section to implementation in generalized geometries with idealistically rigid and glossy boundaries, still, the relevant literature is vast. The problem has been approached from many perspectives, yielding methods appropriate for a variety of applications. What follows is far from an exhaustive historical account, but instead a survey in which we narrow our focus to models which will best serve our needs, while gleaning rules of thumb and heuristic observations from models which are otherwise not well suited for the task at hand. For thorough histories, see [39].

For many applications, frequency domain solutions and approximations are sufficient. Common applications of diffraction models include the prediction of the insertion loss of a barrier to protect listeners from road noise or machinery. Since road-noise, condensers, heat pumps etc. are continuous sources, empirical predictions based on the *Fresnel Number*, or a spreadsheet calculation based on the Maekawa model find common use in an architectural consulting setting with continuous mechanical noise sources. [19]

Recall that the application we're addressing is that of impulsive sources. For impulsive excitations, the diffracted and direct fields may not have the temporal overlap to interact, rendering continuous wave solutions inappropriate. In this Section, we first aggregate guiding principles and rules of thumb building an intuitive understanding of acoustic diffraction. We then focus on the BTM Model implemented.

4.2.1 Heuristic Concepts with Simple Guidelines

This section enumerates physical laws, and observed trends with regards to diffracted contributions. The first items were mentioned earlier in introductory chapters, we elaborate a bit more regarding the guiding physical principles.

1. Energy at low frequencies effectively propagates past acoustically small obstacles without reflection or occlusion.

2. The width of the shadow boundary transition is proportional to wavelength.

3. The diffracted contribution away from the shadow boundary is on the order of $O(k^{-1/2})$, meaning it's magnitude is proportional with the root of wavelength.

4. The diffracted contribution has the greatest amplitude for the least time path, that is the first diffracted contribution, or the shortest path from source to edge to receiver.

   Let's elaborate briefly by focusing on fundamental physical principles which develop intuition surrounding diffraction. With our focus on time-domain accurate models, a particularly relevant physical property of wave propagaton is captured in **Fermat's Principle**. Fermat's Principle, also sometimes referred to as the principle of least time, was named for Pierre de Fermat. The principle states that the path taken by a ray of sound or light between two points is the path that can be traversed in the least time. Stated another way, when dealing with occlusion problems where there is a barrier between a source and receiver, the 'least time' path is the path from the source, to the edge of the occluding obstacle, to the receiver. The specific point on the edge occluding obstacle, (referred to as the 'Apex' on the BTM model') is the point where the path is the shortest. Fermat's principle begins to make more sense in light of **Huygen's Principle**.

5. Huygen's principle states that a wavefront can be perfectly approximated by the sum of spherical sources all along the surface of the wavefront. When you consider Huygen's principle, and visualize a wavefront passing through an occluding obstacle, through an aperture, or otherwise being made discontinuous, a spherical source will emerge at the discontinuity. Thus, there is a direct path from the source to the discontinuity, and from every discontinuity to the receiver.

6. Lastly, **Babinet's Principle** states that the field produced when a wavefront is reflected by a finite reflector, is identical to that generated by the complementary wavefront passing through an aperture in the complementary geometry with regards to both specular and diffracted fields.

7. Visualizing propagation based on the principles above, it becomes clear that when considering receivers at field points that receive both diffracted and direct contributions, that the diffracted contribution always arrives later than the direct contribution.

8. As discussed in prior Chapters, recall that for a given frequency diffracted contributions are the largest the closer they are to the shadow zone. For a semi-infinite barrier, the lower the frequency, the greater the diffracted contribution at any location.

4.2.2 Frequency Domain Solutions

4.2.2.1 Classic Sommerfeld Solution

The classical result of the Sommerfeld problem of diffraction by a two dimensional rigid half line, extending infinitely in the 3rd dimension is given by:

$$\Phi = \frac{e^{ikr-i\pi/4}}{\sqrt{\pi}} \sum_{\pm} F\left(-\sqrt{2kr}\cos\left(\frac{\theta-\theta_o}{2}\right)\right)$$

where $F(\xi) = e^{-i\xi^2} \int\limits_{\xi}^{\infty} e^{is^2}$ is the Fresnel integral [37]

Note, this Fresnel Integral is distinct from the Fresnel Integrals found in reference [40] which take the form $C(\mathrm{v}) = \int \cos\left(\frac{pi}{2} z^2\right) dz$ and find application for calculation of the back scattering from a finite rectangular panel using the Kirchoff-Fresnel approximation.

4.2.3 Time Domain Solutions

The continuous wave solutions discussed above assume the source has been radiating energy from the beginning of time - the solution expresses the result of the stabilized constructive and destructive interference at every point. Time domain solutions may also be referred to as transient solutions - they are appropriate for application to problems where the excitation is so brief that at some locations various direct, reflected and diffracted waves are not collocated in space at a particular time and thus do not interfere.

Keller and Blank offered a distinct solution to the same transient plane wave case. Given the planar nature of the sonic boom wavefront, these approaches would be appropriate for first order diffraction. [41]

4.3 Implemented Diffraction Model

The most extensively explored and applied approach in this paper is what has been referred to as the Biot-Tolstoy-Medwin approach (BTM). Peter Svensson offered an implementation of 'Edge Diffraction' based upon the same theory. Svensson's implementation has found popularity and use via his Matlab Toolbox, but more widely through it's incorporation into CATT Acoustic [20], a popular architectural acoustic modeling program. The aim is to investigate the development of an edge diffraction model based upon BTM and offer an implementation in a C++ tool with specific utility to our application.

BTM: Historical Development

In 1957, Biot and Tolstoy authored the following JASA paper "Formulation of wave propagation in infinite media by normal coordinates with an application to diffraction". [42]

This paper offered a closed form solution for the pressure diffracted by an infinite wedge ensonified by a point source radiation from an infinite wedge. The derivation employed a 'Hilbert Space Method'. An infinite wedge is characterized by it's open angle, ζ. If the open angle is an integer fraction of pi, $\frac{\pi}{m}$ the acoustic field in the corner is perfectly defined by $2m-1$ image sources: there is no diffracted component.

The Biot+Tolstoy formulation begins by assuming that the point source is generating what has been called a *doublet source* or an explosion of injected volume. The source is characterized by defining the **displacement potential** as such:

$$\Phi = \frac{-1}{4\pi R}\mathrm{U}(t - R/c) \tag{4.4}$$

Where $U(t-R/c)$ is the unit step function, and R is the distance between the point source and field point. This communicates an explosion of injected volume at the point source position at time $t=0$.

Note! This use of Φ is distinct from it's common utility as *velocity potential*, which is related to pressure with a single partial time derivative. Pressure and **displacement potential** are related by:

$$p(t) = \frac{\rho\delta^2\Phi}{\delta t^2}, \text{and so...} \tag{4.5}$$

$$p(t) = \frac{\rho}{4\pi R}\delta'(t - R/c). \tag{4.6}$$

Where δ' is a 'doublet', the time derivative of δ, the dirac delta function.

Medwin, in his 1982 contribution to JASA [43], reformulated the problem by beginning with a point source which injects volume uniformly and continuously, beginning at time $t = 0$. Essentially integrating all expressions characterizing the source by t.

The point source emits pressure:

$$p(t) = \frac{\rho}{4\pi R}\delta(t - R/c). \tag{4.7}$$

Seeing this, we would expect that an IR offered by any other formulation would resemble the BTM formulation, save the $\frac{\rho}{4\pi R}$ scaling factor introduced by the definition of the point source. The next section presents the solution offered by Medwin for diffracted pressure when the source is defined by Eq. 4.7.

4.3.1 BTM: Defining Equations

Reproduced here exactly as found in [43];

$$p(t) = (-S\rho c/4\pi\theta_w)\left\{\beta\right\}(rr_o \sinh Y)^{-1}\exp(-\pi Y/\theta_w) \tag{4.8}$$

$$\begin{aligned} \beta = \sin[(\pi/\theta_w)(\pi \pm \theta \pm \theta_o)] \times \\ \{1 - 2\exp(-\pi Y/\theta_w)\cos[(\pi/\theta_w)(\pi \pm \theta \pm \theta_o)] + \exp(-2\pi Y/\theta_w)\}^{-1} \end{aligned} \tag{4.9}$$

$$Y = \mathrm{arcCosh}\,\frac{c^2t^2 - (r^2 + r_o^2 + Z^2)}{2rr_o} \tag{4.10}$$

Where the least time over the wedge is:

$$\tau_o = [(r + ro)^2 + Z^2]^{1/2}/c. \tag{4.11}$$

It's clarified that "the curley bracket consists of the sum of your terms obtained by using the four possible combination of angles" [43]. However, even this clarification is ambiguous, as the curly bracket is found around β in the definition of the pressure time series, as well as around half of the definition of β. We proceed assuming they only refer to the former.

Thus β is expanded as such:

$$\beta = (\beta_{++} + \beta_{+-} + \beta_{--} + \beta_{-+}), \text{ where} \tag{4.12}$$

$$\beta_{++} = \sin[(\pi/\theta_w)(\pi + \theta + \theta_o)] \times \\ \{[1 - 2\exp(-\pi Y/\theta_w)\cos((\pi/\theta_w)(\pi + \theta + \theta_o)) + \exp(-2\pi Y/\theta_w)\}^{-1} \tag{4.13}$$

$$\beta_{+-} = \sin[(\pi/\theta_w)(\pi + \theta - \theta_o)] \times \\ \{1 - 2\exp(-\pi Y/\theta_w)\cos((\pi/\theta_w)(\pi + \theta - \theta_o)) + \exp(-2\pi Y/\theta_w)\}^{-1} \tag{4.14}$$

$$\beta_{--} = \sin[(\pi/\theta_w)(\pi - \theta - \theta_o)] \times \\ \{1 - 2\exp(-\pi Y/\theta_w)\cos((\pi/\theta_w)(\pi - \theta - \theta_o)) + \exp(-2\pi Y/\theta_w)\}^{-1} \tag{4.15}$$

$$\beta_{-+} = \sin[(\pi/\theta_w)(\pi - \theta + \theta_o)] \times \\ \{1 - 2\exp(-\pi Y/\theta_w)\cos((\pi/\theta_w)(\pi - \theta + \theta_o)) + \exp(-2\pi Y/\theta_w)\}^{-1} \tag{4.16}$$

In equations 4.12-4.16, the curly brackets have no special meaning, beyond the usual distributive property. The $\times$ operator simply indicates multiplication. The validated function used to implement these equations is given in Appendix D.

4.3.2 BTM: Finite Edges and Huygen's Interpretation

The equations reproduced and clarified in the previous Section are an analytical solution for the diffracted field around an infinite wedge. In order for this solution to find practical implementation and application to a generalized planar environment, it needs to be adapted for finite edges. This was first accomplished through a "Huygen's Interpretation" by Medwin [43] and then popularized by Svensson [44]. Based on intuitive understanding Huygen's Principle, we assume that each point along the edge contributes at only one moment in time. Said another way -

the arrival of the diffracted contribution from each point along the edge is given by the propagation time traversing the path from source-to-edge-to-receiver for that edge point. Thus, for finite edges, the diffracted solution is truncated.

Note, if an Apex point, or the 'least time path' edge point is in the middle of the edge, the diffracted contribution will decrease to zero with two discontinuities - one for each end point of the edge found on either side of the Apex point.

It is assumed that the diffracted contributions on either side of an apex point at any point in time contribute equally, but this assumption is never justified.

4.3.3 BTM: Validation

Having discussed the underlying theory, we validate our implementation of the BTM model for diffraction around a single wedge against published implementations.

4.3.3.1 90° Wedge

Here we validate the single diffraction BTM solution outlined in Section 4.2.3, and recreate images from the seminal document to validate that our implementation is as the authors intended.

The follow variables define the condition to be simulated for validation purposes. They are mostly documented in the old caption for the figure below, but are listed here to eliminate any possibility for ambiguity.

Source Coordinates: $(r_o = 100[m], \theta_o = 45, 0)$
Receiver Coordinates: $(r = 100[m], \theta = 225 + \epsilon, Z = 0)$
Where $\epsilon = [.1, .5, 1, 10]$
Physical Constants: sound speed $c = 343[m/s]$, density of air $rho = 1.2[kg/m^3]$

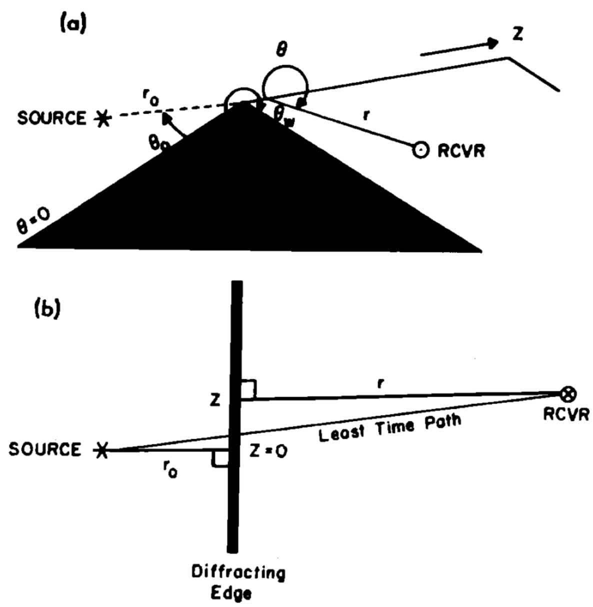

FIG. 1. (a) Wedge geometry for Eqs. (1)–(3); (b) unfolded geometry.

Figure 4.1: Biot-Tolstoy-Medwin Diffraction Model - Validation Geometry Orientation and Definition.

While implementing this model with the aim of reproducing Figure 4.2a (shown below), two ambiguities arise:

1. In Equations 4.10 - 4.16 (above) we find the variable S. The variable goes undefined above in the reference [43]. For the purpose of this validation, we will assume $S = 1$. We will address this with more rigor in Section 4.3.4.2.2, where we discuss the required scaling factors for agreement in both the time and frequency domain. Historically S is used to represent source strength, If the source is based on a "delta function acceleration source", then the source strength should be completely defined. Without a confident definition of S, we essentially have an unknown scaling term.

2. The results we are to reproduce in Figure 4.2a , are presented as $p(n\Delta T)$, without mention of the value of ΔT. Later in the document, we find a figure

that shows a frequency response extending to 40 kHz. So let us set this ambiguities aside by assuming $fs = 80$ [kHz], and $\Delta T = 1/fs = 12.5$ [μs].

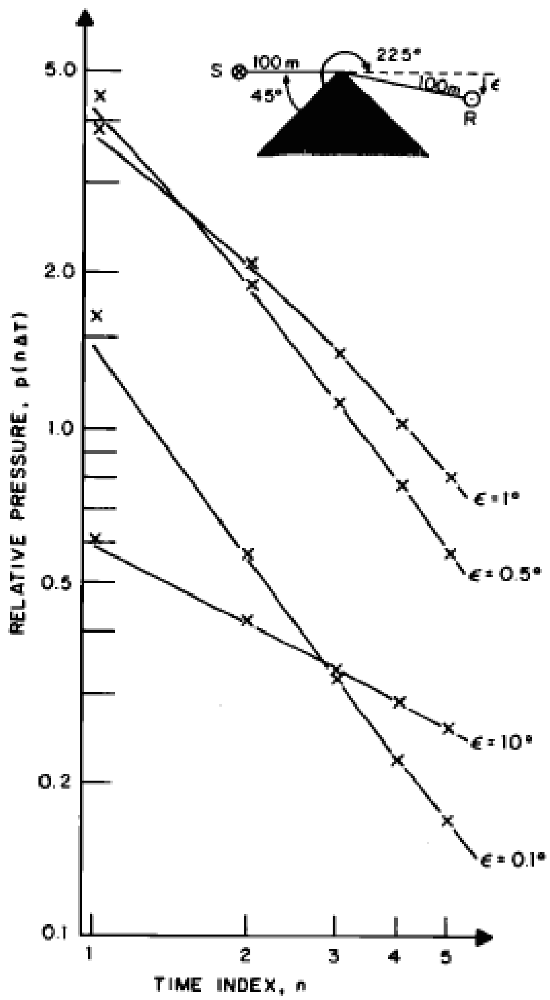

(a) Original

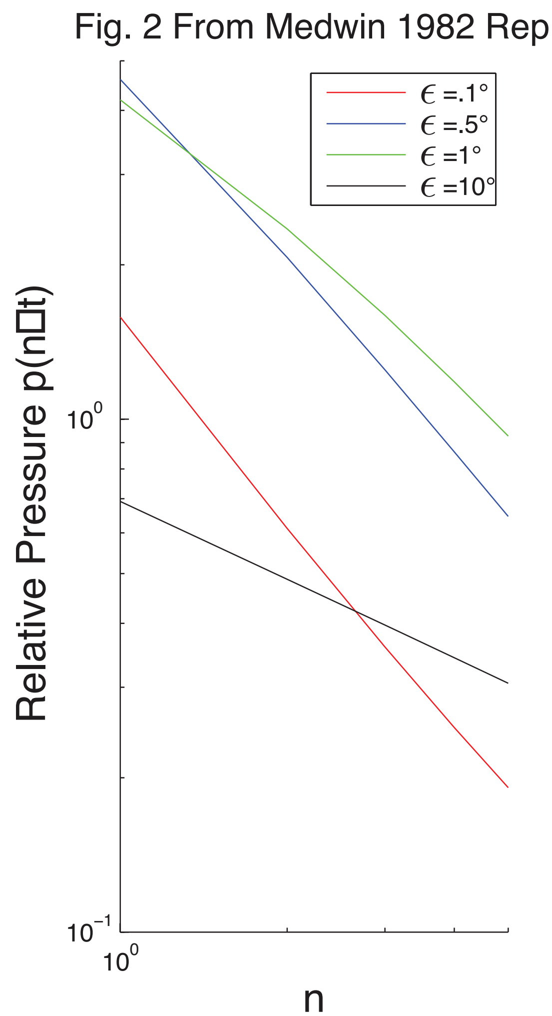

(b) Validation

Figure 4.2: Time Domain Comparison of Medwin 1982's Wedge Figure. Note that the x-axis has no real units. Also note that the expressions for the IR go to infinity as $\tau = t - \tau_o$ goes to zero. After some trial and error, it was found that $fs = 110$ [kHz] resulted in the plots above, which agree well. Also note that the $n = 0$ sample is not shown in the reference figure.

4.3.3.2 Visualizing Expected Trends

Having validated the time domain IR for a single geometry, let's explore how the IR varies with geometry. An interactive implementation the BTM solution is presented here - illustrating trends and allowing easy access to a functioning code sample:

`http://www.amandalind.com/Sandboxes/BTM_DiffractionSandbox.html`

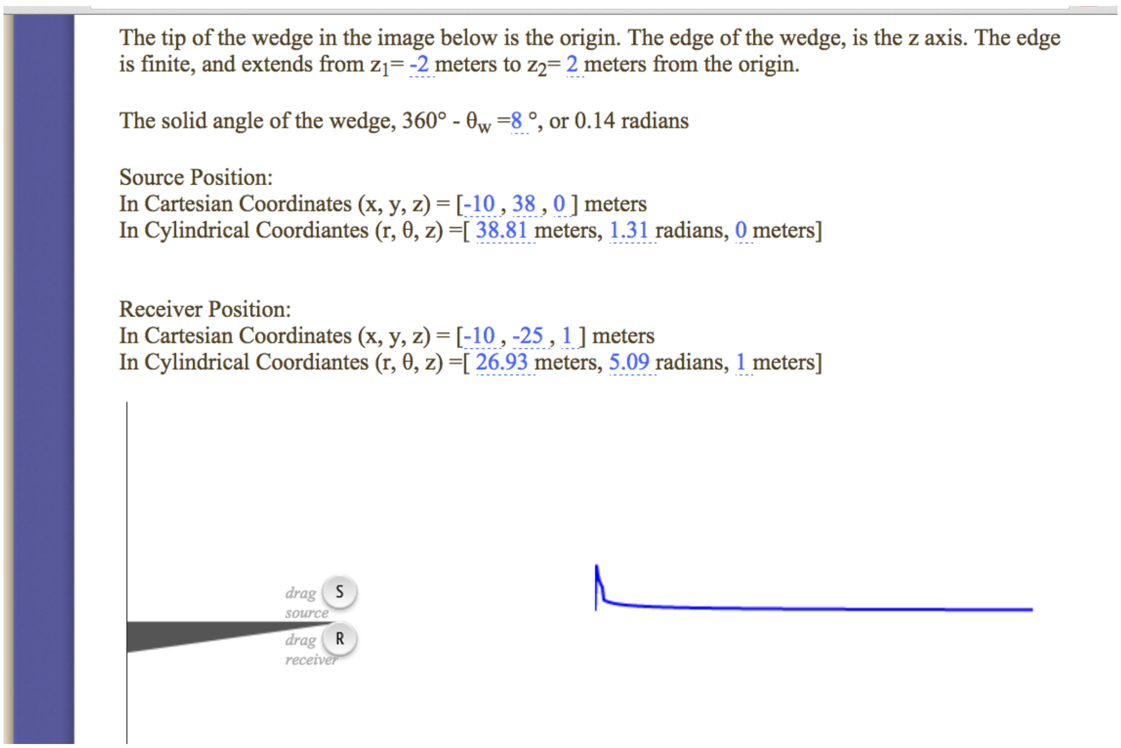

Figure 4.3: Here we see a screenshot of the interactive website accessible at the address above. To the left, we see a wedge: the solid angle of the wedge is shaded, and adjustable by clicking and dragging the blue numbers on the site. Source and Receiver position can be altered by clicking and dragging the them around the wedge. To the right, we see a plot of the diffracted impulse response at the receiver position. Recall, Medwins 1980 presentation built upon Biot & Tolstoy's 1957 analytical solution for an infinite wedge. Medwin offered that, with the aid of computers, the solution was suitable for finite edges. This is achieved by computing the diffracted IR for a single edge sample by sample. A Huygens Principle interpretation indicates the portion(s) of the wedge responsible for each sample. This allows the response to be truncated when the edge is finite. The step change in the IR above occurs because of the asymmetry along the length of the finite edge: one side of the edge ceases to contribute before the other.

Using the site, first we confirm the behavior of the model as source and receiver positions shift around the wedge. Both the source and receiver begin on the same side of the wedge, then the receiver moves clockwise into the shadow zone.

Figure 4.4: In these figures, S represents the source position, and R the receiver position. The blue line to the right tis the diffracted IR predicted by the BTM mode. We move the receiver to demonstrate the impact on the IR. The direct and reflected waves dominate here. The diffracted contribution attenuates the reflected wave slightly, beginning to smooth the transition to the region without the reflected component from the top of the wedge.

Figure 4.5: In these figures, S represents the source position, and R the receiver position. The blue line to the right tis the diffracted IR predicted by the BTM mode. We move the receiver to demonstrate the impact on the IR. As we approach the shadow zone of the reflection, the diffracted contribution attenuates the specular field.

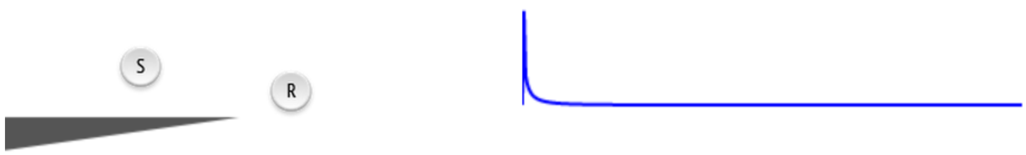

Figure 4.6: In these figures, S represents the source position, and R the receiver position. The blue line to the right tis the diffracted IR predicted by the BTM mode. We move the receiver to demonstrate the impact on the IR. After crossing the boundary, no reflected field is predicted by the specular model, the diffracted field interferes constructively with the direct contribution.

Figure 4.7: In these figures, S represents the source position, and R the receiver position. The blue line to the right tis the diffracted IR predicted by the BTM mode. We move the receiver to demonstrate the impact on the IR. At this position, far from the specular boundaries, the specular model is accurate and diffracted contributions are minimal.

Figure 4.8: In these figures, S represents the source position, and R the receiver position. The blue line to the right tis the diffracted IR predicted by the BTM mode. We move the receiver to demonstrate the impact on the IR. At this position, far from the specular boundaries, the specular model is accurate and diffracted contributions are minimal. However, the sign changes - the specular solution over predicts the solution as we approach the area where the direct field is occluded by the wedge.

Figure 4.9: In these figures, S represents the source position, and R the receiver position. The blue line to the right tis the diffracted IR predicted by the BTM mode. We move the receiver to demonstrate the impact on the IR. Very close to the shadow boundary of the direct sound, the specular solution is significantly attenuated.

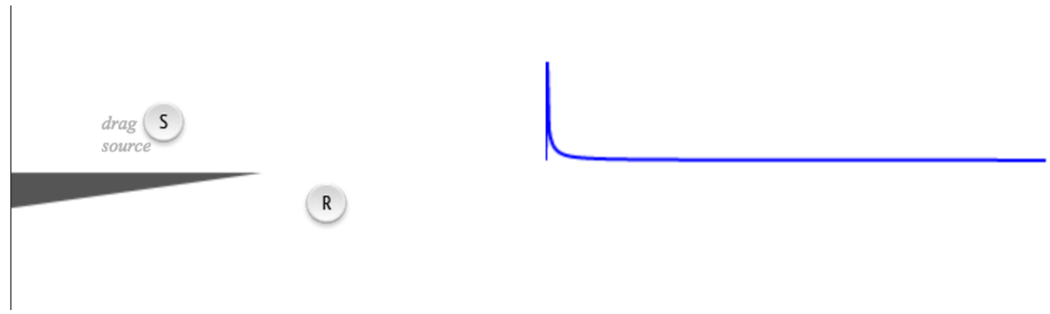

Figure 4.10: In these figures, S represents the source position, and R the receiver position. The blue line to the right tis the diffracted IR predicted by the BTM mode. We move the receiver to demonstrate the impact on the IR. At this position, far from the specular boundaries, the specular model is accurate and diffracted contributions are minimal. However, the sign changes - the specular approximation over predicts the solution as we approach the boundary where the direct field is occluded by the wedge.

Figure 4.11: In these figures, S represents the source position, and R the receiver position. The blue line to the right tis the diffracted IR predicted by the BTM mode. We move the receiver to demonstrate the impact on the IR. Moving clockwise the shadow boundary, the peak amplitude of the diffracted component monotonically decays.

4.3.4 BTM: Practical Implementation

4.3.4.1 Geometrical Tasks

Having shown agreement with published results for one geometrical condition time domain, and demonstrated trends that agree with heuristic behavior and our expectations, let's now go through the steps required to implement this model in our 'Isolated Wall' geometry.

4.3.4.1.1 Extracting Edges from Geometry Having implemented and validated our diffraction model for a single edge, there remains considerable onus with regards to generalizing the model for application in a generalized planar geometry.

When implementing a diffraction model, there are two categories of approach. In one category, the model propagates random distributions of rays in the virtual environment (a monte carlo approach) the calculations outlined above are then potentially executed when a ray a surface on the geometry near an edge. A second category of models could be solved deterministically.

We take the deterministic approach: the first step in computing the diffracted field in a planar environment would be to identify all the edges in the model. While it would be possible to begin by defining the geometry with collections of edges, then connecting those edges into planes for the purpose of the specular model, geometries for acoustic models are more commonly defined by identifying vertices grouped in planes. The algorithm implemented here defines vertices, then identifies all unique edges, lastly computing angle formed by the two planes which comprise each edge.

We begin with an acoustic model of the environment, the model is comprised of a list of vertices (corners) and a list of planes (walls). The plans are of collections of the vertices. Remember, vertices on comprising a plane are ordered according to right hand rule.

1. We iterate through each plane in sequence.

2. We iterate through each edge in each plane.

(a) For each edge, the two lowest number vertices are constructed into a new edge.

(b) The edge contains the following data:

   i. edge identifier (an index)

   ii. solid angle of the wedge the edge forms the apex of

   iii. unique indices representing the vertices (the vertices indices used to create the new edge may be a redundant second identifier). Note, these unique vertice indexes are no longer ordered based on right hand rule and which side of the wall is reflecting, but are instead ordered smallest to largest (index 2 comes before index 11). It is then noted that that the vertices are "right handed" or "left handed". This facilitates our search for redundant or overlapping edges later.

   iv. indices for each of the two planes which come together to form the edge

   v. a vector defining the edge, and normalized vector for the edge are both created

(c) The norm of one of the first of the two planes that meet at the edge is calculated

(d) The edge is then pushed into a linked list of edges via AddEdge();

   i. as edges are added to the linked list, they are placed where they belong in the list sorted by their first vertex indices.

   ii. if the edge has the same first vertex index, its sorted based on the value of the second vertex index

   iii. if an edge shares the same first and second vertex as another, this is due to the fact that (for a perfectly defined geometry) each edge arrises twice, once in each of the two planes that comprises the edge. In this case, the second plane noted in the structure containing the data for the edge. If the second plane has already been defined, an error is flagged.

3. Now that each unique edge is identified, they are sorted based on the unique

vertices they are comprised of, and paired with the two planes which join to form the edge, the surface normal of the second edge is calculated and stored.

4. Lastly, the solid angle of each wedge (comprised of the two planes meeting at the edge) is calculated and stored.

4.3.4.1.2 First Order Diffraction The specular field simulations in Chapter 3 is more mature, and written more generally than the edge diffraction code. Q/A testing with manually input source and receiver positions for validity and audibility was required to ensure no corner cases returned incorrect validity or audibility results. In the case of the diffracted field, the semi-analytical solution at a single receiver is easily calculated from a single point source with the equations expressed in Section 4.3.1. That diffracted contribution is effectively a line source, that is a collection of point sources, from the entire edge of the occluder. A more mature simulation would expand the contribution into many point sources distributed along the edge, each possessing a segment of the edge corresponding a sample period in propagation distance. As such, visibility testing would be more involved: one must test visibility for each of the point sources in the line source. Additional complication arises because these sources exist on the surface of the geometry.

A decision was made to limit the scope of this current work to first order diffraction, omitting the edge diffraction visability test and asserting what we know about visibility and occlusion manually in the simulation.

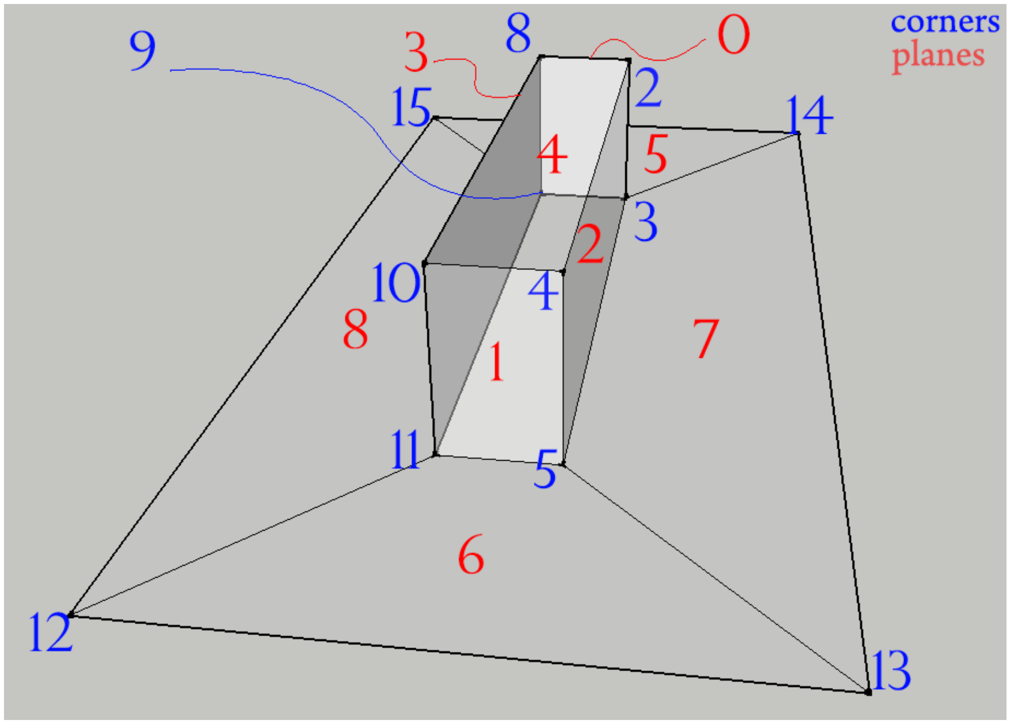

Figure 4.12: This image offers identifies corners and planes in the Isolated Wall geometry. The right side of the wall corresponds to approximately east, and is the side from which the sonic boom is incident. This was useful for asserting known visibility conditions on the first order diffracted simulation.

With the wavefront incident from the east, or the right side of the wall in the image above, Plane 7 receives the first order diffracted contribution from the edge with vertices 2 and 4. Plane 7 also receives the incident wavefront. Plane 8 is partially in the shadow zone and receives a first order diffracted contribution from the edge with vertices 8 and 10.

4.3.4.2 Validation of Scaling Factors

While the reproduced figure of the time domain IRs agrees with the published figure, the published figure lacks the 0^{th} sample. The sampling rate was un-specified and chosen simply to force time domain agreement. The S variable in the BTM equations went undefined. The time domain pressures are too high to be meaningful without context.

Let's address all these questions by returning to first principles and finding agreement in the frequency domain.

4.3.4.2.1 Definition of Source Strength In Sections 4.3.1, and 4.3.3 we discovered that S in the BTM equations went undefined. Let us begin by assuming that it is consistent with a historically typical representation of acoustic source strength. This justifies a step back to briefly review a common use and definition of this symbol in acoustics.

The amplitude of the pressure generated by a time harmonic source (with arbitrary shape and surface velocity), in an arbitrary environment may be described as such:

$$P(\vec{r}) = S(\omega)G(\vec{r}|\vec{r_s}), \tag{4.17}$$

Where $\vec{r}$ is the position vector to the field point where we are observing the pressure, and $\vec{r_s}$ is the position vector to the source. In equation 4.17, $S(\omega)$ accounts for volume velocity over the sources area at each frequency, and the Green's function $G(\vec{r}|\vec{r_s})$ accounts for the acoustic relationship between the source and receiver positions in space, including the effects of any scatterers in the environment.

In the free field, the Green's function reduces to:

$$G(\vec{r}|\vec{r_s}) = \frac{e^{-jkR}}{R}, \text{ where } \vec{R} = |\vec{r} - \vec{r_s}| \tag{4.18}$$

As mentioned, $S(\omega)$ is the frequency domain representation of the derivative of the source strength and is defined as follows. The source strength is given by the following integral.

$$q(t) = \int_S \vec{v}(\vec{r_s}, t) \cdot \hat{n} dS. \tag{4.19}$$

$q(t)$ is the instantaneous integration of the normal component of the surface velocity over the radiator's surface, and is called the "Source Strength".

In the free field, the relationship between pressure at a field point r, and source strength $q(t)$ of a compact acoustic source at the origin is given by:

$$p(\vec{r}, t) = \frac{\rho_o \dot{q}(t - r/c)}{4\pi r} \tag{4.20}$$

For time harmonic monochromatic sources, this may be rewritten, isolating the time varying portion $e^{j\omega t}$, and the frequency dependent amplitude $Q(\omega)$ as follows:

$$q(t) = Qe^{j\omega t} \tag{4.21}$$

In the free field, the pressure amplitude generated by a monopole, continuous wave, compact acoustic source (dimensions are much smaller than a wavelength) may be described as follows after considering Fourier decompositon:

$$S(\omega) = \frac{\rho_o \dot{Q}(\omega)}{4\pi} = \frac{j\omega \rho_o Q(\omega)}{4\pi} \tag{4.22}$$

$$P(\vec{r}, \omega) = \frac{\rho_o \dot{Q}(\omega)}{4\pi} \frac{e^{jkR}}{R} \tag{4.23}$$

.

4.3.4.2.2 An Argument for a Time Domain Scaling Factor We've demonstrated that our implementation of the BTM equations successfully reproduces the results found in our sources.

However, when looking at the validation plots in Section 4.3.3, it's counter-intuitive that pressures at field points due to an impulsive source ("delta function acceleration source") exceeds 1 [Pa]. This confusion is exacerbated by the label on the abscissa - "Relative Pressure". The natural question is, is this the absolute pressure due to a delta function acceleration source, or has it been scaled by some value?

This question is resolved by reviewing the earlier reference by the same authors, written in 1980 [45]. This document clarifies that the "delta function acceleration point source" in the free field, emits the pressure given by:

$$p = (\rho S/4\pi R)\delta(t - R/c) \tag{4.24}$$

Relating, the time domain solution relative to a free field impulse. In the case of the time domain wedge diffraction calculation we used for validation. Was $R = r_o + r = 200[m]$ away. Using equation 4.24, the source excitation

$$p(\tau)_{\text{free field}} = 4.7 \times 10^{-4}\delta(\tau)\ [Pa]. \tag{4.25}$$

We expect an IR without constructive interference to only possess values less than 1. Dividing by the inverse of the the free field path amplitude increases the diffracted pressure even further.

While not explicitly documented in either source [45] [43], the required scaling factor comes from multiplying by the sampling period. Scaling by the sampling period results in absolute pressures, this is due to the fact that the initial source was defined as a "unit volume acceleration" over one sample. We must effectively multiply the output IR pressure by the discrete $\delta(\tau)$ in the above expression. Let us build confidence in this thinking by reproducing the frequency domain results.

We matched the time domain IR in Figure 4.2a to validate our implementation of the BTM expression, in order to be sure that our solution is accurate, we must also accurately match the frequency content as well.

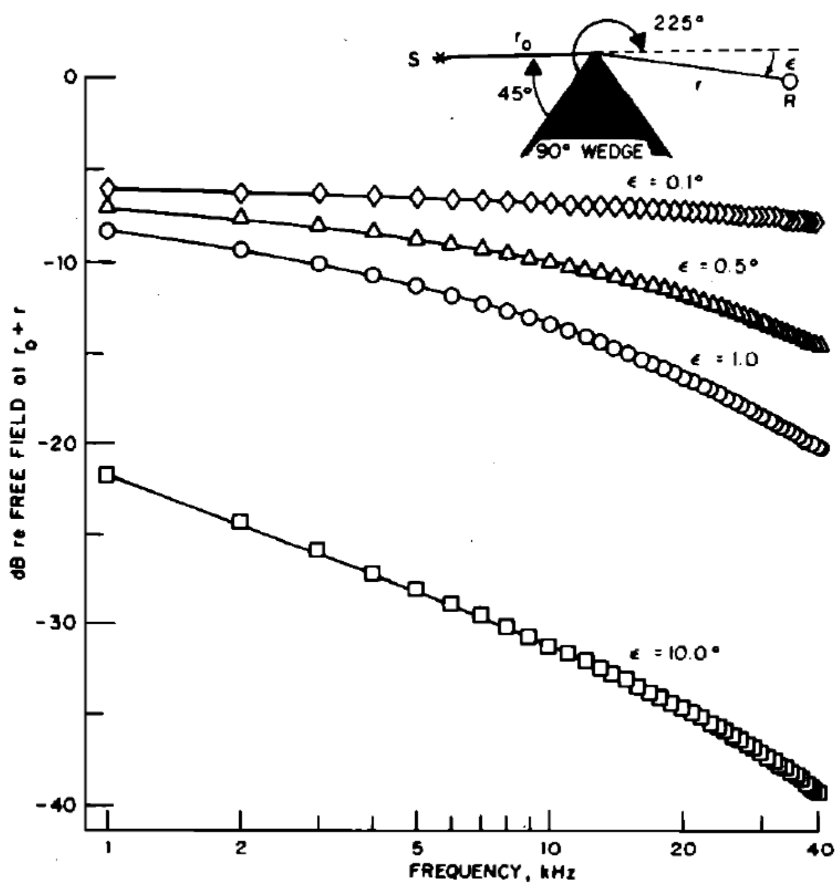

Figure 4.13: The curves in this figure from [43], are the power spectral density of the transforms of the curves in Fig. 4.2a By calculating the spectra of the free field excitation given by Eq. 4.24, and then calculating diffracted component, their ratios offer the insertion loss of the barrier. That is, the ratio of the spectra relates the power of the diffracted component to the power of the free field excitation at the field point.

Figure 4.2a is actually a bit deceptive, in that it does not show the value of the IR at $n = 0$. The omitted initial sample shapes the frequency content. If the initial sample has a very high amplitude relative to the rest of the impulse response (IR), then the frequency content will be quite flat (this is the case near the shadow boundary).

A second facet that is somewhat unclear, is whether the spectra shown in Figure 4.13 is gleaned from the instantaneous IR values, or the averaged values. It's notable that the first sample of the IR is infinite when calculated instantaneously. Given the significance of the first sample, it's assumed that the frequency content shown in was obtained with average values, as that is the only way to arrive at a finite initial sample.

The plots below show the frequency content of the diffracted path using the instantaneous pressure, and defining the initial sample as equivalent to the second sample. The point of the following plots is to demonstrate that scaling by the sampling period brings the frequency content into the correct order of magnitude. In the subsequent paragraph, we will calculate the IR by averaging over a sampling period, and this will have an accurate pressure for the zeroth sample.

Without scaling by the sampling period, the corresponding spectrum is below:

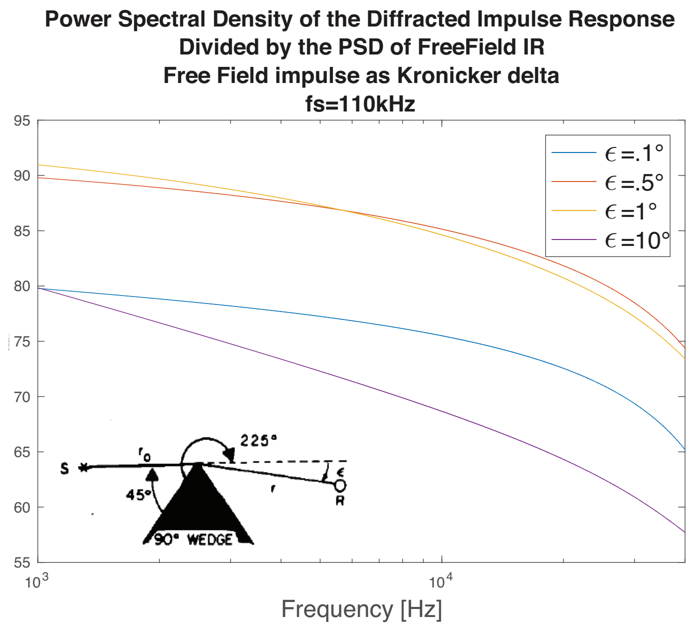

Figure 4.14: BTM Diffraction Model - Initially Simulated Power Spectral Density: This figure should agree with that reproduced in Fig. 4.13. It's apparent that agreement in the 1st-5th samples of the time domain does not guarantee agreement in the frequency domain. 90 *dB is much greater that 0 dB, and we expect our first order diffracted field to possess a magnitude substantially less than the free field.*

These plots are "relative pressure" that is, relative to the free field. After scaling the free field pressure by the sampling period, or synonymously, dividing by the scaling factor given by equation 4.26, the spectrum is as follows:

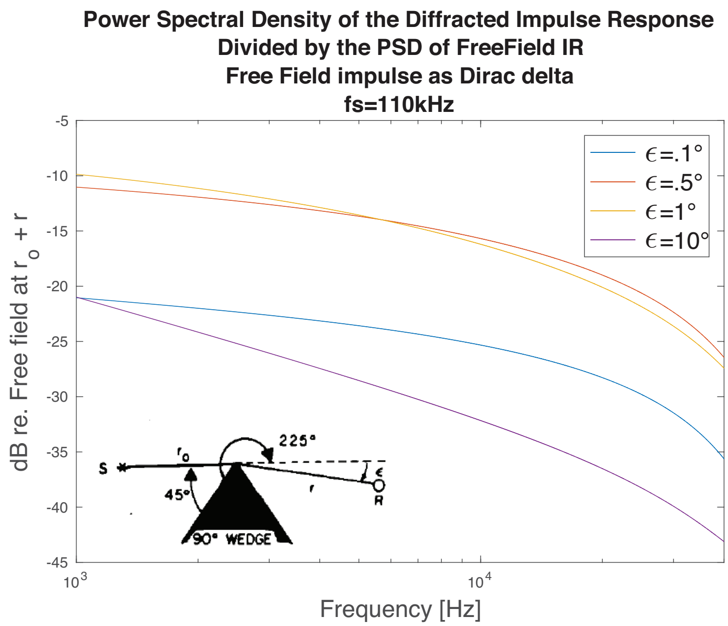

Figure 4.15: BTM Diffraction Model - This figure should agree with that reproduced in Fig. 4.13. Simulated Power Spectral Density after Scaling: scaling has brought us into the correct order of magnitude, but the curves don't match well.

Knowing the significance of the first sample in the spectral shape, and how the amplitude of the first sample increases with sampling rate we employ trial and error to find a sampling rate that results in agreement with the published spectra.

After scaling by the sampling period, and dramatically increasing the sampling rate the spectrum is as follows:

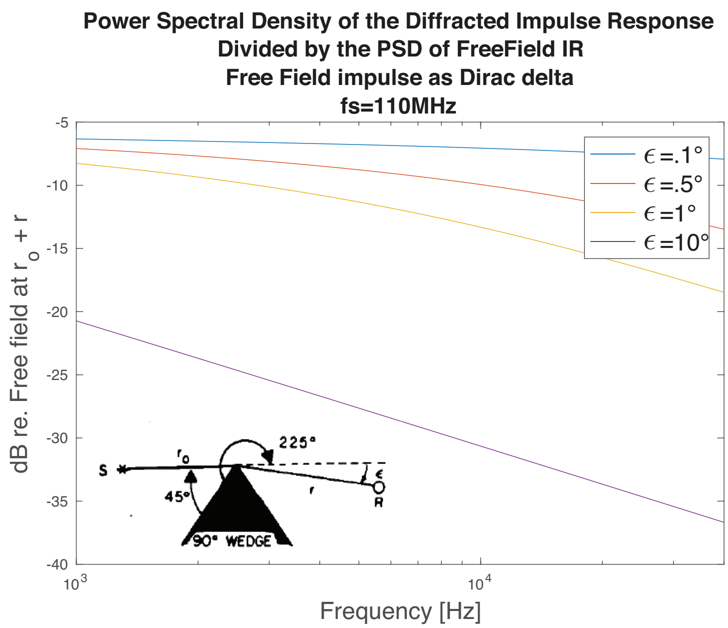

Figure 4.16: BTM Diffraction Model - Validated Power Spectral Density, after scaling, and with increased sample rate. For comparison with Fig. [?].

This begs the question: do the curve converge? Increasing the sampling rate beyond 110 MHz to the range of Terra Hz does not significantly change the spectrum.

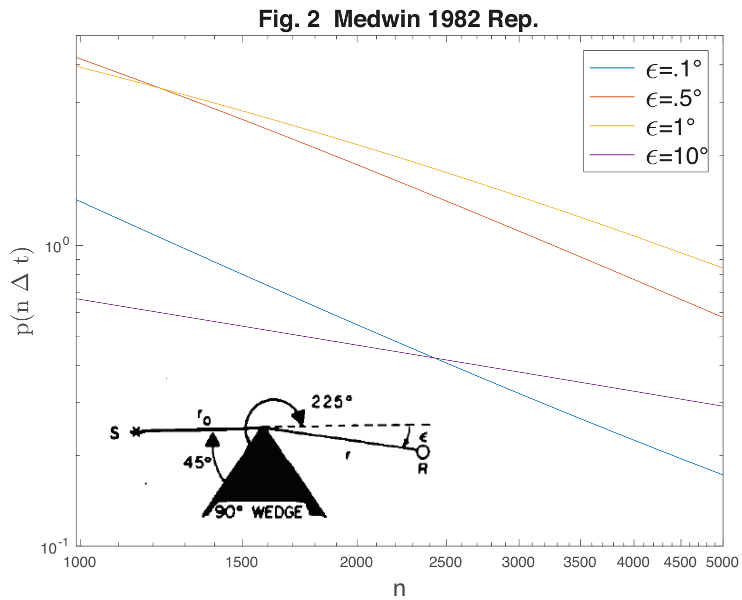

Figure 4.17: BTM Diffraction Model - Validated Power Spectral Density, after scaling, with a increased sampling rate. For comparison with Fig. 4.2.

Before we close this portion, lets briefly return to the time domain signal to regain our bearings. Recall we began the validation of our time domain model by reproducing a published IR in Figure 4.2, before discovering that agreement between the shown samples in the time domain was insufficient for validation. That same time domain "Relative Pressure" plot is reproduced in Figure 4.17 with the higher sampling rate.

In the generation of these validation curves the frequency domain plot was divided by the free-field spectra, the time domain curve was not. The time domain curve gives the pressure at the receiver location, for a unit volume flow (basically a Heaviside function of volume velocity) yielding a free field pressure of $p = (\rho S/4\pi R)\delta(t - R/c)$ at the receiver position. Again, the time domain pressure shown in Figure 4.17 and reproduced for validation does not include the scaling by sample rate OR time domain free-field impulse amplitude.

This unaltered IR would be ready for convolution quantifying the signal path from spherical source to edge to receiver. However our application is distinct since our source is a plane wave. The next section addresses this distinction.

4.3.4.2.3 Conclusion Regarding Scaling Factor: Spherical Source Our goal is to separate the IR from the excitation, meaning our free field IR should be a *dirac delta*, such that convolution of the free field IR with the incident wavefront yields the incident wavefront.

In our exhaustive study of source strength, samplings rates, and scaling factors we've discovered the following: The agreement achieved in Figure 4.16 was only achievable with the following scaling term. The BTM solution is plotted in reference to an impulse of the following magnitude, the impulse with this magnitude is the free field pressure due to volume uniformly and continuously injected, beginning at time $t = 0$:

$$ScalingTerm = \frac{\rho S}{4\pi(r_o + r)\Delta t} \tag{4.26}$$

Where $S = 1$, the density of air $\rho = 1.2$ [kg/m^3], and Δt is the $1/fs$ where fs is the sampling rate.

Comparing this to equation 4.20 in our exploration of source strength, we find that in reference [43], $S = \dot{q}(t - r/c)$. It's conceivable that the Δt could fall out of the discrete derivative of the volume velocity (which takes the form of a Heaviside or Step function), but then it would be included within S.

We also notice that the Δt term is missing from the published expression for free field pressure.

The Δt scaling term invites further curiosity in that equation 4.24 was also offered. It is possible that the Δt term is implied in equation 4.24, as the Δt scaling term is what distinguishes *Dirac* and *Kronicker* delta functions.

Whether the Δt term falls out of a derivative, or the difference between delta functions, we must divide our Impulse Response by the $ScalingTerm$ for consistency with a free-field Impulse Response that is a *Kronicker* delta. An IR divided by $ScalingTerm$ is appropriate for convolution with the incident waveform that would reach the receiver position in the free-field.

We will discover in Chapter 6 that the BTM solution under-predicts the diffracted field in our application. It is tempting to doubt, or consider modifying this scaling term. However this scaling term gives the accurate transfer function relating the free-field source strength and diffracted impulse.

4.3.4.2.4 BTM: Plane Wave Compensation Recall that in Sections 2.1, we discussed modeling the planar wavefront as a very distant spherical source. In doing so, we introduce a very large propagation distance as r_o goes to infinity. The IR for the diffracted contribution given by the equations in Section 4.3.1 is accurate for the given values of the propagation distance, r_o. That is to say, that this value captures not only the shape of the wavefront, but controls the amplitude of the diffracted contribution.

Fortunately for us, when we divide our IR by Eq. 4.26, we already include this compensation.

Care should be taken such that r_o is large enough that the scaling term converges throughout the geometry.

4.3.4.2.5 BTM: High Sample Rates & the Least Time Path Sample This section may be ignored with regards to practical implementation, but it does address some facts surrounding the high sampling rate utilized to obtain good agreement.

As mentioned above, what is deceptive about the time domain validation plot in Figure 4.2a, is that the least time sample, meaning $p(n\Delta T)_{n=0}$ is not shown. This omission is particularly devious, because:

1. The value of this first sample has a significant impact on the magnitude in the frequency domain (it's the most energetic sample in the Impulse Response).

2. The value of the first sample also has a significant impact on the overall shape of the IR; what is impulsive in one domain is flat in the other.

Medwin offers two ways to compensate for this.

1. Solve for the 0th sample using the expression below, knowing this is not accurate near the shadow boundary.

   Under the conditions where the receiver field point is not near a shadow boundary, the least time sample is given by [43]:

$$p(n\Delta t)_{n=0} = \beta\sqrt{\frac{2}{\Delta T}} \tag{4.27}$$

   However, this 0^{th} sample is most significant near the shadow boundary, so such an expression has limited utility.

2. Solve the BTM Model with a higher sampling rate, and average many samples around each sample of actual interest. With averaging over each sampling period, the IR is calculated by averaging the instantaneous diffracted pressure over the following windows: $n\Delta T - \frac{\Delta T}{2}$ and $n\Delta T + \frac{\Delta T}{2}$. This offers a finite value for the where $n = 0$ sample, as we let $p(\tau) = 0$ for $\tau <= 0$.

Having seen that a very high sampling rate results in good agreement, we use the following approach. We solve the BTM equation discretely at a very high sampling rate (120 MHz), and then down-sample to 48 kHz by averaging all the samples within the new Δt. The method used to sample the continuous analytical solution can drastically change the spectra or time domain signal. The Matlab script used to demonstrate the validated signal processing to obtain a useful diffracted Impulse Response is presented in Appendix E. Appendix E also includes the application of this approach to obtain the results presented in the Section.

4.4 Microphone Position Simulation Results

4.4.1 Simulated IRs

What follows are the simulated IR's for the three microphones in close proximity to the wall.

The total pressure waveform at each microphone position is the sum of multiple specular paths, and multiple diffracted paths, and some paths which include both specular reflection and diffraction. The theory used to combine these paths is discussed in more detail in Section 6.3. Here we show the diffracted paths and specular-diffracted which must be calculated before thoughtfully combining the contributions.

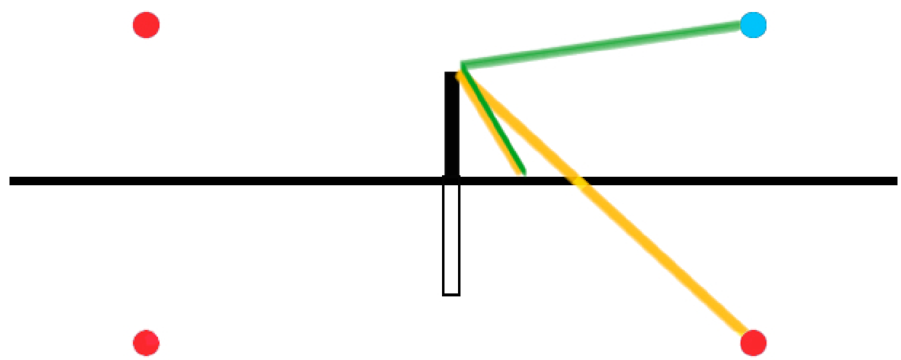

Figure 4.18: This figure illustrates two of the four paths, which include 1st order diffraction, incident at microphone 202. The green path is the Edge Diffracted path, and the yellow path is a path which is first specularly reflected, and then diffracted off the edge. Note, that each of these paths may then be specularly reflected by the ground. Due to the fact that our microphones are placed on the ground, all diffracted paths at this microphone (202) can be captured by calculating the waveforms from these two paths, doubling them, and then superimposing the results.

The impulse response are the simplest diffracted simulations possible, modeling the edge as infinite in length. These IRs have been divided by the scaling factor presented in 4.3.4.2.3.

One intention of this section is to improve our intuition regarding the sign of the impulse response. Recall that the effective function of the diffracted contribution is to smooth the transition between the where specular reflections are present, and the shadow zone. When we are presented with a source, and a diffracting edge, specular reflections are generated by the faces comprising the edge. Recalling our discussion of "Field Angles" and shadow zones in Chapter 3, identify whether a reflection off plane that forms the diffracting edge will reach the microphone. If it does, expected a negative diffracted impulse response. If the microphone is in the shadow zone of that reflection, expect a positive impulse response.

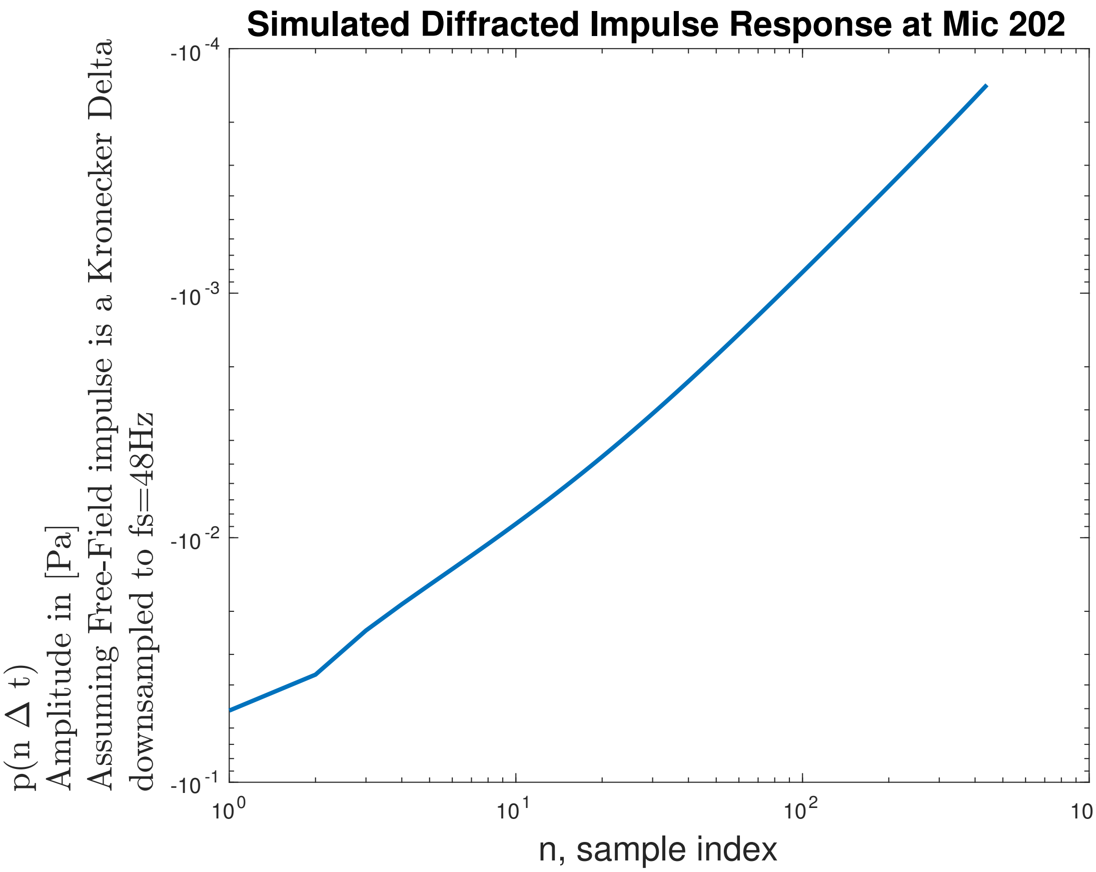

Figure 4.19: Simulated Diffracted IR - Mic 202: Diffracted from the eastern edge of the wall

It's notable that this impulse response is negative, this is what we expect, since microphone 202 is illuminated by the reflection of the original source off the wall that forms the diffracting edge. As such the diffracted contribution negates some of the incident pressure, smoothing the transition into the shadow zone.

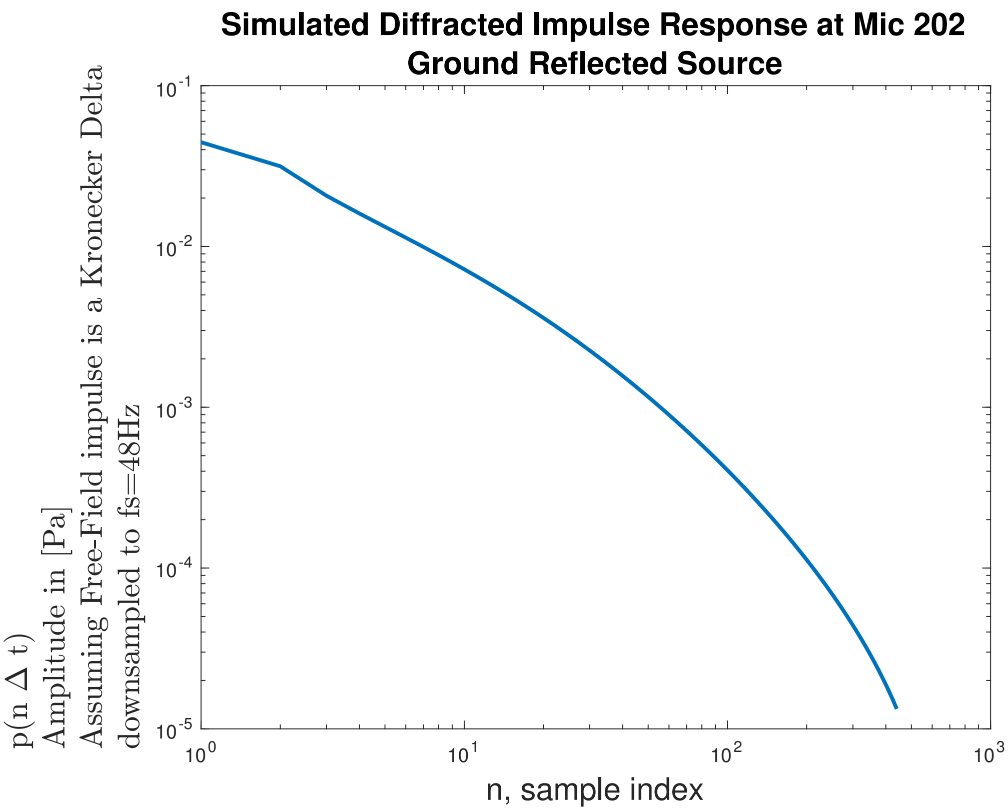

Figure 4.20: Simulated Diffracted IR - Mic 202 - From Ground Reflected Source: Diffracted from the eastern edge of the wall

Unlike the diffracted contribution from the original source, the diffracted contribution from the specularly reflected source, is positive. If we were to begin with the ground reflected image source, and then visualize the specular reflection (of the image source representing the ground reflection) off the wall forming diffracting edge, we would would see that Mic 202 is outside the "Field Angle" and in the shadow zone. As such the diffracted contribution is expected to be positive.

Microphone 203 is an outlier, as it rests on top of the wall. In this circumstance, since the surface that the microphone is resting on is one of the planes of the diffracting edge, we do not double these impulse responses or waveforms to account for subsequent specular reflection.

Another distinction of microphone 203, is that it's significantly impacted by two diffracting edges. As such there are three paths which include 1st order diffraction that require calculation to predict the pressure waveform at this location.

The resulting waveforms after convolution are also distinct in shape, and higher amplitude, due to the fact that the microphone is so close to the edge, and on one of the surfaces forming the edge.

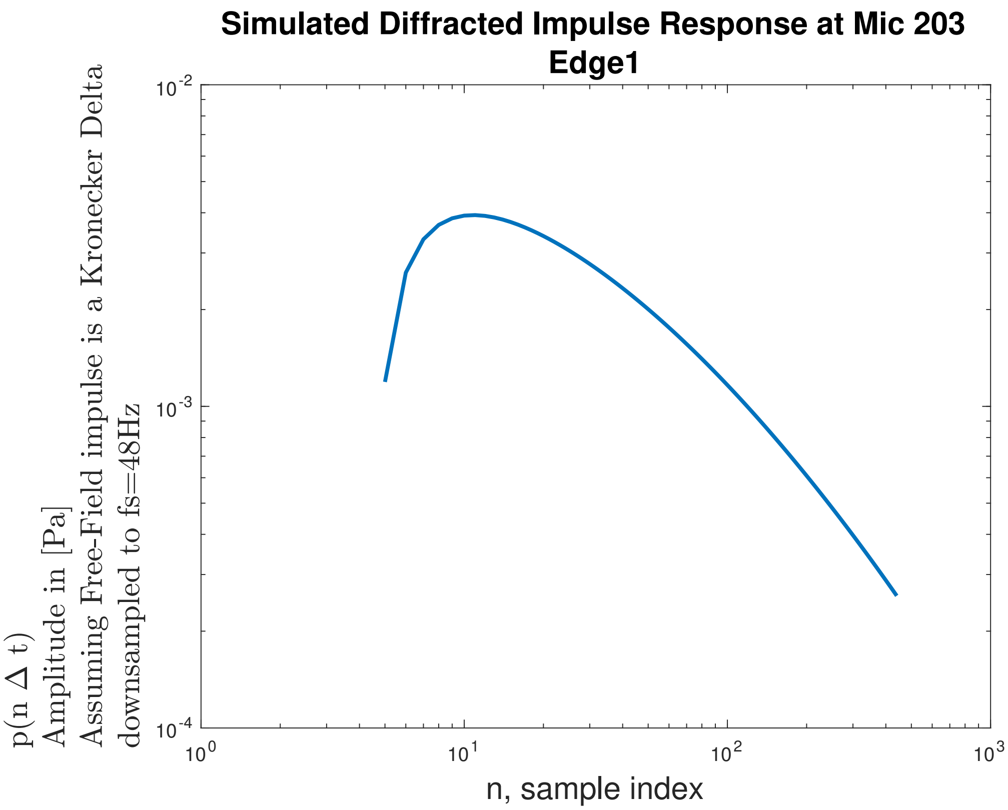

Figure 4.21: Simulated Diffracted IR - Mic 203: Diffracted from the eastern (incident) edge of the wall

Note that there is no ground reflected source incident upon the western edge, since it would be occluded by the eastern edge. Second order diffracted paths are

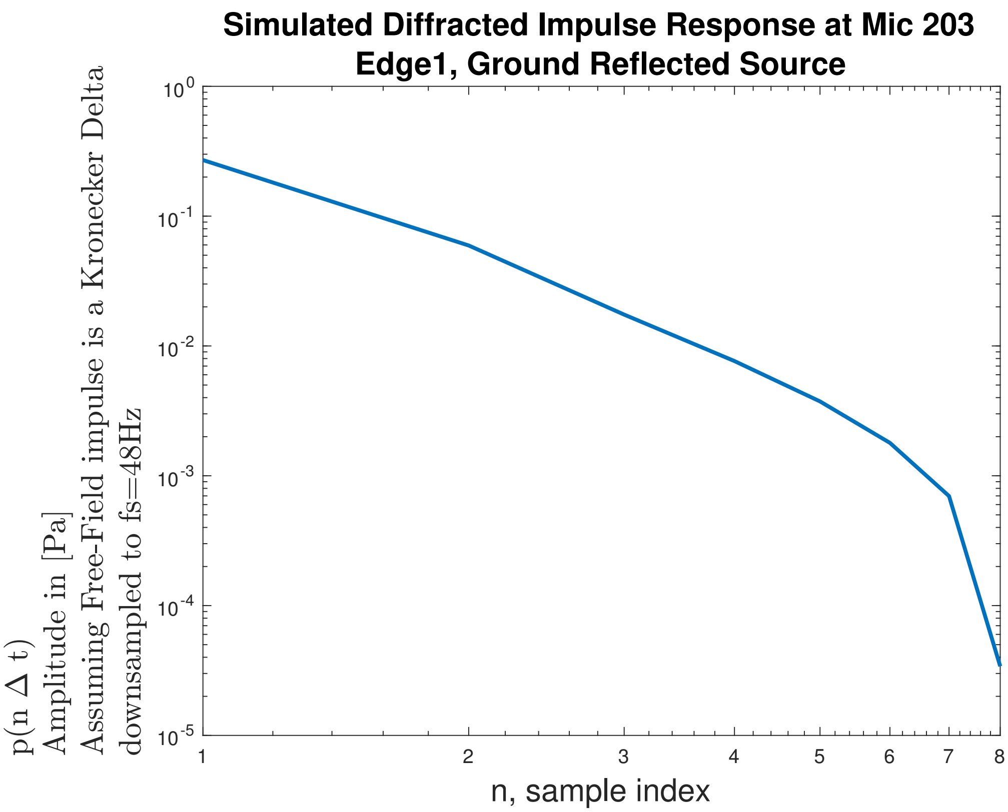

Figure 4.22: Simulated Diffracted IR - Mic 203 - Ground Reflected Source: Diffracted from the eastern (incident) edge of the wall

lower amplitude, and omitted as they are out of the scope of this paper.

Microphone 201 is very similar to microphone 202. The main distinction being that the direct path and ground reflected path are both occluded. As such, both diffracted paths are positive.

It's notable that, since 2nd order diffraction was omitted in this work the wall was approximated by a single edge when solving for microphone 202 and 201.

While both IRs calculated for microphone 201 appear identical, it was confirmed that they are distinct.

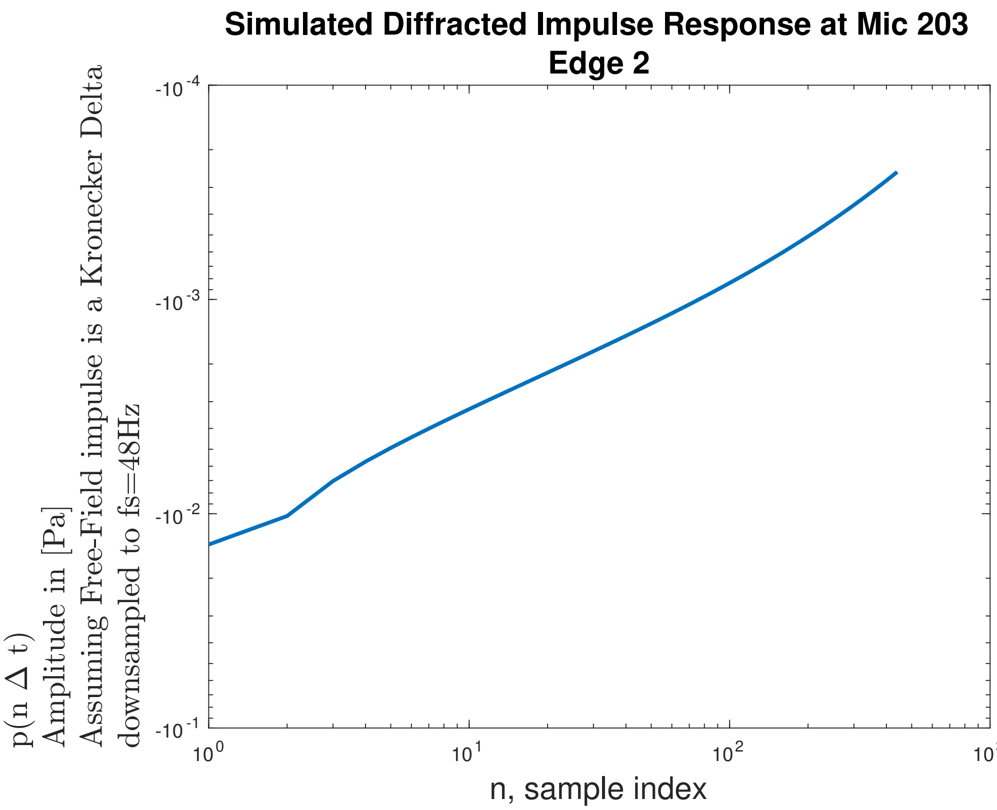

Figure 4.23: Simulated Diffracted IR - Mic 203: Diffracted from the western (non-incident) edge of the wall

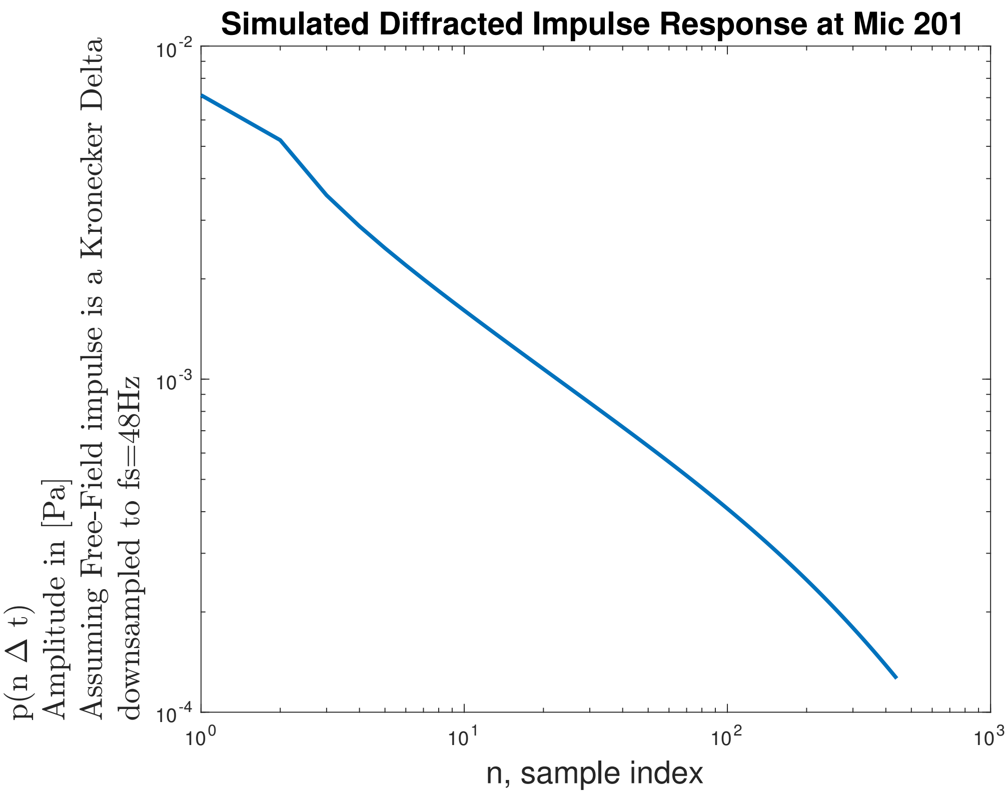

Figure 4.24: Simulated Diffracted IR - Mic 201: Diffracted from the western (non-incident) edge of the wall

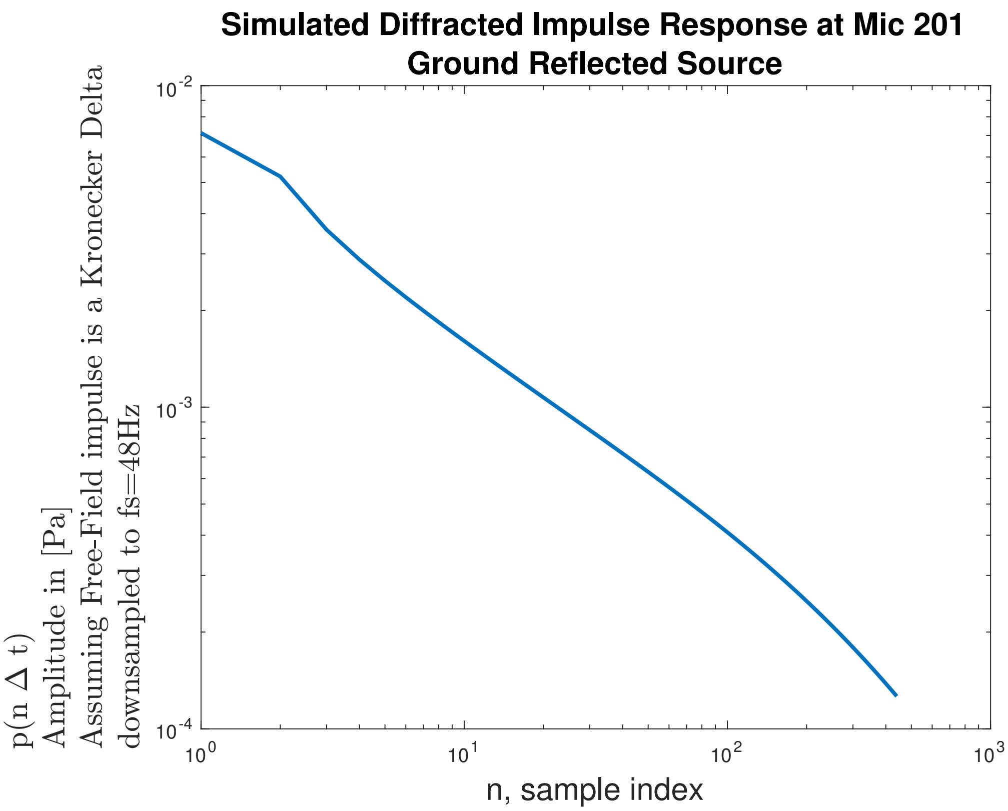

Figure 4.25: Simulated Diffracted IR - Mic 201: Diffracted from the western (non-incident) edge of the wall

In Summary, these IRs confirm the following expected trends:

1. Microphone positions occluded from the original source by the diffracting plane exhibit positive IRs

2. When the source is not occluded by the wall, and a specular reflection of that source off the wall illuminates the microphone, the Impulse Response will be negative

3. Microphone positions further from the edge have more gradual decays, and will contain more low frequency content. This can be seen by looking at the units of the time axis.

Next we convolve them with the incident waveform to obtain the diffracted booms.

4.4.2 Simulated Diffracted Boom Waveforms

In this section, we give the simulated waveforms required to account for all paths including up to 1st order diffraction. These figures are generated via convolution of the IRS in the previous section, with the incident waveform approximated from measurement at microphone 188, discussed in Section 5.2.3.

The pressure at Mic 203, centered on top of the wall is approximated by diffraction off both edges. The simulated waveforms at microphones 202 and 201 were doubled, to account for subsequent specular reflection, since the microphone positions were on the ground surface, where as microphone 203 is on the surface of a diffracting plane comprising the edge.

The waveforms presented in this section, are superimposed with the specular contributions in Chapter 6, approximating the total pressure scattered by the wall, at each microphone position.

Recall that the input waveform exhibited a maximum pressure of 35.6 [Pa] , and a PLdB of 92.6. As PLdB is determined by rise time, and since the diffracted IR is a decay, convolution with the exponential decay will typically smear the incident shock in time - lowering the PLdB.

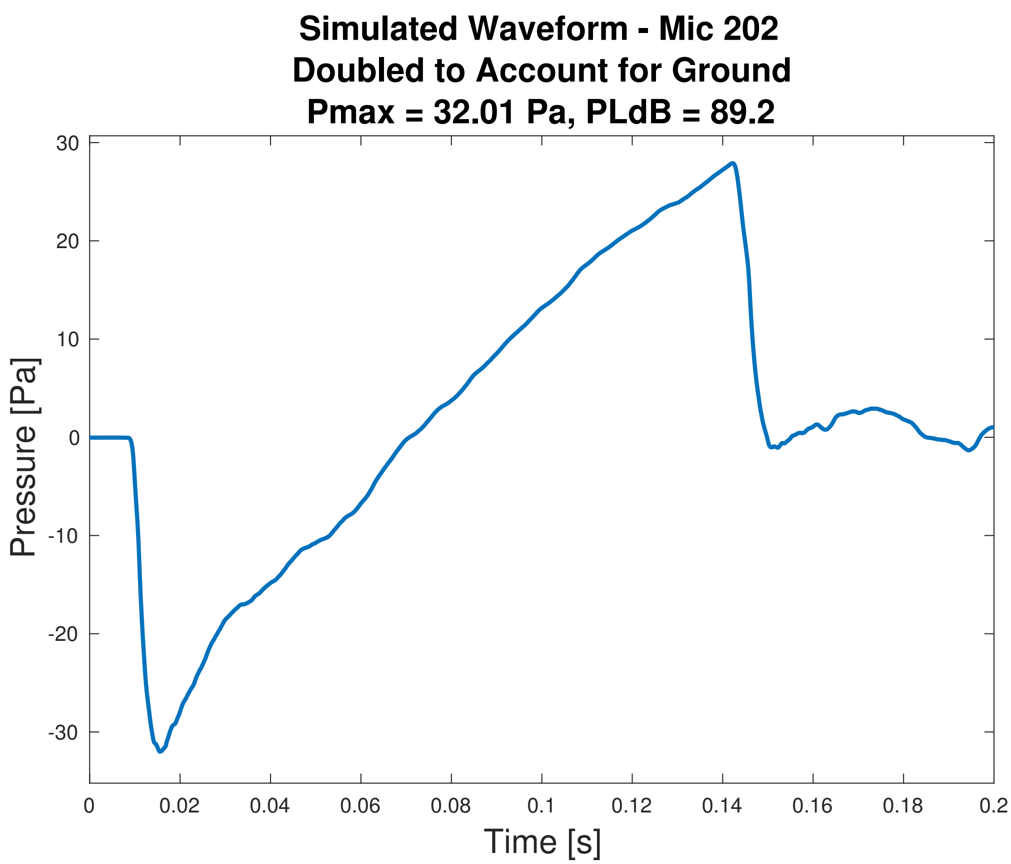

Figure 4.26: Simulated Diffracted Waveform - Mic 202: Diffracted from the eastern (incident) edge of the wall

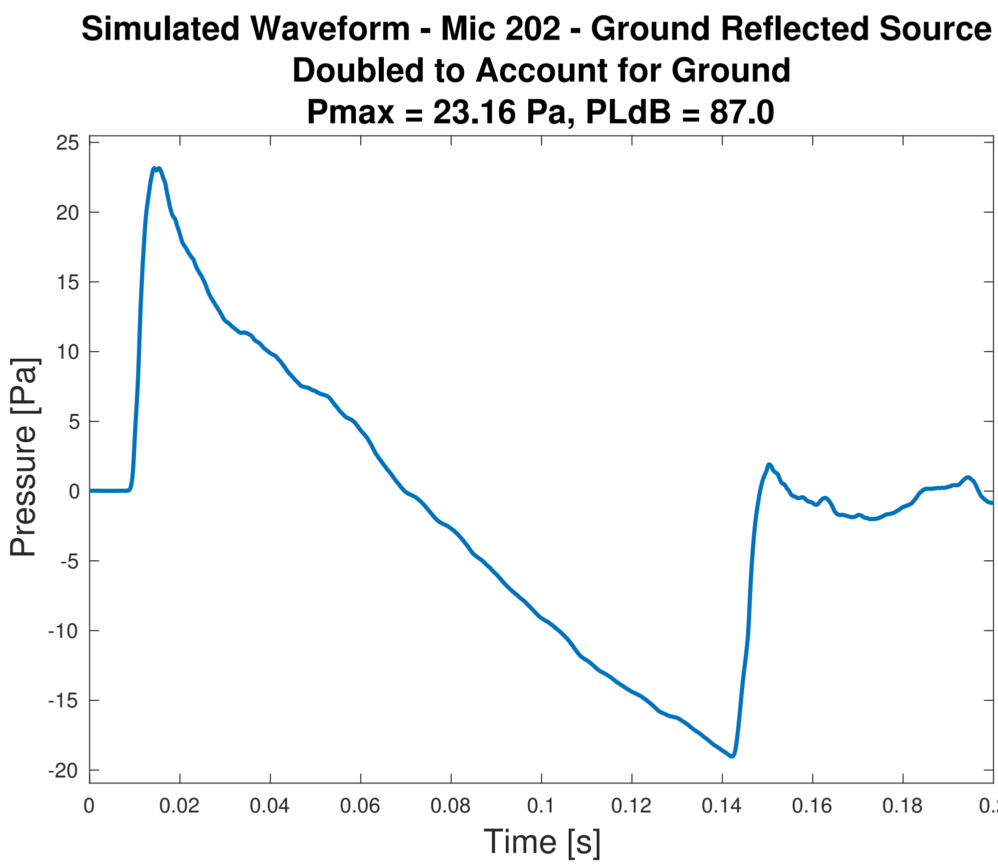

Figure 4.27: Simulated Diffracted Waveform - Mic 202 - Ground Reflected Source: Diffracted from the eastern (incident) edge of the wall

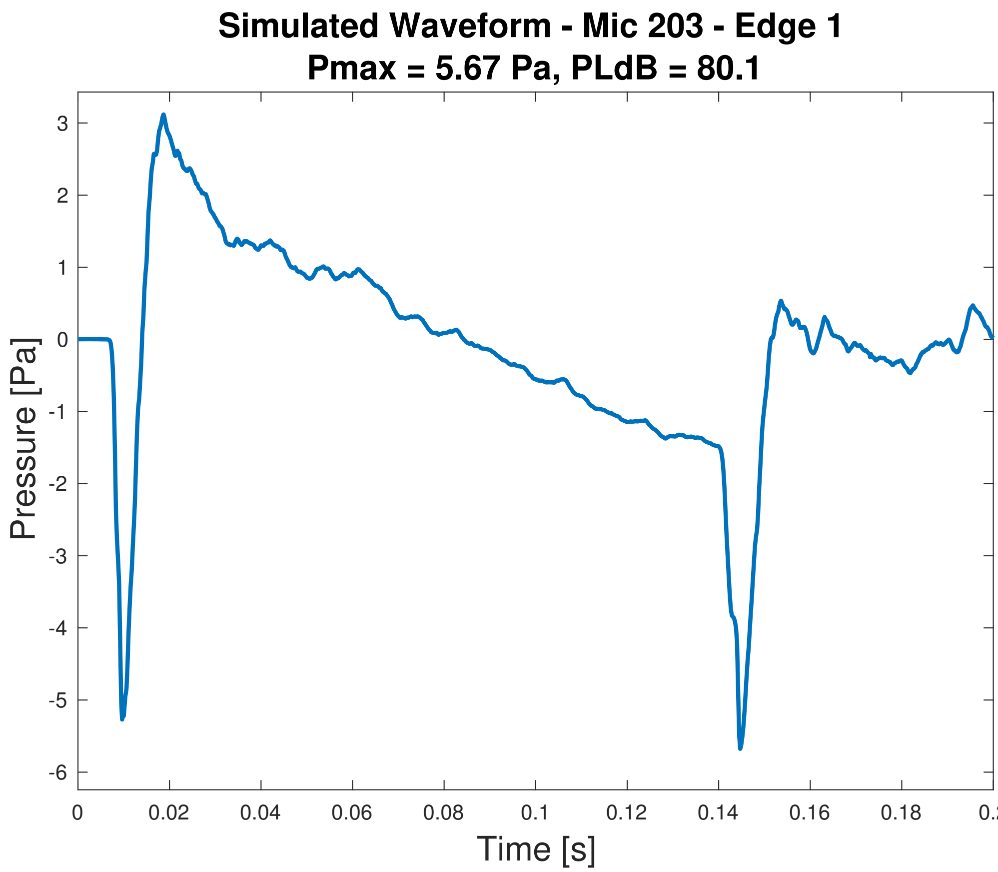

Figure 4.28: Simulated Diffracted Waveform - Mic 203: Diffracted from the eastern (incident) edge of the wall

Microphone 203 on top of the wall (shown in Fig. 5.7) receives three first order Diffracted contributions. Due to the proximity to the edge, the IR decays very quickly, this results in very little smearing to the shocks, and preserves the high PLdB, despite the low maximum pressure.

Recall that we omitted diffraction from on the western edge of the ground reflected source, as the ground reflected source is obscured by the eastern edge.

The initial arrival time of these diffracted contribution reflects the simulated distance of 31 [km] to the spherical source, for approximation of a plane wave. The time domain waveforms were time aligned such that $t = 0$ s is the moment that the direct sound would have arrived in the free-field. Observing the diffracted contributions in isolation is informative, but not particularly representative of the final maximum pressures and PLdB. Superimposing the time aligned specular and

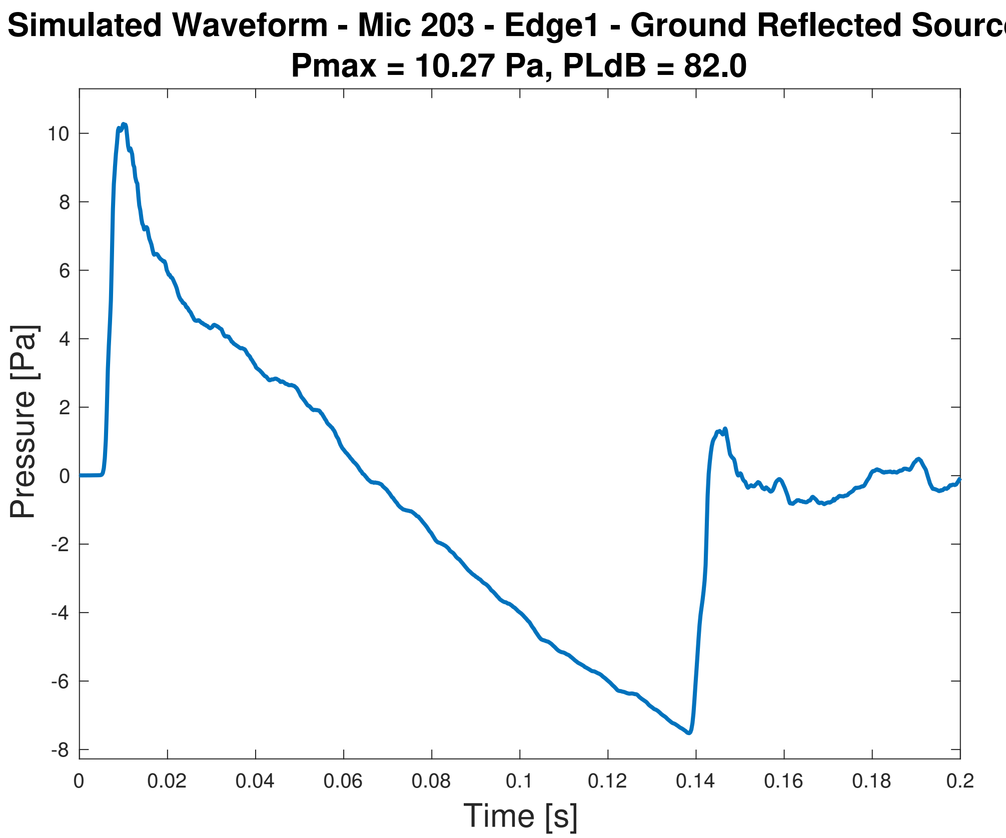

Figure 4.29: Simulated Diffracted Waveform - Mic 203: Diffracted from the eastern (incident) edge of the wall

diffracted contributions allows us to observe interference between the two contributions. These results are presented in Chapter 6.

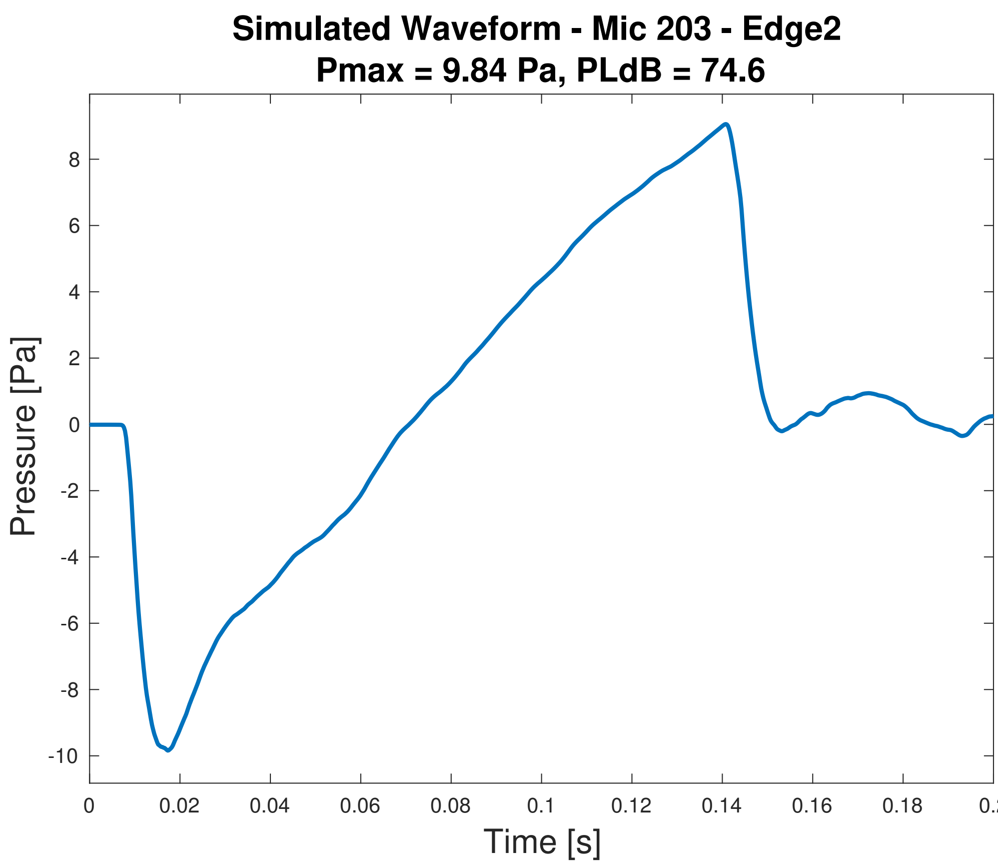

Figure 4.30: Simulated Diffracted Waveform - Mic 203: Diffracted from the western (non-incident) edge of the wall

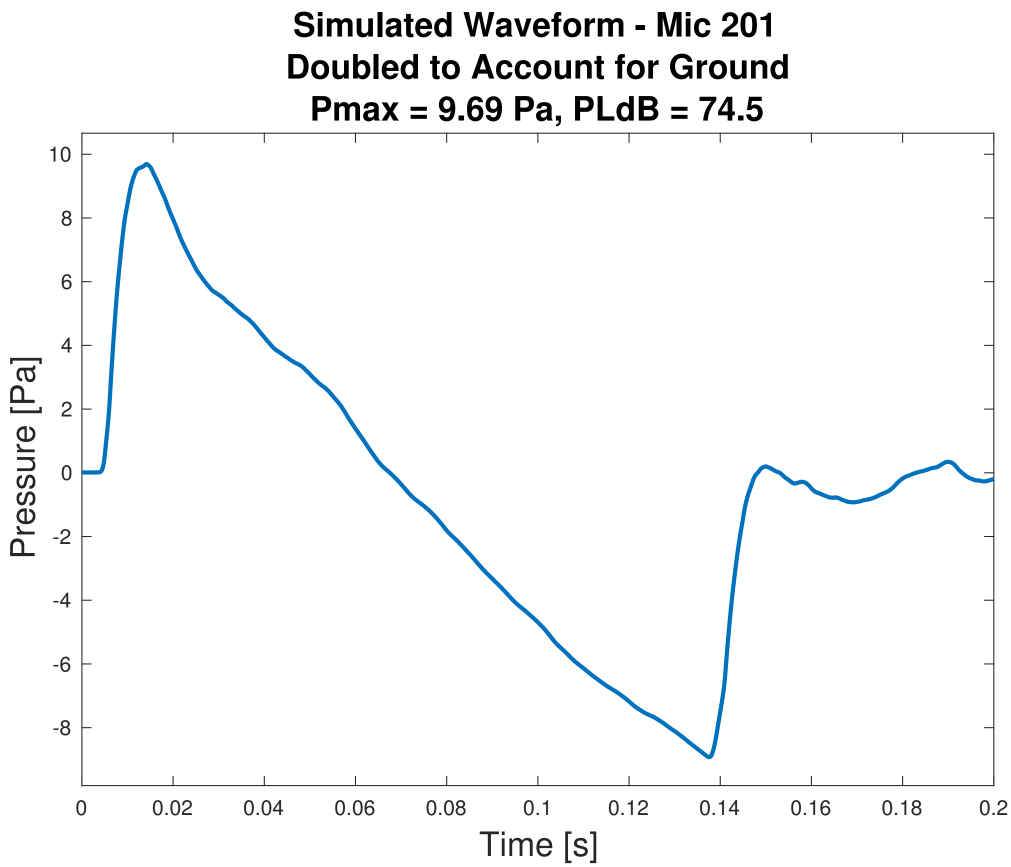

Figure 4.31: Simulated Diffracted Waveform - Mic 201: Diffracted from the western (non-incident) edge of the wall

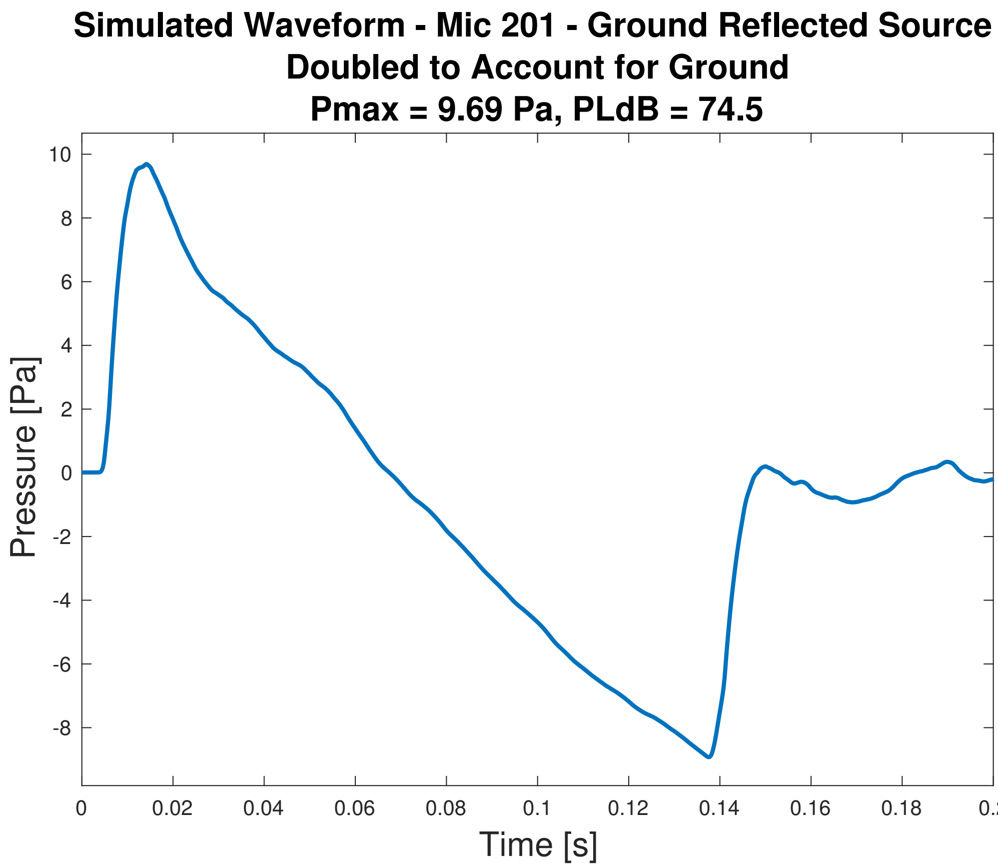

Figure 4.32: Simulated Diffracted Waveform - Mic 201 - Ground Reflected Source: Diffracted from the western (non-incident) edge of the wall

Thus far we've illustrated the multiple diffracted paths acting on each microphone position. Before closing the chapter we will present the combined diffracted contribution at each microphone position. Previously, diffracted IR were plotted on a logarithmic time axis to illustrate their linearity in logarithmic time, here they are plotted more naturally on a linear time axis. Receiver positions are listed from east to west.

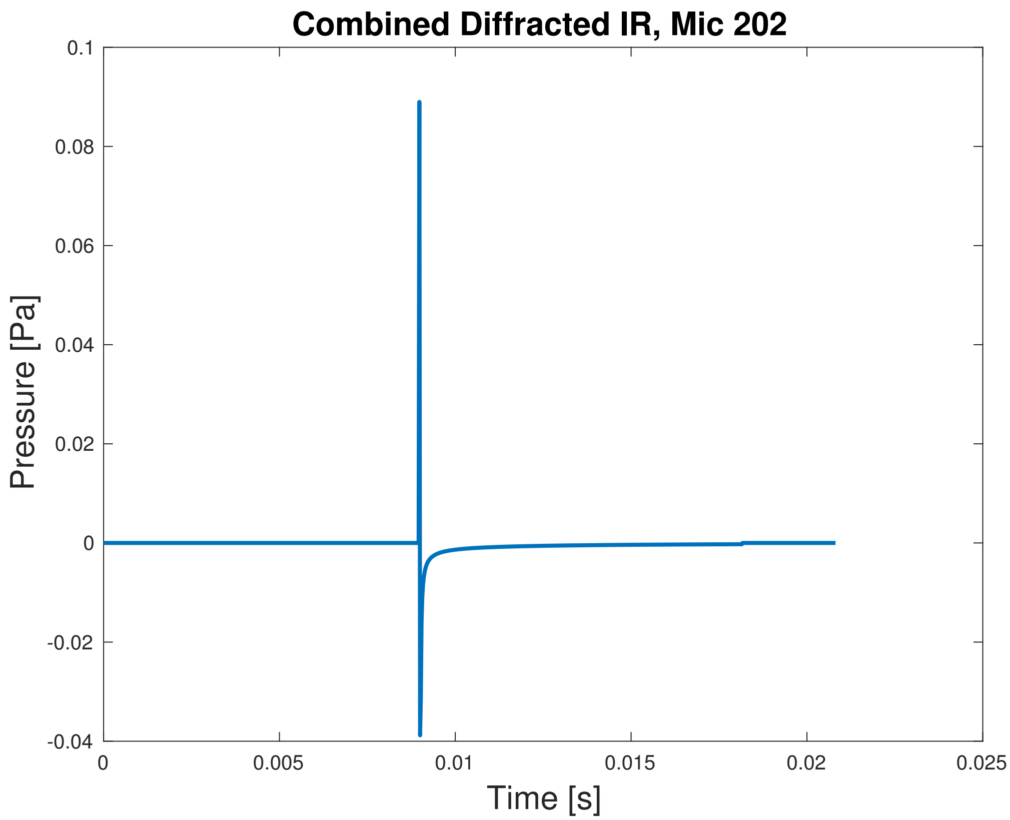

Figure 4.33: Combined Diffracted IR - Mic 202

Performing convolution with our incident waveform yields the following diffracted contributions at each microphone position

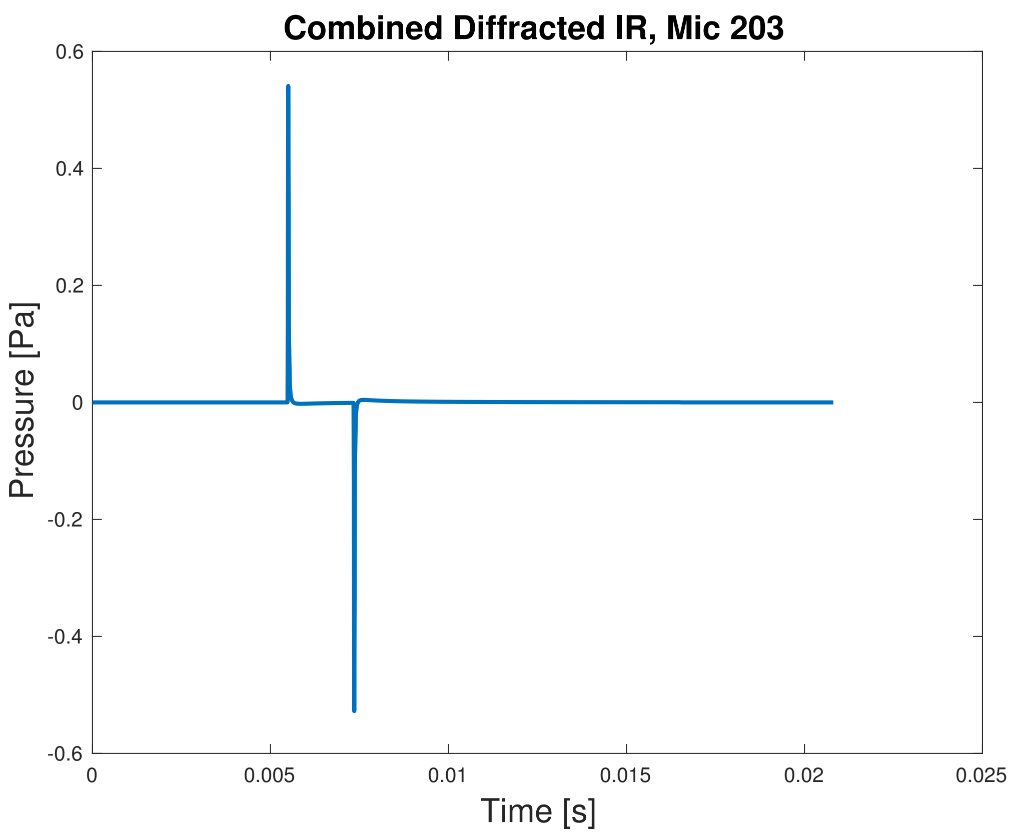

Figure 4.34: Combined Diffracted IR - Mic 203

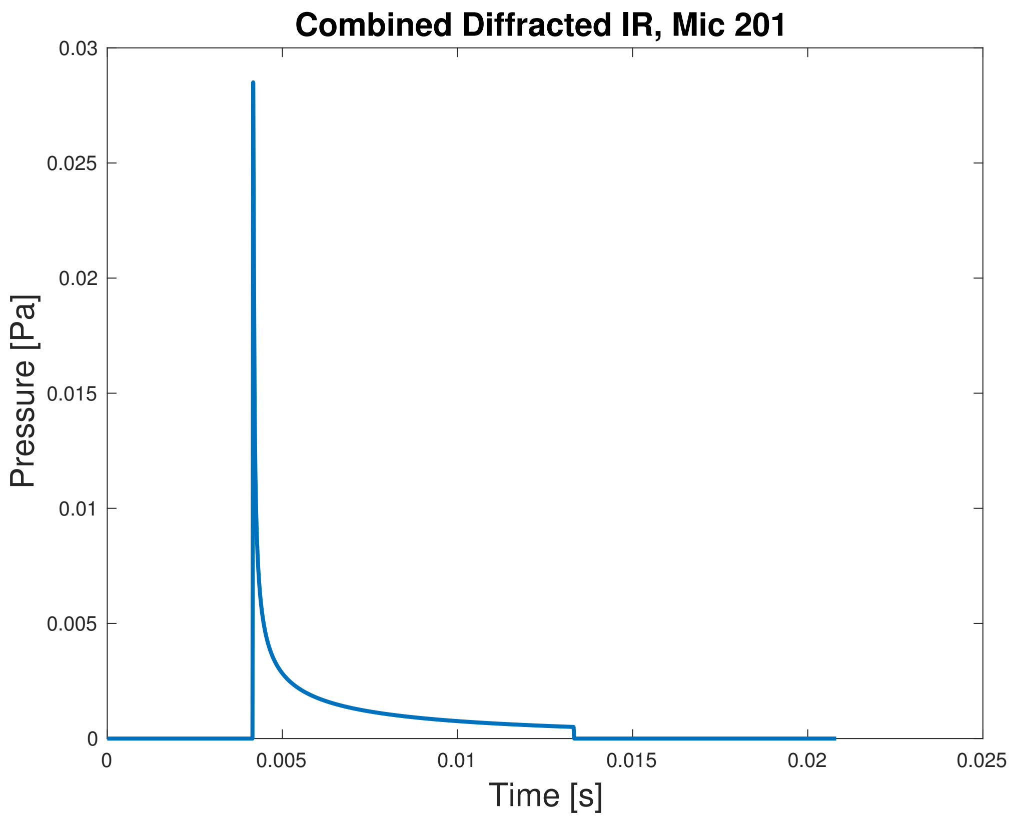

Figure 4.35: Combined Diffracted IR - Mic 201

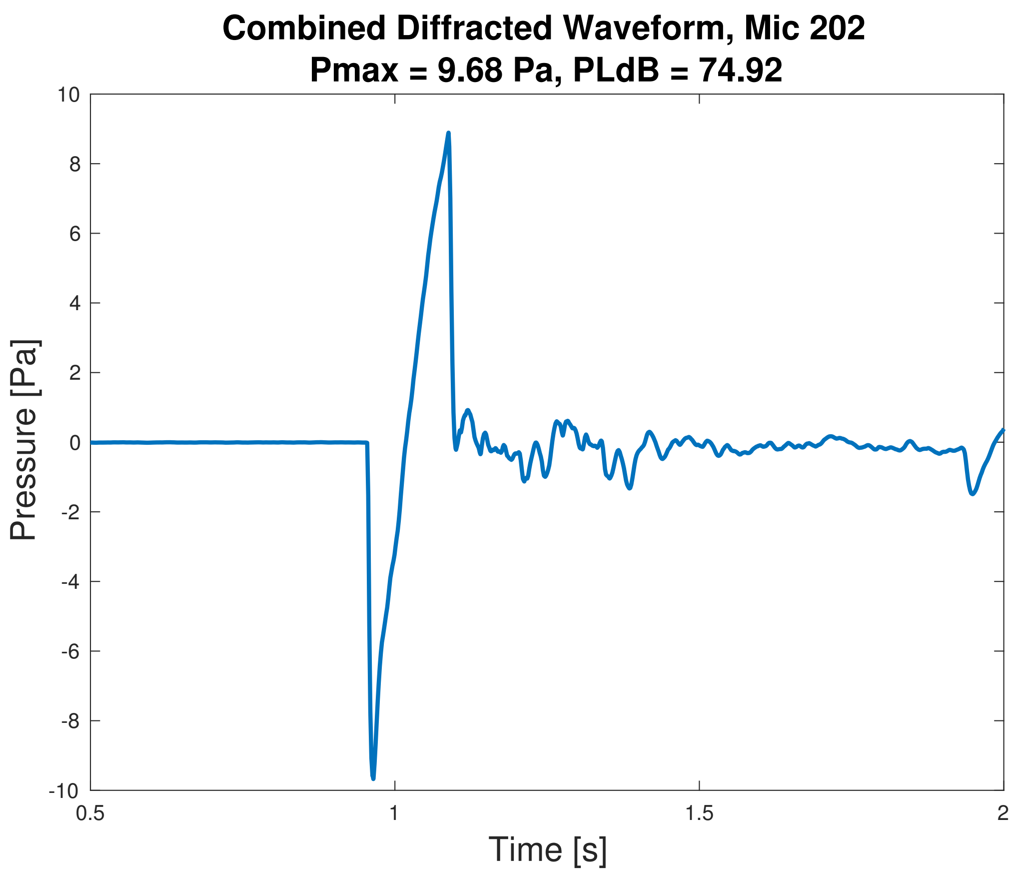

Figure 4.36: Combined Diffracted Waveform - Mic 202

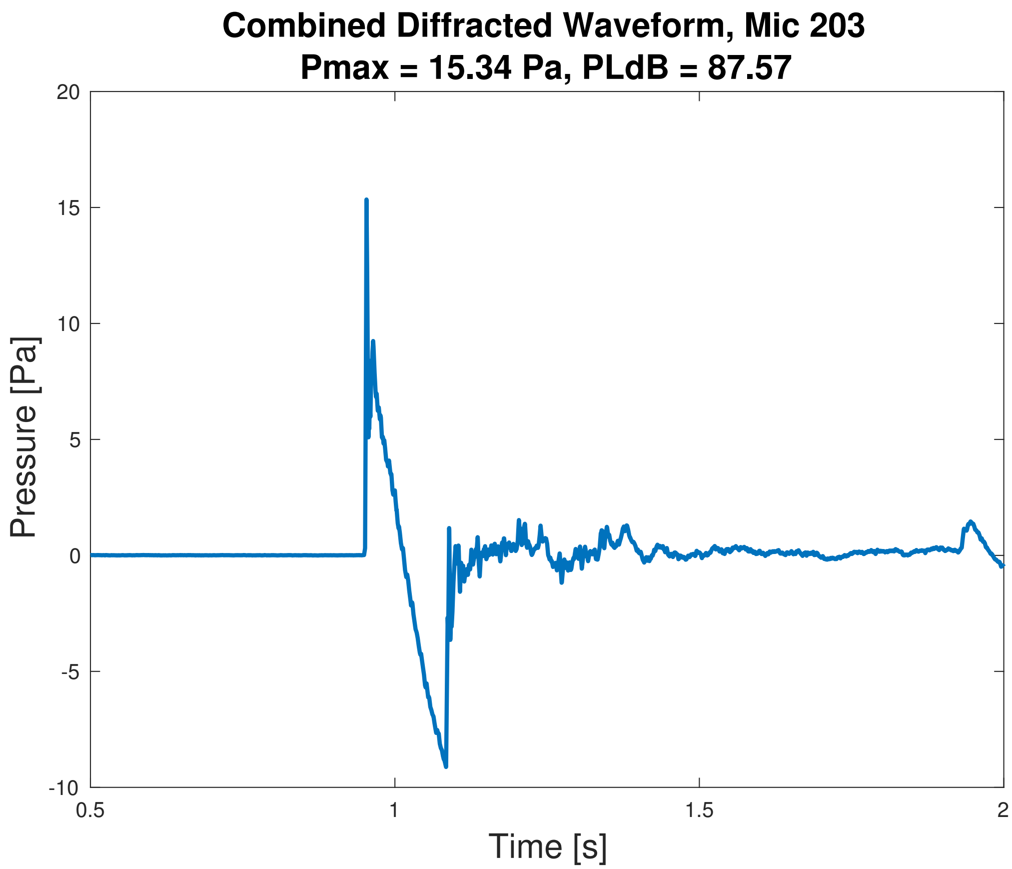

Figure 4.37: Combined Diffracted Waveform - Mic 203

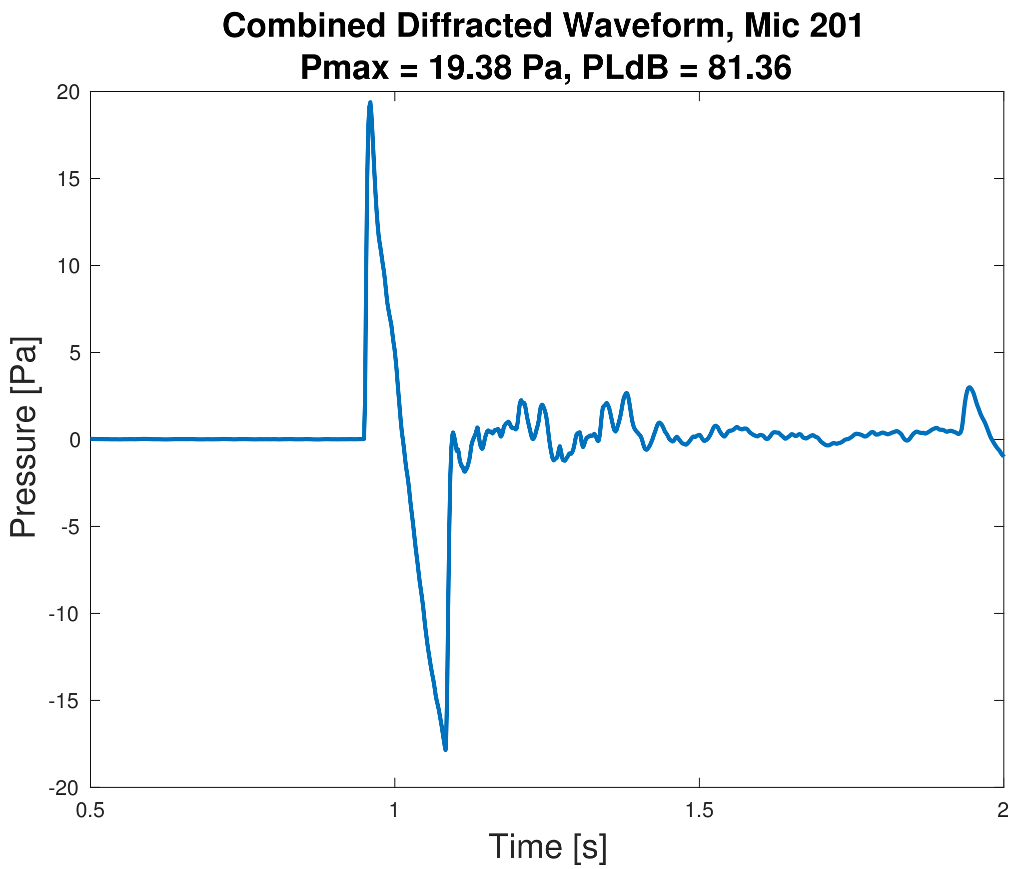

Figure 4.38: Combined Diffracted Waveform - Mic 201

Chapter 5

Field Tests Data

5.1 Introduction

In prior chapters we described the underlying theory and models employed to predict the effects of buildings and terrain on the sonic booms heard around a building. In this chapter, we explore three relevant data sets provided by NASA. Comparisons between the predictions and measurements are made in Chapter 6.

The dataset we will use for comparison is the fruit of flight tests performed on Edwards Airfare Base in June of 2006. The details of this field test were found in the 2007 Technical Report, Vibro-Acoustic Response of Buildings Due to Sonic Boom Exposure : June 2006 Field Test, produced by Jake Klos [46]. This dataset proved to be a good place to begin, since measurements were taken around a simple barrier: a concrete block wall.

A second dataset was also provided around a much more complicated adjacent structure, a highly instrumented multiple family dwelling.

5.2 Scattering and Diffraction by Concrete Wall in Field Test

5.2.1 Context: June 2006 Flight Test

To gain confidence regarding our implementation of BTM, and it's application to the outdoor sonic boom propagation problem, we compare our auralized waveforms to waveforms measured around a simple wall. The data-set analyzed in this Section is a subset of the data acquired during the 2006 test, it is the 'smaller' Matlab data set described on page 102 of [46]. The waveforms presented here were recorded September 22, 2006 at approximately 9:25 AM local time. All booms were conventional, and were generated by straight level flight of an F/A-18B at Mach 1.23 at an altitude of 31,550 ft.

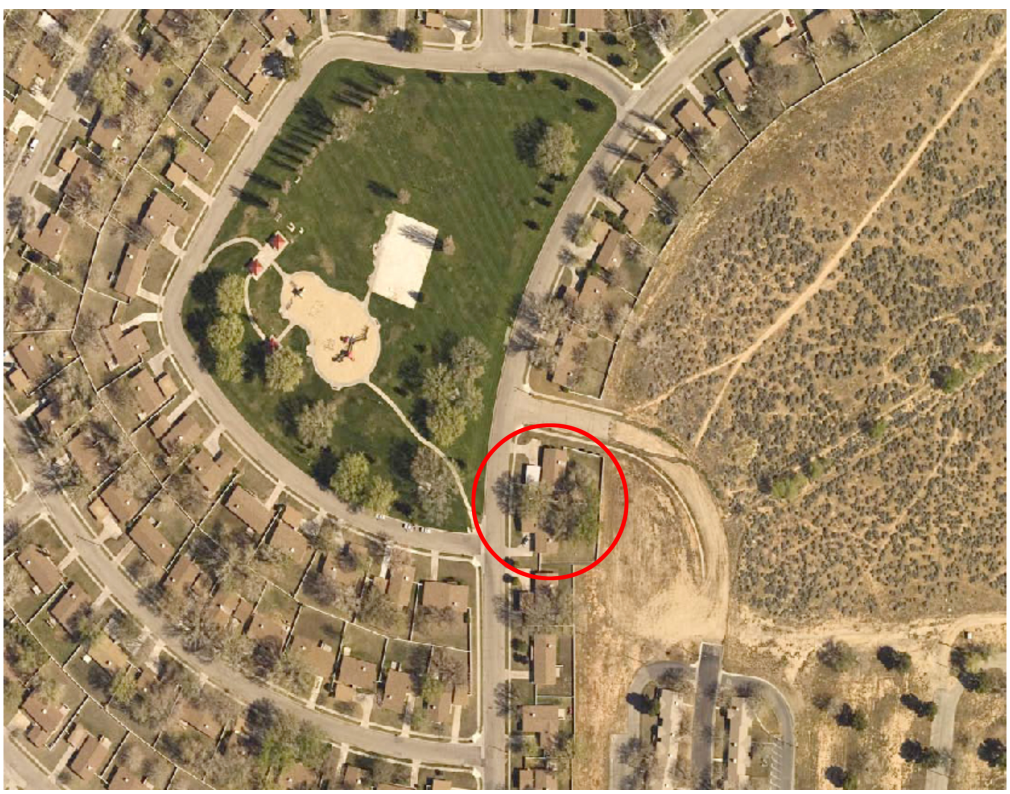

Figure 5.1: Aerial View of Instrumented Site. The instrumented house is indicated by the red circle. The corresponding Latitude and Longitude of are 34.93207 N, -117.940135 E. The address of the home was 7334 Andrews, Edwards AFB.

Table 5.1: Wavefront Arrival Angles

Date	UTC	Az	El	SOS (m/s)	Temp [F]	Boom
2006.06.22	16:31:31	257.193	20.264	348.936	85.505	1
2006.06.22	16:32:25	282.637	18.358	348.935	85.501	2
2006.06.22	16:37:13	255.268	19.352	349.255	86.501	3
2006.06.22	16:38:42	285.942	20.857	349.257	86.508	4

The sonic boom arrival angles given in Table 8.1 were not included in the TM, but were provided via email by Jake Klos. It's notable that in this 2006 test, the convention for reporting incident azimuthal angle varied from that of the subsequent test. The azimuthal and elevation angles here indicate the direction the boom ray paths were traveling **to**, where as subsequent tests report where they were coming **from**, subtract 180° from these azimuthal angles for consistency with the subsequent datasets. Azimuthal angles are measured clockwise from True North. The waveforms analyzed here are recordings of Boom Event 1, this can be confirmed on page 107 of the NASA technical memo [46].

In order to simulate the shadowing and scattering of this boom by the wall, we required the following inputs:

1. incident boom angles from Table 5.1,
2. the dimensions of the wall (shown in Figure 5.2),
3. and the orientation of the wall relative to north.

The TM erroreously states that the corners of the fence are included in the GPS survey data presented in Appendix C of [46], but these coordinates are unavailable. Luckily, aerial photographs were oriented to True North; the wall aligns with Azimuth angle 184°, measured clockwise from North. The aerial photographs present in this document were taken from google maps, however the site has since been leveled, and the satellite imagery has been updated. These geometric relationships were applied in Chapter 3 Section 3.2.1 and Chapter 4 Section 4.4 where we simulated specular and diffracted fields around the wall.

Figure 5.2: Dimensions of the Concrete Block Wall. The cinder blocks "...were roughly 12 inches long by 6 inches high"[46]. The wall was oriented along azimuthal angle of 184°, clockwise from True North.

Table 5.2: Microphone Sensitivities in mV/Pa: Daily microphone sensitivities, after gain, were found on page 54, in Table 3.4 of [46]. A subset of that data, one day of post measurement sensitivities, are reproduced here for convenience. These microphone sensitivities are in mV/Pa and were used to calibrate the boom events - recorded as voltage time-series [V].

Channel	1	2	3	61	62	129	136	177	178	179
Post Cal	48.2	49.1	48.1	48.2	47.2	NAN	NAN	51.3	NAN	61.6
Channel	180	181	182	183	184	185	186	187	188	189
Post Cal	48.5	52	44	45.9	41.6	49	51.2	45.3	49.8	47
Channel	190	191	192	193	194	195	196	197	198	199
Post Cal	58	45.3	46.4	51.7	41	43.2	36.8	42.4	40	39.7
Channel	200	201	202	203	204	205	206	207	287	288
Post Cal	45	42.7	43.5	43.6	42.2	NAN	41.4	41.8	NAN	NAN

It's notable that data from channels 201, 202, 203, 204, 207 were phase reversed, because of the microphone that was used.

5.2.2 Recorded Waveforms

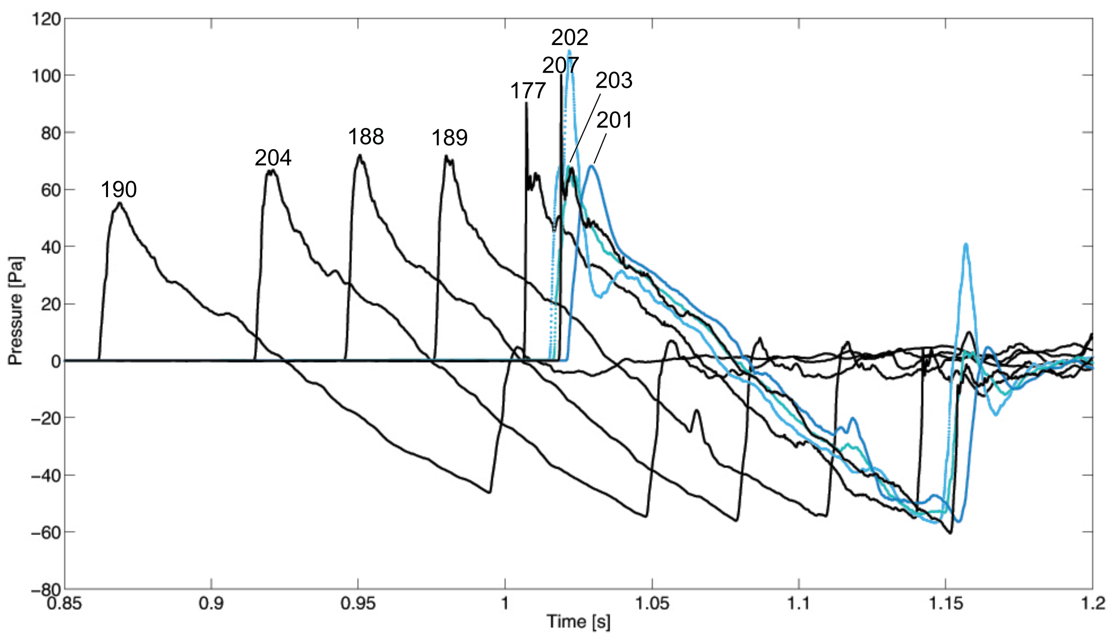

Figure 5.3: Waveforms from the array leading up to the wall. The waveforms measured immediately before the wall, on the wall, and after are indicated in blue.

As shown in Figure 5.3 the wave-front reaches microphones for each channel in the following order: 190, 204, 188, 189, 177, 202, 203, 207, and 201. Here, the arrival of the wave-front is indicated by the pressure exceeding a threshold, for example 10 [Pa], not by the occurrence of peak pressure: the peak pressure in record 202 is due to the arrival of a reflection, not the incident wavefront.

5.2.2.1 Back Scatter From Wall

The length of the sonic boom N-wave is approximately 160 ms. The arrival elevation of the rays of the wavefront approximately 20° from grazing.

Recaling the large planar wavefront, the speed of the wavefront along the ground (phase speed) is faster than the speed of sound. Any wave reflected by the wall would take the same amount of time to get back to the microphone, as the relative delay between the arrival at the microphone, and the arrival at the wall. Any wave diffracted by the wall would spread cylindrically from the top of the wall and will arrive slightly after the specular reflection wavefront. In order to identify the closest microphone with signals only negligibly affected by scattering from the wall, the delays between the incident wavefront and specularly reflected wavefront were calculated, and are shown in Table 5.3.

Table 5.3: Delay in seconds between arrival time at each channel relative to Channel 202, and approximate delay between incident and wall reflected wavefronts.

Channel	190	204	188	189	177
Delay From Mic Arrival to Wall Arrival [s]	0.1534	0.1003	0.0696	0.0392	0.0089
Delay between incident and reflected wavefronts [s]	0.3067	0.2006	0.1391	0.0784	0.0177

For the arrival angles in boom event 1, recordings made at microphones 190, and 204 will not contain interference between the incident and specularly reflected sonic booms due to propagation times and the duration of the N-wave.

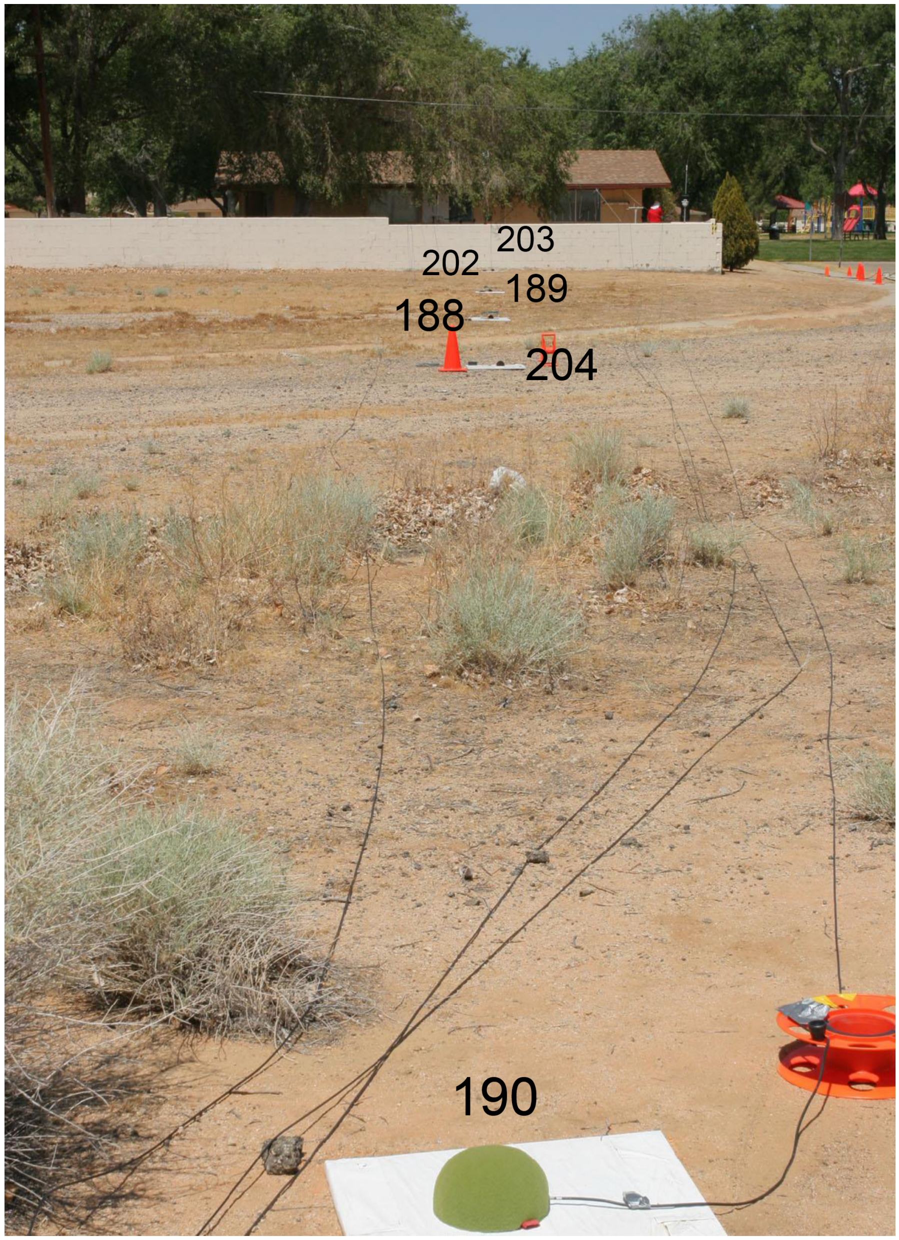

Figure 5.4: Long view of the concrete block wall, annotated with channel numbers. The perspective shown is approximately that of the approaching wavefront. Microphone 190 was a distant microphone and was approximately 81.08 m (266′) from the house. Microphones 189, 188, and 204 were approximately 35.31 m, 47.37 m (115′10″, 155′5″) and, 59.64 m (195′8″) from the back wall of the house, respectively. Channels 202 and 201 were approximately 0.91 m (3′) from the wall on either side. The incident wavefront approaches from the right, and microphones are numbered from right to left in the discussion below

Microphones more distant than 2.51 m (8.25') from the base of the wall are predicted to not receive a specular reflection, due to the elevation angle and wall height. Theory predicts all microphones would capture a cylindrically spreading bad scattered edge diffracted component.x

While interference between the direct and backscattered sonic booms is possible at microphone 188, interference would only occur in the last 20 ms of the waveform. The diffracted contribution would be dominated by low frequency energy, due to the microphones distance from the shadow boundary: the boundary occurs at about 2.51 m (8') from the base of the wall. The backscattered diffracted component at microphone 188 would be attenuated by about 17 dB due to cylindrical spreading and a propagation distance of 47.4 meters.

5.2.2.2 Geometrical Spreading and Consistency

Sonic boom wavefronts may be up to 80.46 [km] (50 miles) in diameter, in such cases, the conic wavefront is accurately approximated by a plane wave at the ground. Is it safe to assume that the wavefront is planar in this experiment? Yes. Without analyzing the flight path and meteorology - was there quantifiable geometrical spreading of the direct sound between microphones 190. 204, 188 and 189? No.

We explore the consistency of the candidate input waveforms two ways:

1. First, by analyzing the peak pressure of the front shock, (which, for all 5 microphones, will be unaffected by the wavefront reflected from the wall),
2. and second, we calculate the PLdB of all five candidate input waveforms to identify the consistency of our perceptual metric, a metric based mostly on the shape of the front shock. See Table 5.4

Figure 5.3, and the peak levels and PLdB metrics in Table 5.4, make it apparent that the waveform at microphone 190, the far field microphone, the waveform varies from those closer to the wall.

Table 5.4: Front Shock Peak Pressure and PLdB

Channel	190	204	188	189	202	203	201
Peak Pressure	55.26	66.78	72.06	71.80	108.59	68.13	68.15
PLdB	95.2	99.0	99.4	100.0	103.4	98.2	96.3

5.2.3 Isolated Wall: Approximation of Incident Waveform

One of the simplest means of approximating the wavefront incident on the wall, is to assume that the pressure waveform incident on the wall is roughly equivalent to the waveform at a microphone far enough away to be unaffected by the scatterer, divided by 2. The division by two is an effort to reverse the pressure doubling due to the ground plane. This introduces some error, as the amplitude of reflection from the ground plane varies with frequency. This approach also assumes that the sonic boom wavefront is perfectly planar, and differences in the waveform due to meteorology and raypath are negligible.

If the recording used to approximate the incident wave is to close to the wall, diffraction from the wall will compromise the results. If the recording used is too far from the wall, variation due to meteorology and ray path will compromise the results. Throughout this document we settle on the waveform captured at microphone 188 scaled by .5 as an acceptable approximation for the incident waveform.

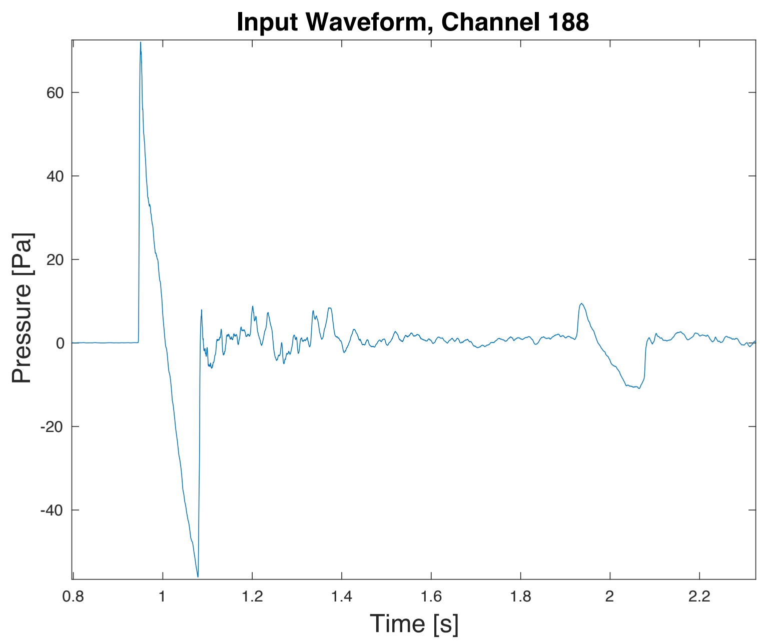

Figure 5.5: This waveform was selected as an appropriate approximation for our incident waveform. This waveform is first divided by 2, this is an approximation for removing ground reflection from recordings with the microphone placed on a ground-board. The waveform is then convolved with the impulse responses simulated in Chapters 4 and 5. The output of the convolution offers an approximation for the pressure at each field point.

5.2.4 Isolated Wall: Measured Scattered IRs

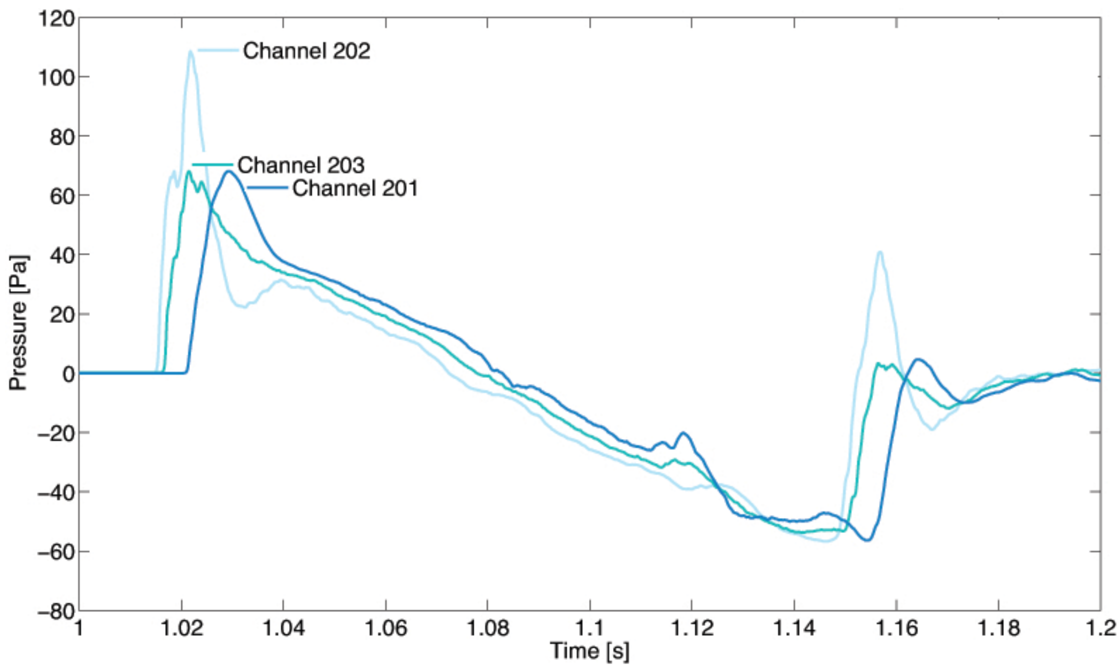

Figure 5.6: The three waveforms measured just before (.91 m East), on top of, and just beyond (.91 m West) the concrete block wall. Recall the boom was incident from the East.

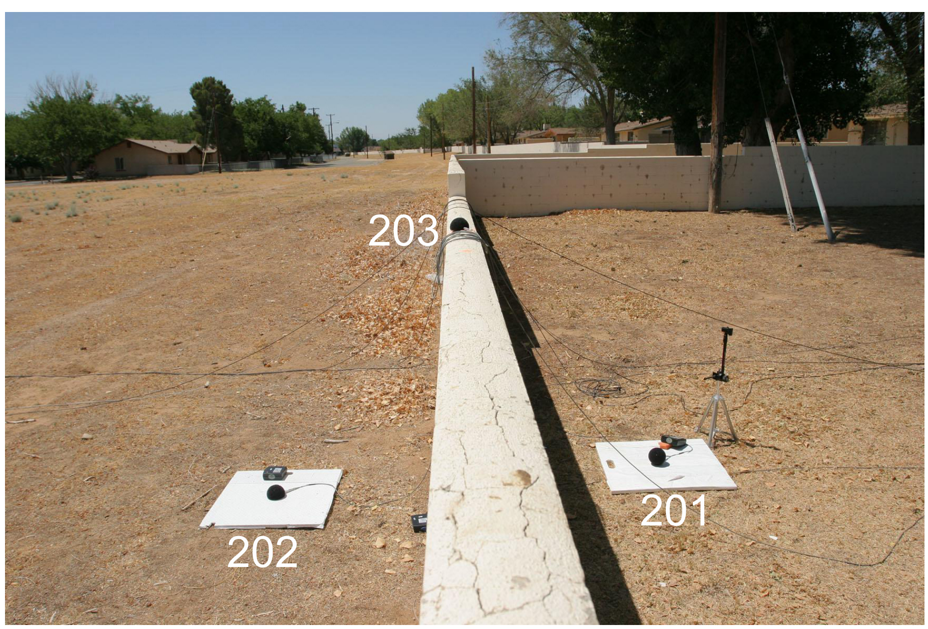

Figure 5.7: Array Over Wall - 202, 203, 201 from left to right.

5.3 Blackbird Field Test

5.3.1 Context: July 2007 Flight Test

In Chapter 3, specular reflections were also calculated around a geometry approximating that of Edwards Airforce base residence instrumented in the 2007 experiment known as HouseVIBES [2].The BTM model was not sufficiently generalized for application to this complicated geometry, but an alternate 'disk approximation' approach for accounting for diffraction was applied. Simulated PLdB contour maps for this geometry were presented in Chapter 3, Section 3.2.3, here we present the corresponding measured field data.

The input incident waveform was approximated by the sonic boom recorded on the desert surface, 300 m West of the structure, scaled by 1/2. This input waveform was then convolved with the impulse response (IR) predicted using the geometry shown in Figure 5.8.

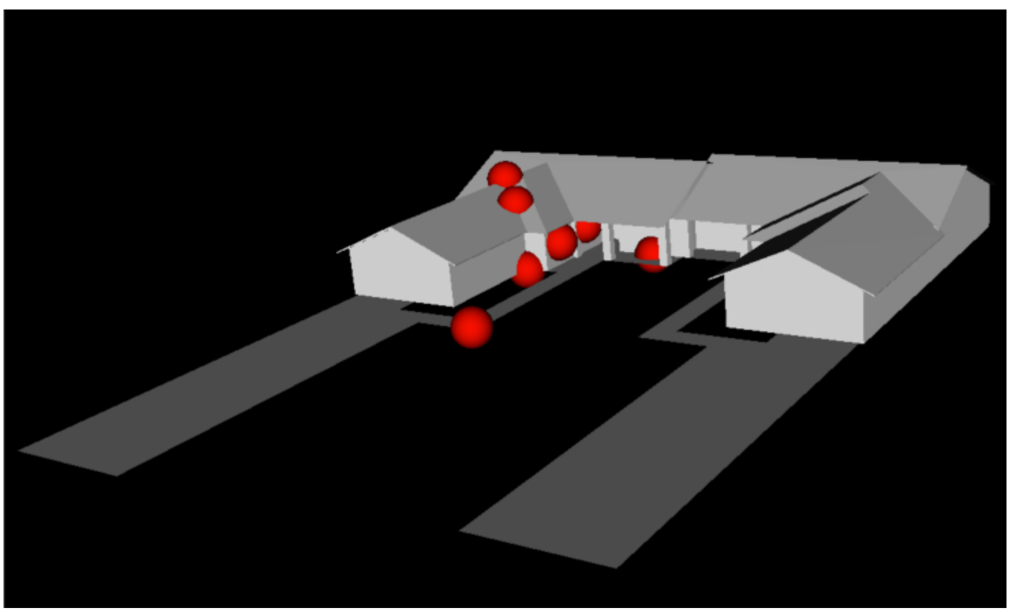

Figure 5.8: Blackbird geometry and microphone locations

Thirty four impulse responses were both simulated and recorded in the experiment, corresponding to the incident arrival angles of the recorded sonic booms comprising the dataset. It was found that the ISM+disk approach significantly under predicted peak pressures, and that the agreement between simulated and recorded waveforms was better without the disk approximation. Without applying the finite disk model, the simulations consistently over predict the peak pressure of the waveform, although by a smaller margin. The BTM approach was not yet sufficiently generalized for application to this complicated geometry.

5.3.2 Measured Building Amplification

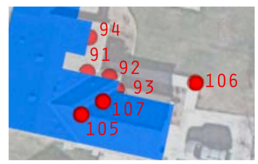

Recorded Building Amplification
(Assuming 300ft West Mic is Accurate Input)
Passes Where Elevation was Negative: 1, 6, 15

Sim, Angles\Mic	91	92	93	94	104	105	106	107
2, Az:62°, El:10°	0.99	0.95	1.15	0.98	1	1.04	1.02	1.00
3, Az:63°, El:5°	2.59	1.88	**3.26**	1.75	1	1.26	1.47	1.46
4, Az:91°, El:29°	2.16	1.51	2.96	1.92	1	1.05	1.34	1.27
5, Az:91°, El:29°	1.56	1.11	1.96	1.40	1	0.81	0.90	0.84
7, Az:58°, El:6°	2.16	1.69	1.75	1.54	1	1.08	1.25	1.28
8, Az:58°, El:10°	2.32	1.67	2.62	1.43	1	1.07	1.21	1.23
9, Az:99°, El:15°	1.93	1.20	1.50	1.62	1	1.07	1.07	1.08
10, Az:103°, El:15°	1.63	1.05	1.35	1.44	1	0.84	0.90	0.87
11, Az:102°, El:18°	1.27	0.79	1.03	1.10	1	0.66	0.72	0.69
12, Az:71°, El:2°	2.30	2.01	2.46	2.02	1	1.47	1.44	1.57
13, Az:68°, El:4°	2.17	1.60	1.76	1.74	1	1.25	1.24	1.34
14, Az:56°, El:1°	1.57	1.17	1.36	1.20	1	0.90	0.90	0.92

Figure 5.9: Building Amplification: The numbers given in this table are the ratio of the peak pressure recorded at each microphone position around the house, to the peak pressure at microphone 104. Microphone 104 was the far field microphone, which was not impacted by the acoustic scattering of the dwelling.

Recorded Building Amplification

(Assuming 300ft West Mic is Accurate Input)

Passes Where Elevation was Negative: 1, 6, 15

Sim, Angles\Mic	91	92	93	94	104	105	106	107
16, Az:89°, El:27°	1.90	1.23	1.57	1.60	1	0.89	1.00	0.97
17, Az:89°, El:30°	2.04	1.36	2.37	1.55	1	0.93	1.07	1.05
18, Az:104°, El:8°	1.79	1.13	1.36	1.55	1	1.11	1.09	1.11
19, Az:107°, El:7°	1.91	1.29	1.82	1.96	1	1.12	1.23	1.12
20, Az:102°, El:1°	1.76	1.07	1.37	1.60	1	0.99	0.96	1.00
21, Az:108°, El:11°	2.12	1.26	1.54	1.86	1	1.29	1.29	1.32
22, Az:76°, El:19°	2.03	1.80	**3.08**	1.80	1	1.06	1.22	1.25
23, Az:77°, El:18°	1.20	0.96	1.43	1.04	1	0.63	0.66	0.74
24, Az:80°, El:17°	2.02	1.33	1.94	1.42	1	0.98	1.09	1.02
25, Az:81°, El:16°	1.52	1.05	1.17	1.27	1	0.74	0.84	0.86
26, Az:112°, El:18°	1.74	1.10	1.42	1.66	1	0.98	1.08	1.00
27, Az:289°, El:19°	1.04	0.84	0.90	0.86	1	1.10	1.01	1.05

Figure 5.10: Building Amplification: The numbers given in this table are the ratio of the peak pressure recorded at each microphone position around the house, to the peak pressure at microphone 104. Microphone 104 was the far field microphone, which was not impacted by the acoustic scattering of the dwelling.

Recorded Building Amplification

(Assuming 300ft West Mic is Accurate Input)

Passes Where Elevation was Negative: 1, 6, 15

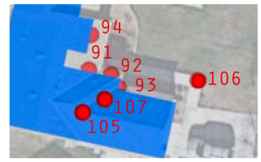

Sim, Angles\Mic	91	92	93	94	104	105	106	107
28, Az:62°, El:1°	1.63	1.43	1.59	1.41	1	1.18	1.12	1.20
29, Az:51°, El:4°	1.97	1.57	1.81	1.42	1	0.99	1.09	1.11
30, Az:95°, El:19°	1.93	1.21	1.64	1.66	1	1.04	1.04	1.03
31, Az:98°, El:15°	1.84	1.20	1.54	1.61	1	0.97	0.99	1.01
32, Az:75°, El:21°	2.23	1.62	**3.32**	1.50	1	1.00	1.02	1.29
33, Az:78°, El:19°	2.63	2.04	**4.80**	2.09	1	1.25	1.10	1.64
34, Az:77°, El:19°	1.87	1.30	2.46	1.54	1	0.80	0.87	0.91
35, Az:74°, El:17°	1.67	1.30	2.65	1.49	1	0.84	0.86	1.14
36, Az:108°, El:14°	1.39	0.98	1.55	1.52	1	0.91	0.92	0.91
37, Az:289°, El:22°	0.47	0.46	0.49	0.48	1	0.53	0.56	0.54
Mean	1.79	1.30	1.88	1.49	1.00	0.99	1.04	1.08
Standard Dev.	0.44	0.34	0.83	0.33	0.00	0.20	0.21	0.23

Figure 5.11: Building Amplification: The numbers given in this table are the ratio of the peak pressure recorded at each microphone position around the house, to the peak pressure at microphone 104. Microphone 104 was the far field microphone, which was not impacted by the acoustic scattering of the dwelling. Also given are the mean and standard deviation of the amplification factors for each microphone position, over all passes.

Chapter 6

Analysis of Measurement Data & Simulation Results

6.1 Review

In Chapter 3, we calculated idealized specular reflections around three geometries

1. an isolated wall,
2. an 'L-shaped' building,
3. and a two family residence that used to reside on Edwards Airforce Base (with the address was 52 Blackbird).

While the 'L-shaped' building was included to verify that the specular reflection code was operating properly, the other two geometries were associated with experimental datasets. Care was taken to best reproduce the wavefront orientation and microphone positions from the documented experimental conditions. This chapter compares the simulated results for the isolated wall to its corresponding measurements.

We attempted to approximate diffraction around the residential geometry (52 Blackbird) using the disk approximation. The disk approximation, described in Section 2.1.2 essentially filters every specular reflection with a high pass filter based on the size of the facet and relative source/receiver locations. This approach consistently underpredicted the peak pressures and PLdB when compared to recorded waveforms. None of the microphone positions from the residential geometry were occluded from the direct sound. The idealized specular field was found to over predict the pressures and PLdB, but by a smaller margin - this is attributed to the fact that all the microphone locations received direct sound. Beyond that summary the disk approximation results were not included in this document, favoring instead the BTM model.

In Chapter 4, we calculated the first order edge diffracted field around the isolated wall geometry (via the BTM Model) at the three microphone positions surrounding the wall. This BTM model is not as mature as the specular model, so higher order diffracted fields, and fields throughout the geometry were not calculated. We briefly discuss the expected margin of error that results from only considering first order diffraction.

For more detail regarding the field test data, see Chapter 5.

In this chapter, we briefly discuss the metrics used to quantify the human impact of sonic booms, and then compare the simulated and experimental results in light of those metrics.

6.2 Quantification of the impact of buildings on the human impact of sonic booms: PLdB

In Chapter 1, It was mentioned that PLdB has been demonstrated to be an an effective metric to quantify the subjective loudness of a variety of outdoor signatures: conventional booms, shaped booms, as well as composite booms (booms consisting of a direct component summed with a single delayed identical reflection) [6].

The Steven's Mark VII PLdB metric applies frequency and level dependent weights to content of the booms in order to better approximate how humans perceive the loudness of these impulsive sounds. As it has been vetted, and is the industry standard for quantifying the annoyance and human impact of sonic booms, PLdB has been the metric employed throughout this section to quantify the perceived loudness of both simulated and measured sonic booms.

The quality of our model is quantified based upon how well it trends with corresponding measured PLdB values.

6.3 Analysis: Isolated Wall Geometry

In this section, we compare the simulated and measured results around the isolated wall geometry. This section references sections 2.1 (analytical solutions), 5.2.2 (Measured), 4.4.2 (Simulated Diffracted), and 3.2.1.6 (Simulated Specular). Please refer to those sections for more detail about how these results were calculated and validated.

Before addressing each individual microphone, let's briefly discuss the strategy employed to combine the specular and diffracted paths. In the following 3 Figures, the original source representing the incident wavefront is shown in blue. The receiver location of interest is on the ground, on the same side of the wall as the incident source.

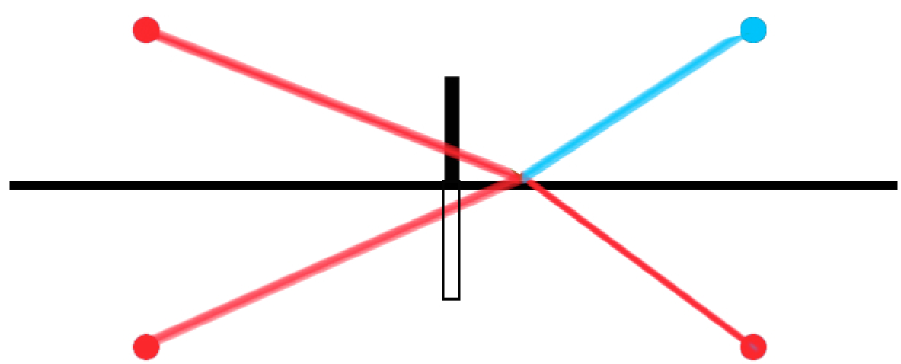

Figure 6.1: Incident (Blue), and Specularly reflected paths (Red)

Next, in Fig. 6.2 and Fig. 6.3, let's consider all paths including 1st order diffraction, and any number of valid specular reflections.

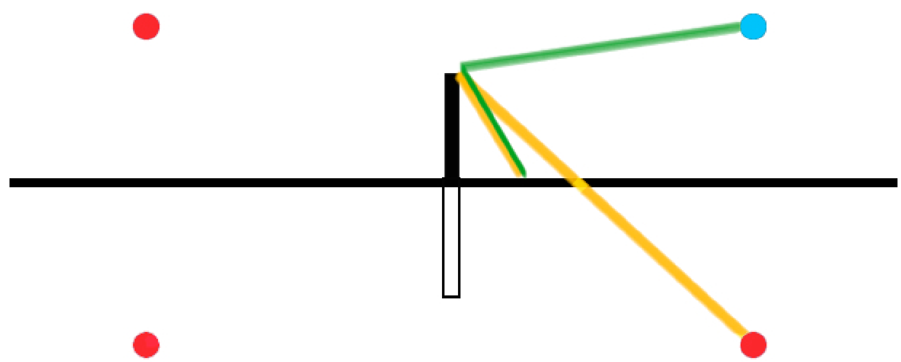

Figure 6.2: Diffracted Path (Green), and Specular->Diffracted Path (Yellow)

Note that the two specularly reflected image sources on the left side of Fig. 6.2 and Fig. 6.3 are ignored. We do not explicitly calculate the diffracted contribution from these sources: The planes that gave rise to these image sources is one of the two planes forming the diffracting edge. The formulation for the edge diffraction solution takes these specular reflections into account. Since the ground plane is not part of the diffracting edge, the image source accounting for ground reflection requires explicit consideration.

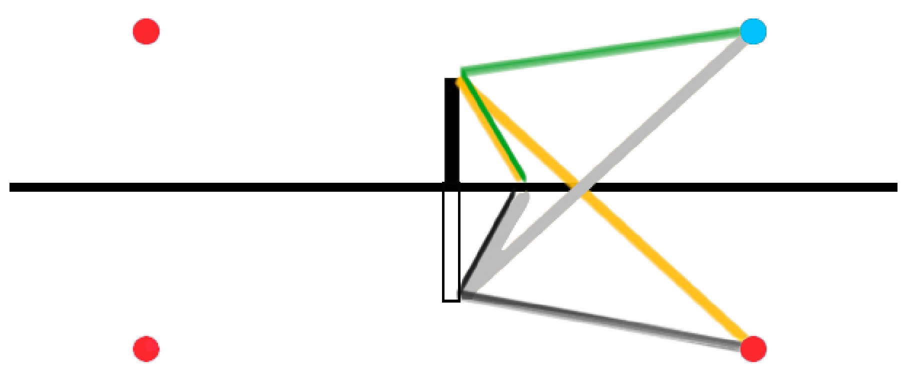

Figure 6.3: Diffracted Path (Green), and Specular->Diffracted Path (Yellow), Diffracted->Specular Path (Light Grey), Specular->Diffracted->Specular Path (Dark Grey)

Figure 6.3 illustrates paths which include a specular reflection **after** edge diffraction, shown in two shades of grey. The lighter shade of grey accounts for the Edge Diffracted->Ground Reflected path. The reflection angles are accounted for by creating an image of the edge (line source) reflected below the ground plane. The darker shade of grey represents the Specular->Diffracted->Ground Reflected Path.

Notice that due to symmetry, either the two grey paths **or** the yellow and green path are the only paths that need explicit calculation. Summing the yellow and green diffracted paths, and then doubling the results, accounts for all paths including 1st order diffraction in this geometry. In section 4.4.2 we calculated only the green diffracted path. In this section, we calculate the diffracted path (green) the specular-diffracted path (yellow) and then double that impulse response to account for subsequent specular reflection of the diffracted path off the ground. This simplification is only possible because our receiver is on the ground. The complete 1st order diffracted IR calculated by this superposition is then combined with the specular IR from Section 3.2.1.6, corresponding to Fig. 6.3.

This development applies to microphones 202 and 201, that is the two microphones on the ground.

Microphone 203 is an outlier, as only the direct path and 1st order diffracted paths from each edge reach the mic centered on top of the wall (the other paths are occluded). The specular reflection from the top of the wall is not occluded and must also be superimposed.

6.4 Approximated Incident Waveform

Before moving on to present the final results, we revisit our approximated incident waveform, for context. This waveform was obtained by dividing the amplitude of the waveform captured at distant microphone 188, by 2 to remove the ground reflection. The waveform captured at microphone 188 can be found in Fig.4.18.

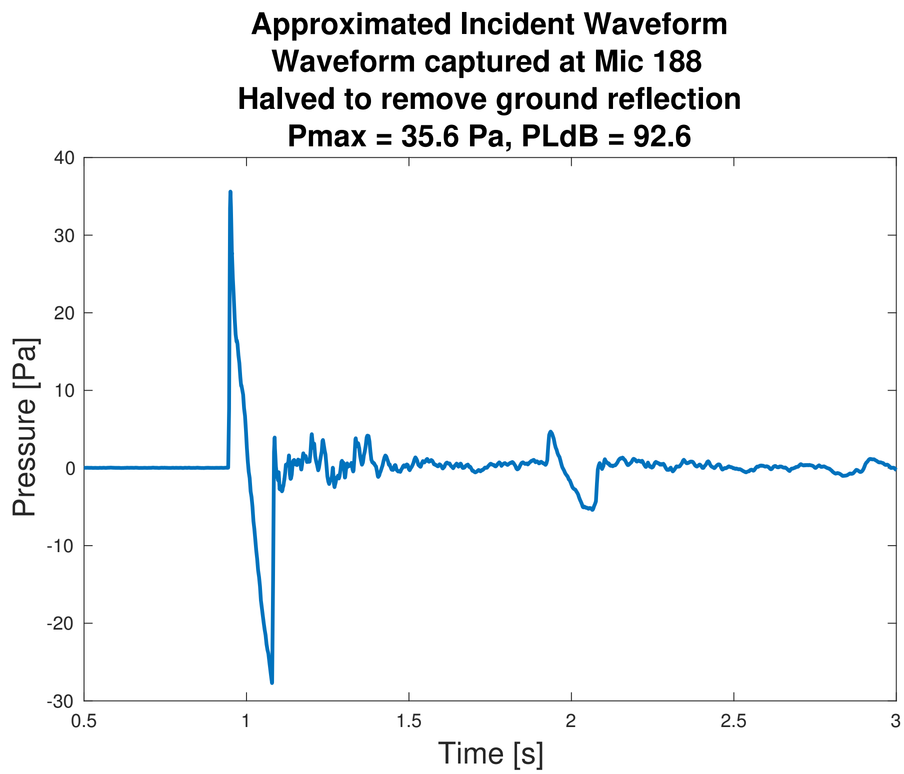

Figure 6.4: Approximated Incident Waveform

6.4.1 Microphone Position 201

As we discussed specular models and diffraction theory, we have hypothesized that the diffracted contributions would be most significant in the shadow zone, and near the shadow boundary. In the shadow zone the incident sound is occluded, and the specular model predicts zero pascals. Near the shadow boundary (relative to wavelength), the diffracted contribution is large, smoothing the transition.

As such, it makes sense that we begin our comparisons with the simulations and recordings in the shadow zone, at microphone 201. These results are the most meaningful, and conveniently simplest to calculate: Since this microphone is in the shadow zone behind the wall, and the specular contribution is zero, the specular and diffracted contributions don't need to be superimposed.

The simulated diffracted waveform, computed by convolving the diffracted impulse response and our approximation of the incident waveform, and originally given in Figure 4.36, is reproduced in Figure 6.5 below.

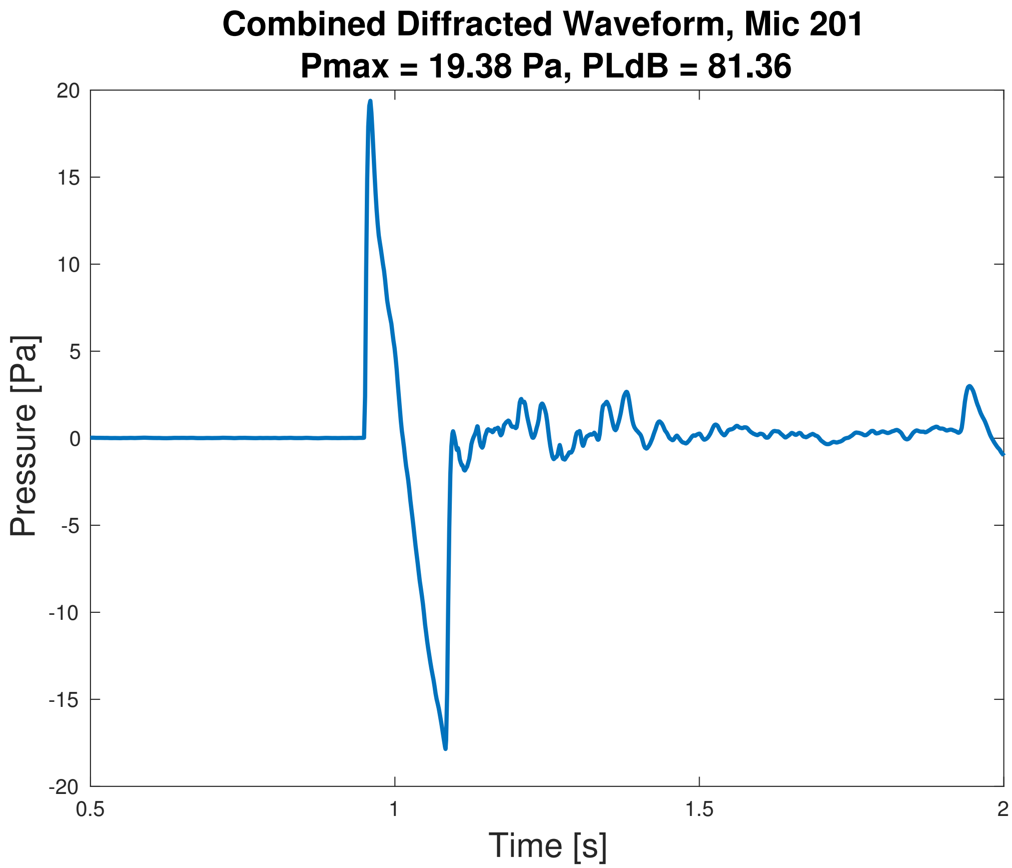

Figure 6.5: Simulated Diffracted Waveform - Mic 201: Diffracted from the western (non-incident) edge of the wall. Pressure doubling due to the ground was included

We compare the simulated waveform in Figure 6.1 with the measured pressure at microphone position 201. Throughout this Chapter, simulated time series will be shown in blue, and recorded time series will be plotted in red. The recorded waveform, which theory predicts should be dominated by diffracted energy, is given in Figure 6.6 below.

While the waveform predicted by our diffraction model, on the occluded side of the wall is much closer to the recorded waveform than silence - the maximum pressure is much lower than expected.

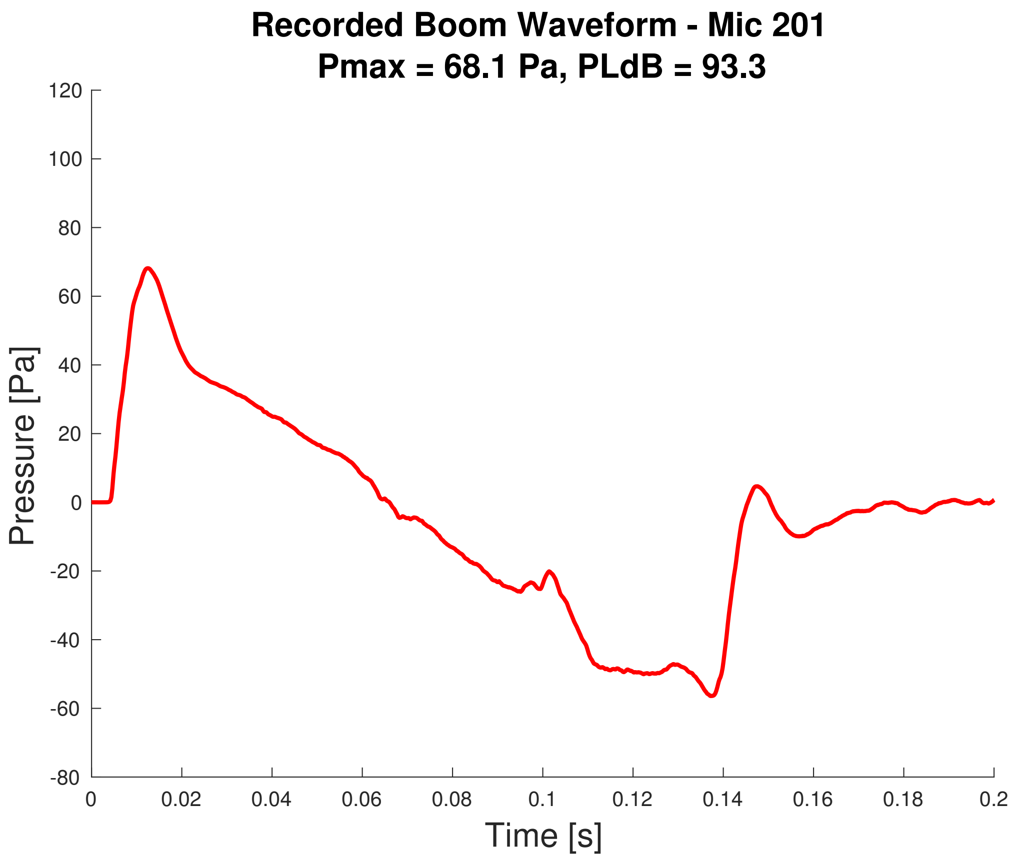

Figure 6.6: Recorded Waveform - Mic 201: Diffracted from the western (non-incident) edge of the wall

6.4.2 Likely Sources of Error

We observe significant discrepancy with regards to overall amplitude and maximum pressure, and PLdB. That said, including this diffracted contribution when modeling the sound field in the occluded area behind the wall would provide a significant improvement over simply simulating specular reflections. Without the diffracted contribution the levels at this microphone position, occluded by the wall, would be predicted to be a PLdB of 0 dB. We underpredict the maximum level by 58.5 Pa, and under predict the PLdB by 18.9 dB. Simplified metric based results like this for all three microphone positions are summarized in Tables 6.1 - 6.3.

If we allow ourselves to trust that this model is perfectly accurate for an idealized isolated wall of infinitesimal thickness, trusting the validation in Chapter 4, the following are potential sources of this discrepancy:

1. A discrepancy between the simulated and measured incident wavefront azimuthal or elevation angles moving our simulated microphone position further from the shadow zone boundary.

2. Low frequency transmission through the CMU wall that we assumed was infinitely rigid. The STC of unfinished hollow CMU block walls is approximately Sound Transmission Class (STC) 45. [48]

3. Scattering from adjacent structures or irregular ground not included in our model.

4. An inaccurate input waveform. If our input waveform is poorly chosen, it's possible that systematic underprediction with this input waveform would correspond to accuracy with another.

5. It was briefly considered that better agreement could be achieved with longer diffracted impulse responses. Our current impulse responses were calculated to be 400 samples long at a 48 kHz sampling rate. This corresponds to 8 ms of propagation time, and about 2.7 meters of propagation distance. Remember, when the diffracting edge is finite, the impulse response is truncated. Given that the incident wavefront hits the broad side of the wall (the incident

angle is nearly normal to the walls axis) our simulations offer the diffracted contribution from a 6 meter wall, centered at the microphone array. The wall is closer to 10 meters in length, centered about the microphone array. Considering that the initial samples of the impulse response are most significant, we discount this potential source of error.

6. Nonlinear vibration of the ground or adjacent structures. These amplitudes are quite high. It's very possible that the environment is contribution to pressures at the microphone beyond our idealized incident, specular and diffracted paths.

7. Non-idealized surface impedances far from infinitely rigid compromise our specular results.

These potential sources for error are present for all following results.

6.4.3 Microphone Position 202

Recall that microphone position 202 is on the eastern side of the isolated wall, on the ground about 0.91 [m] (3') away. The east side of the wall faces the incident shock waves, so this position receives two first order specular reflections and one second order specular reflection from the interactions between the wall and the ground.

The simulated and recorded sonic boom waveforms at microphone position 201 were particularly easy to compare, considering the lack of a specular contribution. To simulate the sonic boom waveform at microphone position 202, we must superimpose the Specular solution from Figure 3.12, with the diffracted contribution from Figure 4.21.

6.4.3.1 Time Aligned Combined Specular and Diffracted IR

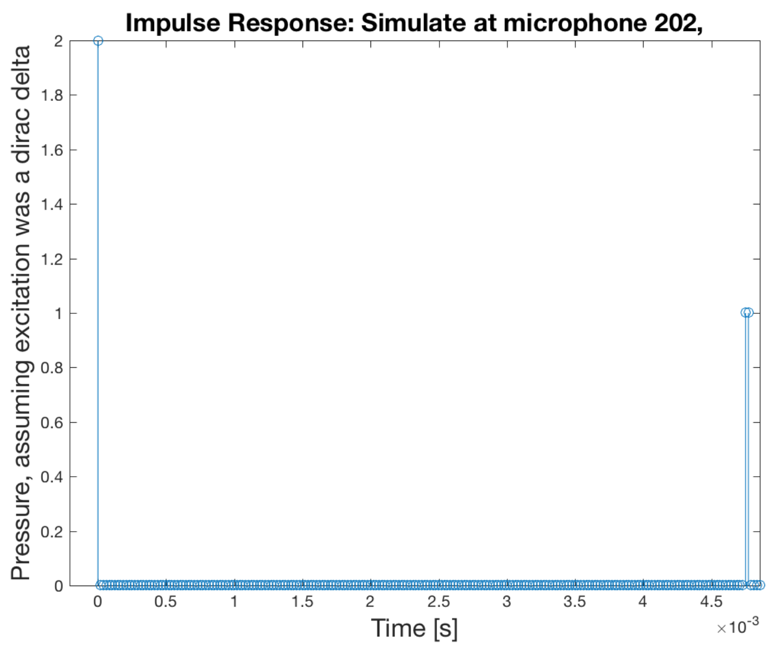

Figure 6.7: This is the impulse response at Microphone 202, the microphone receives a ground reflection co-incident with the direct sound, as shown by the initial impulse with a magnitude of two. Approximately 4.75 ms later, the two second order reflections involving the wall and ground arrive.

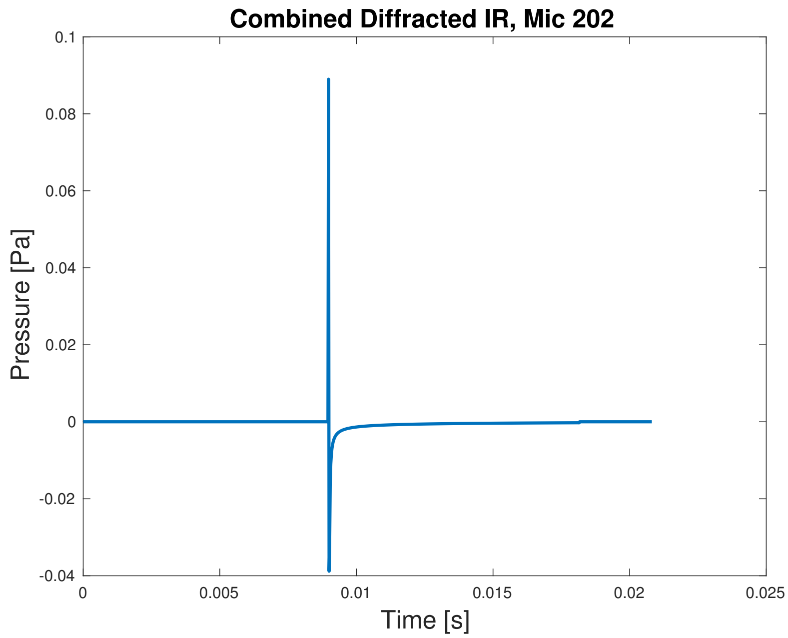

Figure 6.8: Diffracted Impulse Response - Mic 202

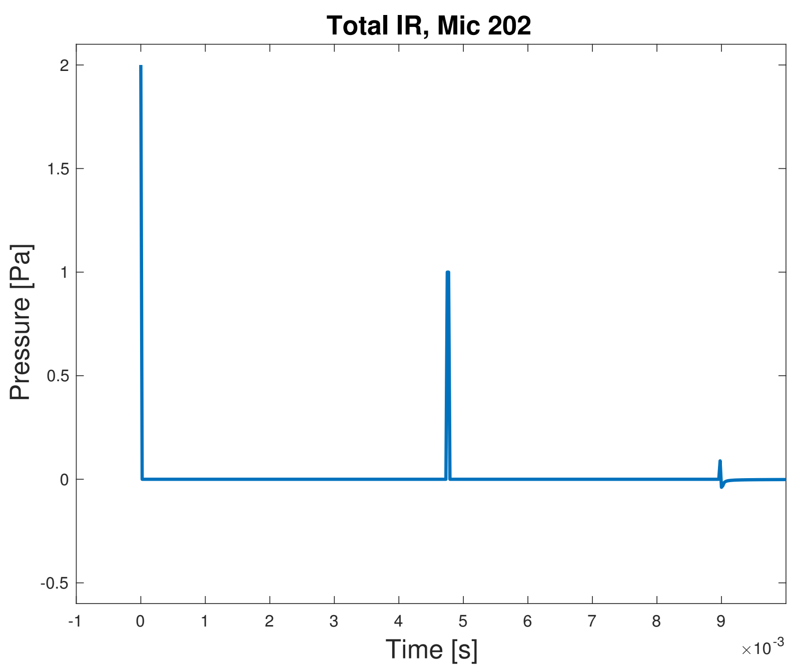

Figure 6.9: Combined Impulse Response - Mic 202. Notice that the impulse response of the diffracted component is negative. It is expected to interact destructively with the specularly reflected wavefront.

6.4.3.2 Time Aligned Combined Specular and Diffracted Waveform

Convolving our combined specular and diffracted impulse response with our input waveform gives the following simulated/auralized sonic boom at the microphone 202 position.

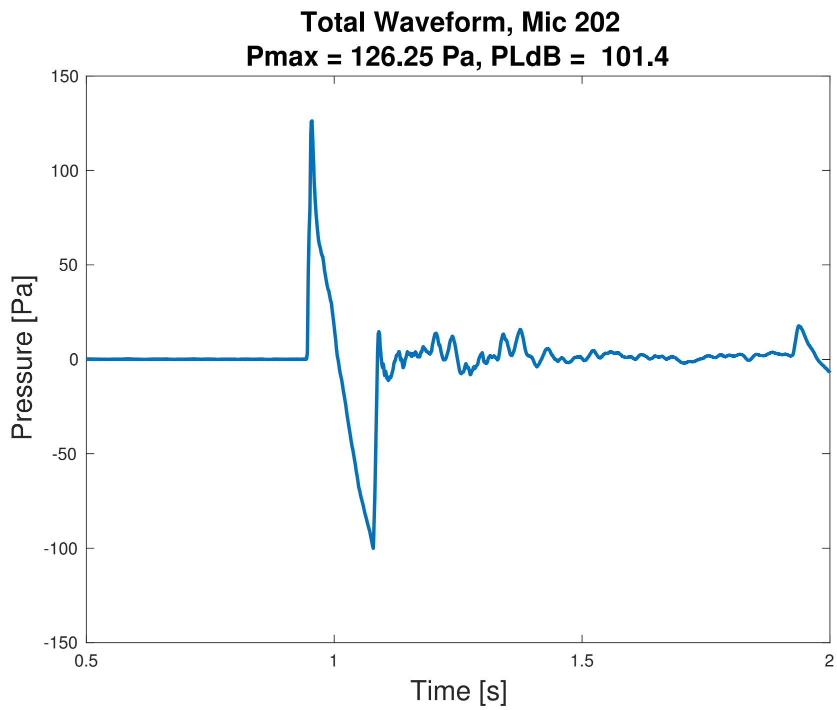

Figure 6.10: Simulated Waveform - Mic 202: Back scattered from the eastern edge of the wall, with both ground and wall reflections. Includes direct, specular and diffracted contributions.

6.4.3.3 Recorded Sonic Boom Waveform

Presented here is the corresponding recorded sonic boom. While the maximum pressure levels are very distinct, the PLdB Levels are somewhat close. The shape of the front shock between the simulated and recorded waveforms is similar. Again Pmax, and PLdB metrics are summarized in Tables 6.1-6.3 at the end of this chapter.

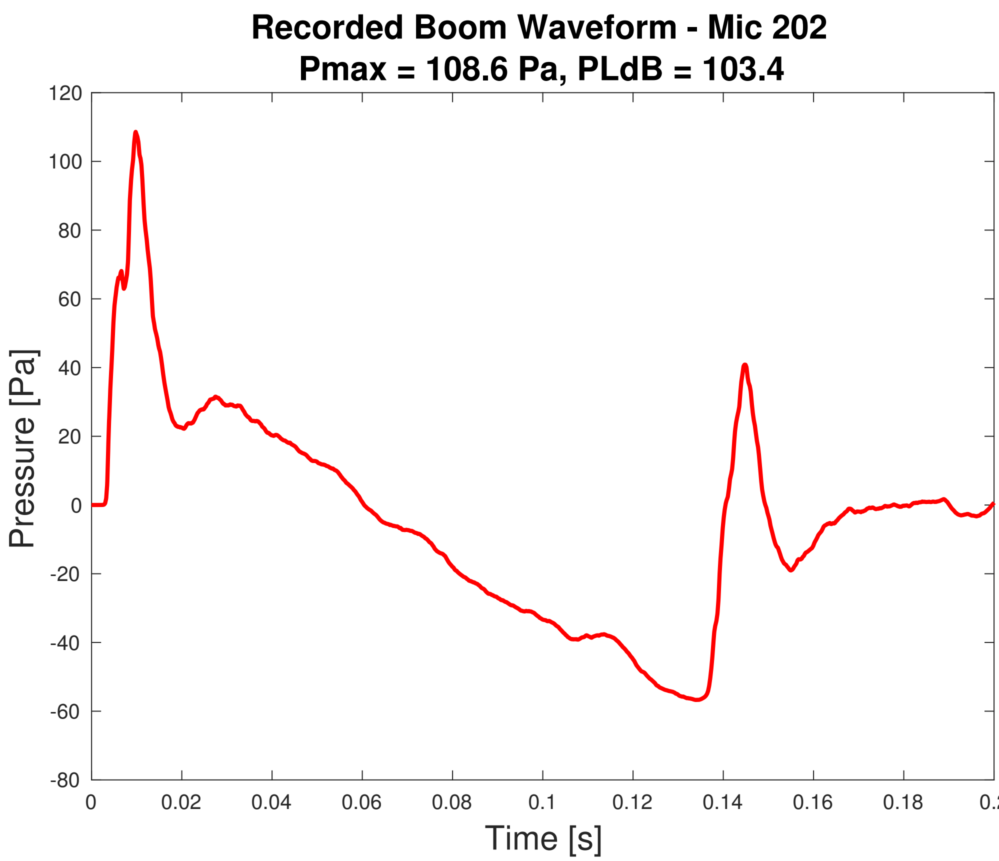

Figure 6.11: Recorded Waveform - Mic 202: Back scattered from the eastern edge of the wall

6.4.4 Microphone Position 203

6.4.4.1 Time Aligned Combined Specular and Diffracted IR

Simulations at this microphone position are outliers for a couple reasons. CMU are about .20 [m] (8") wide, so the microphone is only .10 [m] (4") from two different diffracting edges. Given this very short distance to the edge, and the near normal incidence of the shockwave to the wall, all the diffracted energy arrives quickly. The typical exponential decay with time does not have an opportunity to set up. As such the impulse response and predicted boom waveform are distinct from those simulated at microphones 201 and 203.

Lastly, and perhaps most significantly, here we have only modeled the first order diffracted contribution from one edge. Contributions from both edges framing microphone 203 are certainly significant and interfere.

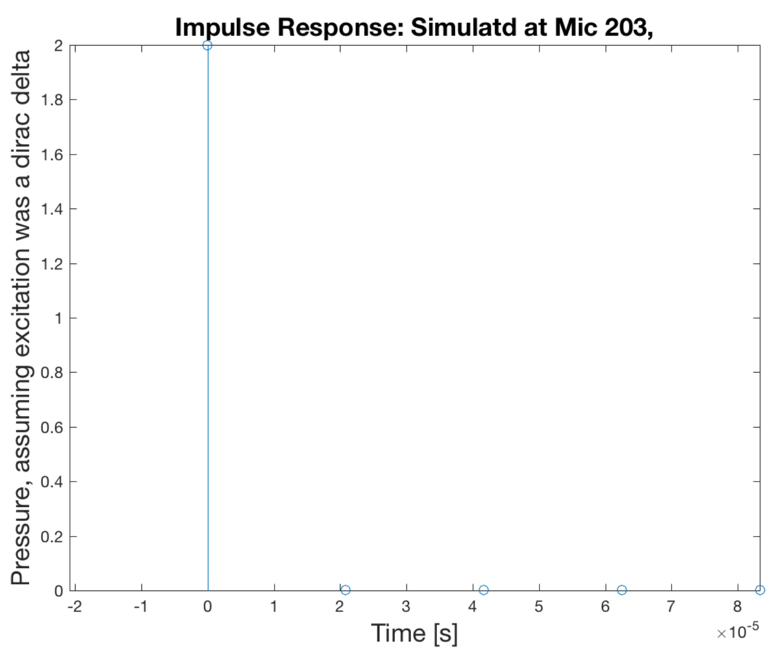

Figure 6.12: This is the impulse response for microphone 203, the microphone on top of the wall. It receives only the direct and 'ground' reflected contributions. In this case 'ground' refers to the surface on top of the wall. This is expressed as the initial sample with value 2, as though two coincident dirac deltas had been summed.

As mentioned, because of the geometry relating the edge to the incident wavefront, and the proximity between the microphone and the edge, the typical edge diffracted behavior does not have an opportunity to establish itself. If we were to simulate a longer diffracted impulse response, as though the wall were infinite, we would see the exponential decay (linear in log space) that we've become accustomed to.

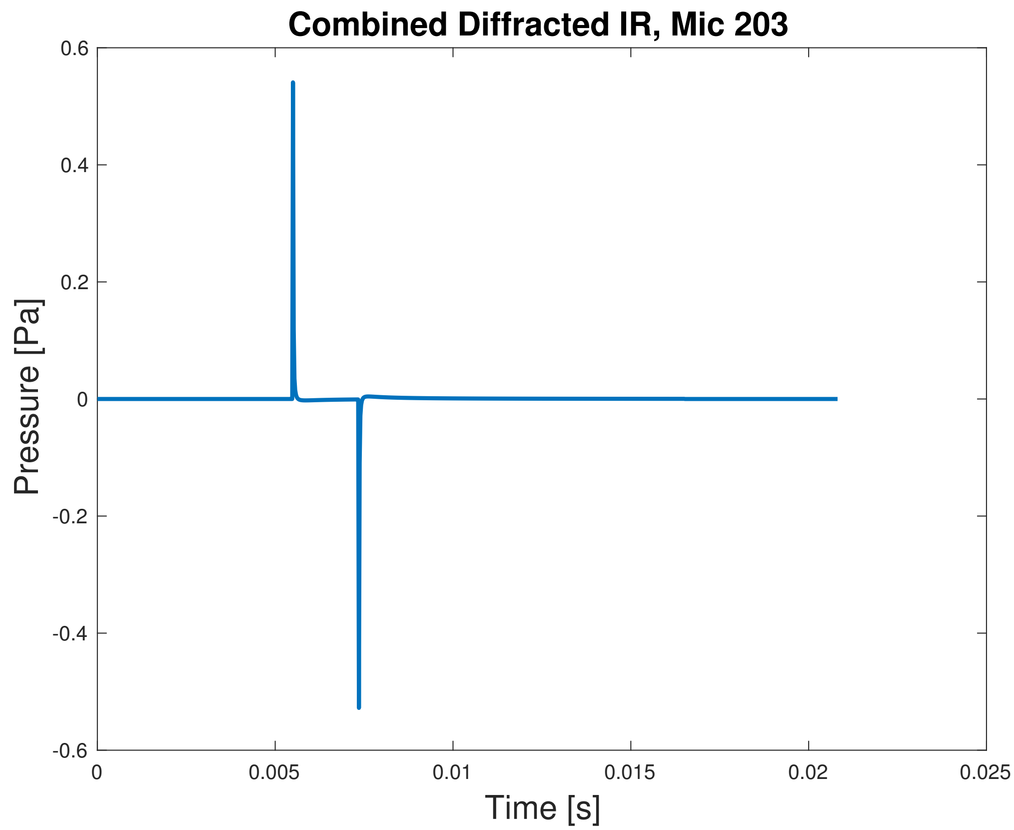

Figure 6.13: Diffracted Impulse Response - Mic 203

Let's briefly be reminded that we have currently modeled all reflective surfaces as infinitly rigid. This assumption is not only present in the edge diffraction calculation, but also in the magnitude of our specular reflections.

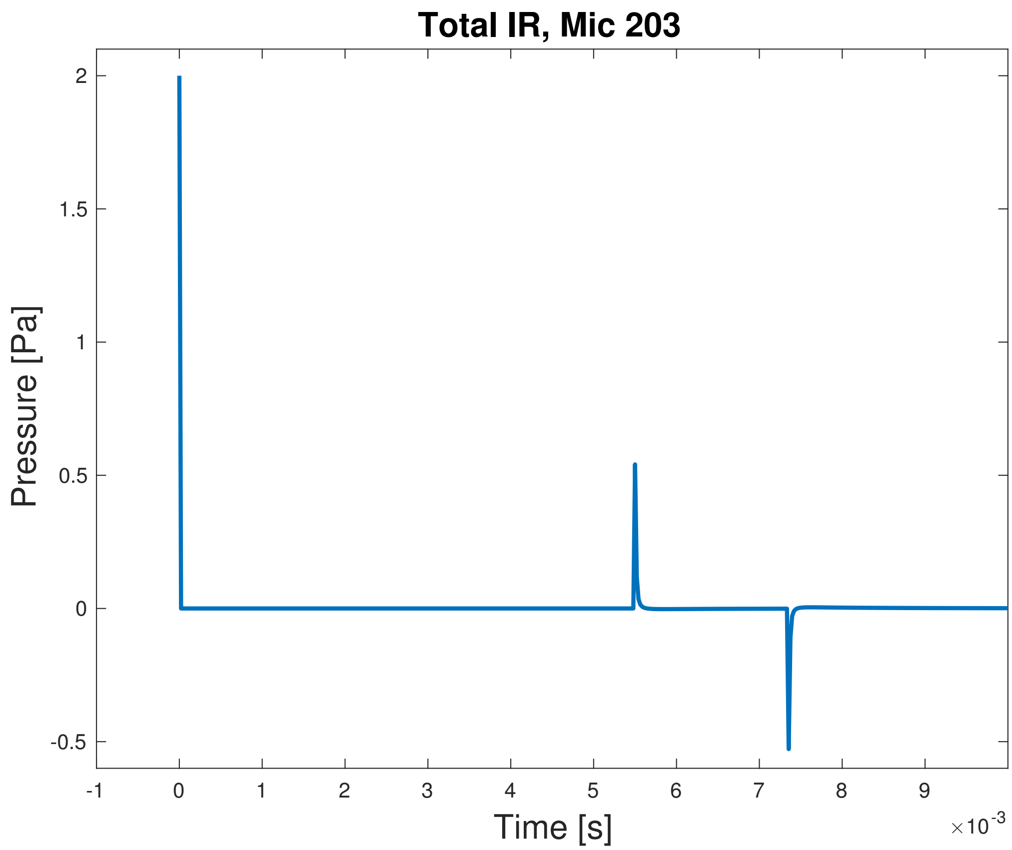

Figure 6.14: Combined Impulse Response - Mic 203

6.4.4.2 Simulated Sonic Boom Waveform

This simulation is our least confident simulation. Among the causes of error present in the other cases, this microphone receives **two** first order diffracted contributions. The other microphone positions only possess one first order diffracted contribution, and one second order diffracted contribution from the wall. Here we present results including only the contribution from one side of the wall. It's very likely that the contributions from both sides would interact significantly.

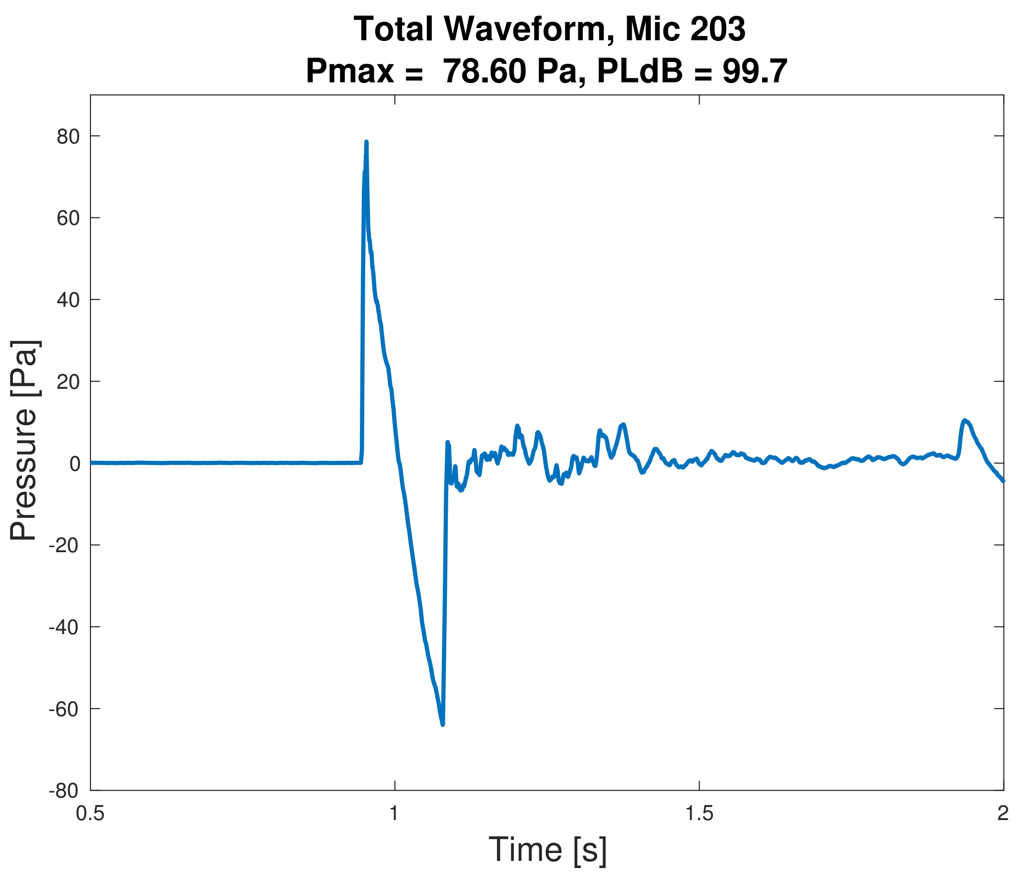

Figure 6.15: Simulated Waveform - Mic 203:Forward scattered from the eastern edge of the wall to the top of the wall, Including direct, specular and diffracted contributions

6.4.4.3 Recorded Sonic Boom Waveform

While the diffracted contribution on it's own looked very distinct from all other simulated or measured waveforms, the diffracted contribution is dominated by the specular contributions, and the combined simulated waveform resembles the measured waveform in shape.

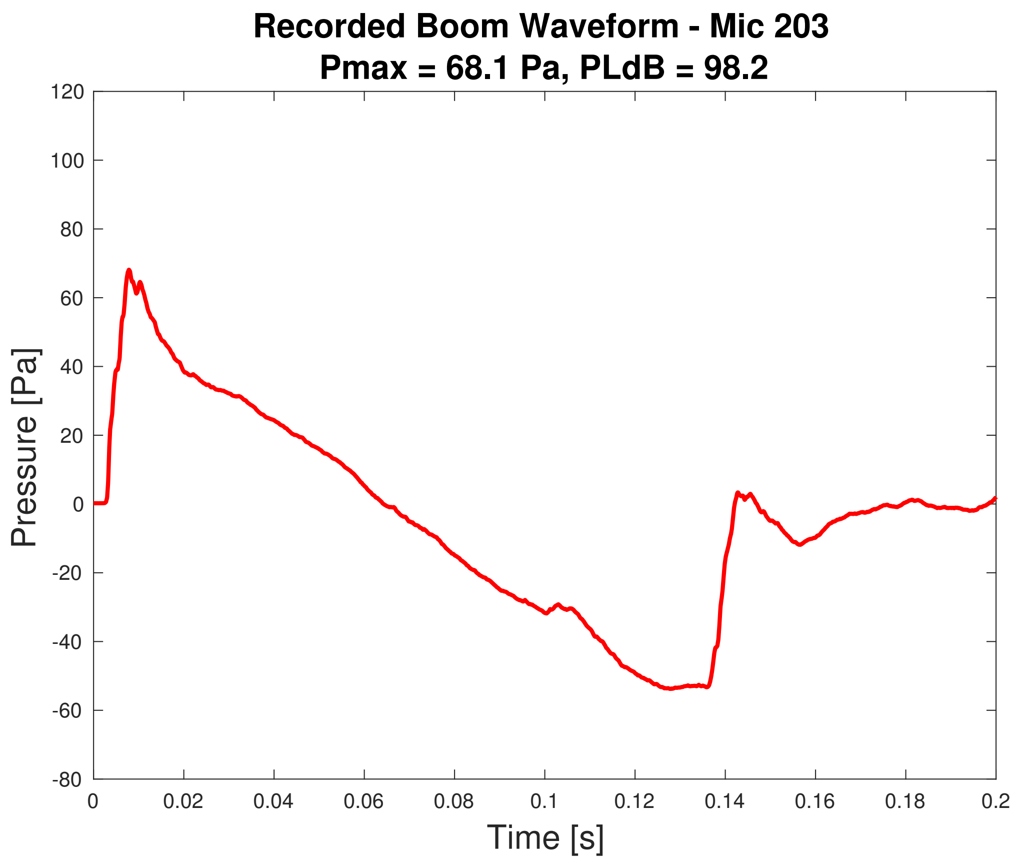

Figure 6.16: Recorded Waveform - Mic 203:Forward scattered from the eastern edge of the wall to the top of the wall

6.5 Tabulated Isolated Wall Results

Recall that the sonic boom wavefront was incident from East to West, and that the microphones surrounding the wall are oriented in the following order, from East to West: 202, 203, 201.

In the following tables we compare metrics obtained from the recorded, and simulated sonic booms. It compares the measured results, with simulated results using only the specular component, only the diffracted component, and the combined results.

Metrics selected were maximum (peak) pressure, and PLdB.

6.5.1 Tabulated Isolated Wall Results: Specular results and 1st order Diffraction at Microphone 201

Microphone 201 is the western most microphone, the incident wavefront is occluded at this microphone. As such, we would expect this microphone to be the most interesting with regards to assessing the diffracted contribution.

Table 6.1: Tabulated Results Mic: 201

	Pmax [Pa]	PLdB [dB]	Pmax Error	PLdB Error	Pmax % Error
Recorded	68.1	93.3			
Specular	0	0	-68.1	-93.3	100%
Diffracted	19.4	81.4	-48.7	-11.9	-71.5%
Combined	19.4	81.4	-48.7	-11.9	-71.5%

We see that including the first order diffracted contribution greatly improves agreement over simply considering the specular field, which predicts silence. That said, we under predict the PLdB value by about 12dB.

6.5.2 Tabulated Isolated Wall Results: Specular results and 1st order Diffraction at Microphone 202

Recall that microphone 202 is on the ground, on the side of the wall facing the incident wavefront.

Table 6.2: Tabulated Results Mic: 202

	Pmax [Pa]	PLdB [dB]	Pmax Error	PLdB Error	Pmax % Error
Recorded	108.6	103.4			
Specular	126.5	101.0	+16.8	-2.4	+15.8%
Diffracted	9.67	74.9	-98.9	-28.5	-91.1%
Combined	126.3	101.4	+16.6	-2	+13.1%

In the case of microphone 202, the specular solution alone achieves the good agreement. Agreement is marginally better when the diffracted contribution is included.

6.5.3 Tabulated Isolated Wall Results: Specular results and 1st order Diffraction at Microphone 203

Recall that Microphone 203 is on top of the wall.

Table 6.3: Tabulated Results Mic: 203

	Pmax [Pa]	PLdB [dB]	Pmax Error	PLdB Error	Pmax % Error
Recorded	68.1	98.2			
Specular	71.2	99.3	3.1	1.1	4.6%
Diffracted	15.34	87.5	-52.8	-10.7	-77.5%
Combined	78.6	99.7	10.5	1.5	15.4%

As in the case of microphone 202, best agreement at this location is achieved by accounting for only the specular contributions.

As such, the results indicate that first order diffracted contributions should be considered when direct and specular paths are occluded, but can safely be omitted, or are insufficient, when direct and specular fields are present.

For the required computation time for these simulations, see Section 8.5.

Chapter 7

Conclusion

In order to increase the fidelity and perceived realism of synthesized sonic booms, a model superimposing direct sound, specular reflections and diffracted contributions was implemented. The impact of specular reflections and diffracted contributions on human impact of sonic booms was quantified with the industry standard PLdB metric. Specular fields were simulated in meshes at listener height and ground level, allowing for the generation of contour plots of maximum pressure and perceived level. These contour plots inform us as to where maximum pressure and perceived level were most amplified by the listening environment.

It's notable that Pmax and PLdB do not map to each other proportionally, recall the rise time of the shock wave controls PLdB, not the peak amplitude.

7.1 Specular Results

In Chapter 2, simple specular reflection simulations were presented which illustrated the relationship between listening environment and sonic boom waveform. Using this waveform, the human impact of the sonic boom was quantified by calculating the 'Perceived Level' Metric, PLdB. Since PLdB is highly dependent upon the rise time of the sonic boom waveform, doubling the waveform does not result in an increase of PLdB by 6 dB. When the space is bisected by a boundary, there is pressure doubling due to reflection, however the change in PLdB is more on the order of +3 PLdB. Idealized specular simulations illustrated that when free space is bisected by the building/terrain geometry three times (resulting in a 1/8th space corner), the change in PLdB is on the order of +9 to +14 PLdB. These circumstances of greatest predicted increase in PLdB occurred in simulations of corners composed of exterior corners with 90 degree angles, if the angles are acute, more image sources would be coincident at the receiver and a larger PLdB than those simulated would result.

Higher order specular reflections were calculated at 3 microphone positions around an isolated wall, and in contours around an 'L-shaped' structure, and multi-family residence. In comparing field test data with our specular simulations, PLdB predictions around the isolated showed excellent agreement. The PLdB levels predicted around the isolated wall by our approach were within 12 PLdB in receiver positions without occluded direct paths. It's quite impressive that the simple model achieved such good agreement, despite idealized surface impedance models.

In the case of occluded listener positions, our specular model is woefully insufficient, as expected. In occluded areas, specular, geometric acoustic, and ray based models under-predict PLdB by 93 dB.

More analysis is desired to validate the specular model for all the microphone positions around the residential structure to the corresponding measured data. The contour plots reflecting hotspots of maximum pressure and PLdB are in line with specular theory and intuition. The excellent agreement for the isolated wall specular simulations are encouraging: the specular contour plot tool is likely capable of good agreement for more complicated geometries.

7.2 Diffracted Results

First order diffracted results were presented at three microphone locations around an isolated wall. First order results for the entire geometry could one day be calculated - pending the programming of visibility checks of all edges at each microphone location. Higher order diffraction or specular-diffracted combination paths would require significant effort: it would require decomposing each analytically calculated diffracted solution into contributions from many point sources distributed in a line along the edge - each contributing a single sample at the listener position. Luckily, for the simple isolated wall geometry, first order diffraction offers significant improvement for characterizing the diffracted field in the shadow zone.

We simulated and confirmed our edge diffraction model against published figures with success. Theory and intuition predicted that diffracted contributions destructively interfere with impulse responses on the en-sonified side of the shadow boundary, and constructively interfere with impulse responses calculated on the occluded side of the shadow boundary - essentially smoothing out the transition from unmitigated propagation and occlusion.

Unfortunately, except for microphone position 201, which was in the shadow zone and receives no specular reflections, including the diffracted contribution did not significantly improve agreement with measurement for both microphone locations 202 and 203. The specular simulation alone had better agreement at microphone position 203. Only a slight improvement in agreement was achieved by including the diffracted contribution at microphone position 202. Calculating the diffracted field greatly improved agreement in the shadow zone.

Calculating the diffracted field is recommended for geometries with occluded listener positions.

7.3 Confounding Phenomena & Mitigation

The agreement between simulated and measured results depends highly on the accuracy of the incident angles. Considering the fact that the diffracted field significantly varies based on the receiver position's proximity to the shadow boundary, a few degrees of error in the incident elevation angle will introduce a lot of error and render the simulation unrepresentative. Often a distant tower was used to discern the elevation angle of the incident sonic booms, and refraction between the tower and the microphone positions was not accounted for.

A second confounding phenomena, in the isolated wall case, is transmission through the wall. Our simulations assumed idealized rigid boundaries - theoretically the first order diffracted solution should describe the pressure field in the occluded areas behind the wall. As mentioned in Chapter 6, the STC of unfinished hollow CMU block walls is approximately STC 45 - quite distinct from infinitely rigid.

That said, PLdB, and perceived loudness depends highly on the rise time of the sonic boom, and fast rise times require high frequency content. As expected with massive boundaries like CMU block, and as captured by the typical transmission curve of an STC 45 wall, high frequencies are filtered by the partition. Acoustic transmission through the wall is expected to contribute significantly to low frequency content and peak pressure, but is expected to be insignificant with regards to PLdB.

Use of a directional microphone in close proximity to the wall, and some height off the ground could have better illuminated some of these issues.

7.4 Implications for Architectural Design

Research in mitigation of the sonic boom at the ground is promising, and it's quite likely that instead of two thunder-crack like shocks, next generation supersonic aircraft will be significantly milder. That said, the research presented here offers heuristic guidelines and a modeling tool to guide architectural design.

Heuristic guidelines are as follows:

1. Avoid placing windows near corners where exterior walls meet (where the open exterior angle is less than 90°).

2. Avoid exterior walls meeting in acute corners, the more obtuse the angle the better. This effect can be quantified with the software tool provided.

3. If the most common flight paths are known, rotate any corners where exterior walls meet such that they point away from the aircraft's approach.

4. Plant shrubbery around the exterior perimeter of the building, particularly

facing the aircraft's approach to prevent listeners from standing in areas with the largest amplification due to the structure.

5. Similarly, plant shrubbery around exterior corners that occlude the incoming shock ways, such that people don't stand in the portion of the shadow zone where edge diffraction predicts significant PLdB (close to the edge).

6. If the most common flight paths are known, use the simulation tool offered in this work to calculate where there are zones of significant building amplification due to multiple reflections. Try to use outdoor architectural features to discourage listeners from occupying those spaces. For example, don't put a bench where the Specular PLdB prediction tool predicts a peak SPL.

7. Place outdoor features that are attractive to listeners deep in shadow zones, far from occluding corners.

7.5 Future Work

Software tools with similar goals, which draw contours of metrics and calculate pressure fields at doors, are typically made by teams, and are the the result of many man-years of work. The tool here is certainly research-code, and far from polished despite the ability to generate some potentially useful graphics.

It's known that the limiting case for sonic boom legalization is not the outdoor experience, but the indoor experience. It is conceivable that the model presented here could be used to calculate pressure loading on exterior surfaces as inputs for an FEM model of the structure.

While unlikely, it's also conceivable that the software tool would actually find utility in architectural design under a known sonic boom flight path.
The following studies and tasks would either further one of those two applications, or would be generally illuminating.

1. Compare the Diffracted Transfer Function to the Maekawa and Pierce Continuous Wave Solutions [22] , Maekawa1968

2. Generalize the 1st order edge diffraction calculation, such that it can be accessed from within the existing specular field calculation and visualization tool. This mostly consists of a lot of book-keeping with regards to the visibility of partial edges from the receiver position.

3. A more thorough comparison of simulated and measured pressures around the residential structure - the contour plot presentation of simulated Pressures and PLdB, and the tables of measured building amplification do not allow for easy quantitative comparison of simulated and measured human impact.

4. Compare the BTM based results with Svensson's similar implementation [44] as implemented in his Matlab Toolbox.

5. In a similar vein to Svensson's work, decompose a time-domain diffracted impulse response into a line array of point sources, each contributing a single sample at the receiver position. This would enable higher order diffraction and mixed specular/diffracted paths.

Chapter 8

Documentation of Software Tool

Before closing this document, in hopes that others will find utility and might improve in the software modules used to perform these simulations, some documentation is in order.

8.1 Source Code

The code may be found at: `https://github.com/mandalin/DissertationCODE`.

8.2 Dependencies

This application was compiled with gcc-4.5.2, and utilized the following libraries.

1. VTK - visualization toolkit for generation of renderings and contours.
2. fftw - fast fourier transforms for filtered reflections.
3. boost.1.45.0 - boost for matrix multiplications, complex numbers were handled outside of boost.
4. STXXL - for the ability to write one IR while continuing calculations for the next IR.

8.3 Workflow

The code is far from appropriate for casual consumer use. It is very much a "research" codebase. In it's current state, it lacks a GUI front end for the settings, and also lacks the refinement of an independent settings file. Simulation settings, including geometry selection, are asserted in `OneSourcePos.h`. Details regarding the settings are presented in Section 8.4.

New geometries may be defined in their own header files. In order of relative complexity, the following geometries are already available for simulation:

1. `geometry_generalized_box.h` - Box geometry mimicking simple simulation from M.S. Thesis.

2. `geometry_generalized.h` - L-shaped building.

3. `geometry_IsolatedWall.h` - The Isolated Wall geometry discussed extensively in this document.

4. `geometry_generalized_Albert.h` - A complicated wall, corresponding to an experiment and published results performed by W.C.K. Alberts [87].

5. `generalized_geometry_52Blackbird.h` - An instrumented duplex once located on Edwards Airforce Base, utilized in this document.

6. `generalized_geometry_CSF.h` - A building of modern construction, once instrumented as part of the SonicBOBS experiment. The Combined Services Facility.

7. `ISM_DEM_PAMAP_LoadOneTile.h` - Any tile from a particular GIS dataset (with 5' horizontal resolution) of the area surrounding and including Pine Creek Gorge.

When a simulation is run, it may be run for a handful of listener or virtual microphone positions, or many listener positions may be automatically generated above flagged ground planes. In either case, the simulation creates one text file for each listener position. Each of these text files contains the specular impulse response at that location.

Once text files containing the impulse responses have been generated, as shown in figure 3.2.1.3, a Matlab script (given in Appendix D) is used to perform convolution and calculate metrics.

If one would like to visualize these contours among the simulation geometry, the original simulation is essentially re-run, except `Plot_Contour` is set to true, and the type of contour is selected. As such, the determination of pressure fields, and calculation of metrics is essentially a two step process. The simulation is not permitted to proceed after the rendering is generated.

8.4 Settings

```
/////////////////////////////
//                         //
//                         //
//    Simulation Settings  //
//                         //
//                         //
/////////////////////////////

// Where to Store Output
char              new char 1000
//--------Save Directory
strcat           "/Volumes/AMPULINA/2017/BlackBird/GroundLevel/SpecularIR/"


char * Which_Simulation_ = new char 20];
snprintf(Which_Simulation_, 20, "%i",  Which_Simulation);
strcat(directory,Which_Simulation_);
strcat(directory,"/");

//--------Order of Simulation
int max_order=10;

//--------Receiver Positions
bool SubSampleSurface=true;             //must be true for plotting a contour
bool AddEdgesToSubsample=false;
bool OnlyGroundPlanesSubsampled=true;   //must add ground plane list to this.
                                        //If SubSampleSurface=false,
                                        //this var is of noconsequence, no subsampling occurs.

//--------Height Above Plane For Subsampled Surfaces
//double height_above_plane=1.2;         //1.2 meters listener height
double height_above_plane=.003175;       // 1/8" above the plane


//--------Diffraction
bool BTMSIM=false;

//--------Filtering
bool dont_use_filtering=true;
bool use_R_coeffs=false;
bool use_R_coeffs_and_Disk_Approx=false;

//--------GeometrySimple
bool Box=false;
bool L_shaped=false;
bool Blackbird=true;
bool CSF=false;
bool Albert=false;
bool Canyon=false;
bool Isolated_Wall=false;
```

Figure 8.1: Simulation Settings

```
if L_shaped)
{   resolution=2;}      //BlackBird_sim_37_noHPFing, All L shape Sims
if Blackbird)
{   resolution=1;}      //Blackbird_sim_0_noHPFing
if Isolated_Wall)
{   resolution=10;}     //Isolated Wall

//Plotting of Geometry and Receivers
bool plot_geom=true;
bool Plot_RecPos=false; //dont use with subsampled receiver surfaces !
bool Plot_MicPos=true;

//Plotting of Contours
bool Plot_Contour=false;
bool Save_Contour=false;
bool PldB_Plot=false;
bool Pmax_Plot=false;
bool NumRefs_Plot=false;

//NumRefs Contours
const char   contourFileName "/Volumes/AMPULINA/2017/Wall/GroundLevel/SpecularContour/1 commit
428f65ed0d89646c474499b3b6be6a02c1863111/PLdB_Contour_Wall_2 copy.txt";
```

Figure 8.2: Simulation Settings

8.5 Specular Reflection Computation Time

Table 8.1: Specular Computation Time

Simulation	IRs	Planes	O. Req.	O. Sim.	IR Comp.	Conv.
Wall,1/8"	6127	9	4th	10th	44 min	2.5 hrs
L, 1.2m	20560	11	8th	10th	2 hrs	8 hrs
Blackbird	3314	122	>= 8th	10th	4 hrs 54 min	

Bibliography

[1] H. Kuttruff. *Room Acoustics*. Spoon Press, 5th edition, 2009.

[2] E. A. Haering Jr, L. J. Cliatt, T. J. Bunce, T. B. Gabrielson, V. W. Sparrow, and L. L. Locey. Initial results from the variable intensity sonic boom propagation database. Number 3034, Vancouver, British Columbia Canada, May 2008. 14th AIAA/CEAS Aeroacoustics Conference (29th AIAA Aeroacoustics Conference).

[3] A. B. Lind. Modeling specular reflections and post boom noise to augment synthesized outdoor sonic boom signatures. *http://etda.libraries.psu.edu/catalog/10520* Master's thesis, The Pennsylvania State University, Old Main, State College, PA 16801, May 2011.

[4] P. A. Henne. The case for small supersonic civil aircraft. Number AIAA 2003-2555. AIAA/ICAS International Air and Space Symposibum and Exposition, American Institute of Aeronautics and Astronautics, 2003.

[5] B. M. Sullivan, P. Davies, K. K. Hodgdon, J. A. Salamone. III, and A. Pilon. Realism assessment of sonic boom simulators. *Noise Control Eng. J.*, 56(2):141–157, March-April 2008.

[6] E. A. Haering Jr., J. W. Smolka, J. E. Murray, and H. J. Plotkin. Flight demonstration of low overpressure N-wave sonic booms and evanescent waves. volume 838. AIP Conf. Proc., 2006.

[7] J. Blauert. *Spatial Hearing, The Psychophysics of Human Sound Localization*. MIT Press, Cambridge Massachusetts, revised edition, 1997.

[8] H. Moller. Hearing at Low and Infrasonic Frequencies *Noise & Health*, 6(23):37–57, March 2004.

[9] K. J. Plotkin and D. J. Maglieri. Sonic boom research: History and future. Number AIAA 2003-3575, Orlando, Florida, June 2003. 33rd AIAA Fluid Dynamics Conference and Exhibit.

[10] J. D. Leatherwood and B. M. Sullivan. Laboratory study of effects of sonic boom shaping on subjective loudness and acceptability. Technical Paper 3269, National Aeronautics and Space Administration (NASA), NASA Langley Research Center, Hampton, VA 23681-0001, October 1992.

[11] B. M. Sullivan and J. D. Leatherwood. Subjective response to simulated sonic booms with ground reflections. Technical Memorandum 107764, National Aeronautics and Space Administration (NASA), Langley Research Center, Hampton, Virginia 23681-0001, June 1993.

[12] A. Loubeau, Y. Naka, B. G. Cook, V. W. Sparrow, and J. M. Morgenstern. A new evaluation of noise metrics for sonic booms using existing data. volume 1685 of *AIP Conference Proceedings*, http://aip.scitation.org/doi/abs/10.1063/1.4934481, October 2015. AIP.

[13] J. W. Pawlowski, D. H. Grahm, C. H. Boccadoro, P. G. Coen, and D. J. Maglieri. Origins and overview of the shaped sonic boom demonstration program. Number AIAA 2005-5, Reno, Nevada, January 2005. 43rd AIAA Aerospace Sciences Meeting and Exhibit.

[14] D. H. Graham, J. A. Dahlin, K. B. Meredith, and J. L. Vadnais. Aerodynamic design of shaped sonic boom demonstration aircraft. Number AIAA 2005-8, Reno, Nevada, January 2005. 43rd AIAA Aerospace Sciences Meeting and Exhibit, American Institute of Aeronautics and Astronautics.

[15] D. C. Howe. Improved sonic boom minimization with extendable nose spike. Number AIAA 2005-1014, Reno, Nevada, January 2005. 43rd AIAA Aerospace Sciences Meeting and Exhibit, American Institute of Aeronautics and Astronautics.

[16] D. G. Albert. Observations of acoustic surface waves in outdoor sound propagation. *Journal of the Acoustical Society of America*, 113(5):2495–2500, May 2003.

[17] R. R. Torres. Computation of edge diffraction for more accurate acoustics auralization. *Journal of the Acoustical Society of America*, 109(2):600–610, September 2001.

[18] W. C. K. Alberts II. On the application of well-known diffraction models to the sound field in the shadow zone of an isolated building. *Applied Acoustics*, 70:1128–1130, March 2009.

[19] Z. Maekawa. Noise reduction by screens. *Applied Acoustics*, 1(3):157–173, July 1968.

[20] CATT, Mariagatan 16A SE-41471 Gothenburg Sweden. *CATT-Acoustic V8g : Room Acoustics Prediction and Walkthrough Auralization*, August 2008.

[21] C. L. Christensen. *Odeon User Manual: Industrial, Auditorium and Combined*. Scion DTU, Diplomvej, building 381, Denmark, version 11, 2nd edition edition, 2011.

[22] A. D. Pierce. Diffraction of sound around corners and over wide barriers. *Journal of the Acoustical Society of America*, 55:941–955, 1974.

[23] A. J. Rudgers. Separation and analysis of the acoustic field scattered by a rigid sphere. *The Journal of the Acoustical Society Of America*, 52(1):234–247, November 1971.

[24] J. S. Asvestas, J. Bowman, P. Christiansen, O. Einarsson, R. E. Kleinman, D. L. Sengupta, T. B. A. Senior, F. B. Sleator, P. L. E. Uslenghi, and N. R. Zitron. *Electromagnetic and Acoustic Scattering by Simple Shapes*. Hemisphere Publishing Corporation, Radiation Laboratory, The university of Michigan, USA, 2nd edition edition, 1987.

[25] L. J. Chu and J. A. Stratton. Elliptic and spheroidal wave functions. *Journal of Mathematics and Physics*, 20(1-4):259–309, April 1941.

[26] J. Gutierrez-Vega, R. M. Rodriguez-Dagnino, M. A. Meneses-Nava, and S. Chavez-Cerda. Mathieu functions, a visual approach. *American Journal of Physics*, 71(3):233–242, March 2003.

[27] C. Sun. Explicit equations to transform from cartesian to elliptic coordinates. *Mathematical Modelling and Applications*, 2(4):43–46, January 2017.

[28] R. Holland and V. P. Cable. Mathieu functions and their applications to scattering by a coated strip. *IEEE Transactions on Electromagnetic Compatibility*, 34(1):9–16, February 1992.

[29] H. Kuttruff. *room acoustics*. Spon Press, Institut für Technische Akustik, Technische Hochschule Aachen, Aachen, Germany, 5th edition, 2009.

[30] S. I. Cho. Three-dimensional finite-difference time-domain simulation of low-amplitude sonic boom diffraction around a rectangular test structure and building spiking effect. (a). *Journal of the Acoustical Society of America*, 127(3):1884–1884, March 2010.

[31] S. T. Cho. *Finite-Difference Time-Domain Modeling of Low-Amplitude Sonic Boom Diffraction Around Building Structures*. PhD thesis, The Pennsylvania State University, Old Main, State College, PA 16801, August 2012.

[32] C. Hart. *On a combined adaptive tetrahedral tracing and edge diffraction model*. PhD thesis, University of Nebraska Lincoln, 1400 R St, Lincoln, NE 68588, May 2014.

[33] F. P. Mechel. Improved mirror source method in room acoustcs. *Journal of Sound and Vibration*, 256(5):873–940, 2002.

[34] N. Damera-Venkata and B. L. Evans. Optimal design of real and complex minimum phase digitial fir filters. ICASSP, 1999.

[35] N. Damera-Venkata and B. L. Evans. Optimum design of real and complex minimum phase digital filters. Austin, TX 78712-1084 USA, 1999.

[36] D. P. Hewett. Sound propagation in an urban environment, Hilary Term 2010.

[37] A. D. Pierce. *Acoustics : An Introduction to its Physical Principles and Applications*. Acoustical Society of America through the American Institue of Physics, 1994.

[38] E. Skudrzyk. *The Foundations of Acoustics*. Springer - Verlag, The Pennsylavnia State University, 1971.

[39] E. F. Knott. A progression of high-frequency rcs prediction techniques. *Proceedings of the IEEE*, 73(2):252–262, February 1985.

[40] M. Long. *Architectural Acoustics*. Elsevier Academic Press, 30 Corporate Drive, Suite 400, Burlington, MA 01803, USA, 2006.

[41] J. B. Keller and A. Blank. Diffraction and reflection of pulses by wedges and corners. *Communications on Pure and Applied Mathematics*, 4(1):75–94, June 1951.

[42] M. A. Biot and I. Tolstoy. Formulation of wave propagation in infinite media by normal coordinates with an application to diffraction. *The Journal of the Acoustical Society Of America*, 29(3):381–391, March 1957.

[43] H. Medwin, E. Childs, and G. M. Jebsen. Impulse studies of double diffraction: A discrete Huygen's interpretation. *Acoustical Society of America*, 72(3):1005–1013, September 1982.

[44] U. P. Svensson and R. I. Fred. An analytic secondary source model of edge diffraction impulse responses. *Journal of the Acoustical Society of America*, 106(5):2331–2344, November 1999.

[45] H. Medwin. Shadowing by finite noise barriers. *Journal of the Acoustical Society of America*, 69(4):1060–1064, April 1981.

[46] J. Klos and R. D. Buehrle. Vibro-acoustic response of buildings due to sonic boom exposure : June 2006 Field Test. Technical Memorandum 214900, NASA, Langley Research Center, Hampton, Virginia 23681-2199, September 2007.

[47] F. G. Friedlander. *Sound Pulses*. The Syndics of the Cambridge University Press, 32 East 57th Street, New York 22, N.Y., 1958.

[48] California Department of Health Services Local Environmental Health Services Branch, 714 P Street - Sacramento, CA 95814. *Catalog of STC and IIC Ratings for Wall and Floor/Ceiling Assemblies*.

[49] D. A. McNamara, C. W. I. Pistorius, and J. A. G. Malherbe. *Introduction To The Uniform Geometrical Theory of Diffraction*. ARTECH HOUSE, 1990.

[50] B. DeWitt and W. Burnside. Analysis and measurement of electromagnetic scattering by pyramidal and wedge absorbers. Dissertation 716148-10, The Ohio State University ElectroScience Laboratory Department of Electrical Engineering, Columbus, Ohio 43212, March 1986.

[51] B. DeWitt and W. Burnside. Analysis and measurement of electromagnetic scattering by pyramidal and wedge absorbers. Dissertation 716148-10, The Ohio State University ElectroScience Laboratory Department of Electrical Engineering, Columbus, Ohio 43212, March 1986.

[52] L. L. Locey. *Sonic Boom Postprocessing Functions To Simulate Atmospheric Turbulence Effects*. PhD thesis, Pennsylvania State University, 201 Applied Science Bldg. University Park, PA 16802, August 2008.

[53] W. C. K. Alberts II, J. M. Nobel, and M. A. Coleman. Sound propagation in the vicinity of an isolated building an experimental investigation. *Journal of the Acoustical Society of America*, 124(2):733–742, August 2008.

[54] T. T. Bui. CFD analysis of nozzle jet plume effects on sonic boom signature. Number 47th, Orlando, Florida, January 2009. Aerospace Sciences Meeting Including The New Horizons Forum and Aerospace Exposition.

[55] E. J. Walker and P. E. Doak. Effects of ground reflection on the shapes of sonic bangs. Number L55, Liege, September 1965. 5th International Congress of Acoustics.

[56] P. M. Morse. *VIbration and Sound*. Acoustical Society of America through the American Institue of Physics, 1995.

[57] R. V. Waterhouse. *Journal of the Acoustical Society of America* 27(2):247–258, March 1995.

[58] L. H. Keith Attenborough, Kai Ming Li. *Predicting Outdoor Sound.* Taylor & Francis, 2007.

[59] International Standard. *Acoustics - Attenuation of sound during propagation outdoors - Part 2: General method of calculation*, ISO 9613-2-1996 edition, 1996.

[60] M. E. Delany and E. N. Bazley. Acoustical properties of fibrous absorbent materials. *Applied Acoustics*, 3:105–116, 1970.

[61] S. I. Cho and V. W. Sparrow. Three-dimensional numerical simulation of sonic boom diffraction around buildings using a dispersion-relation-preserving scheme. (a). *Journal of the Acoustical Society of America*, 125(4):2631–2631, April 2009.

[62] E. Granier, M. Kleiner, B.-I. Dalenbäck, and P. Svensson. Experimental auralization of car audio installations. Paris, France, February 1995. Audio Engineering Society.

[63] N. Tsingos. Using programmable graphics hardware for acoustics and audio rendering. Number 7850. 127th Convention of the Audio Engineering Society, October 2009.

[64] N. Tsingos, C. Dachsbacher, S. Lefebvre, and M. Dellepiane. Instant sound scattering. Rendering Techniques, Proc. of the Eurographics Symposium on Rendering, 2007.

[65] H. M. Gary M. Jebsen. On the failure of the Kirchhoff assumption in backscatter. *Journal of the Acoustical Society of America*, 72(5):1607, November 1982.

[66] F. Fahy and P. Gardonio. *Sound and Structural Vibration.* Elsevier, Linacre House, Jordan Hill, Oxford OX2 8DP, UK, 2nd edition, 2007.

[67] M. Ochmann. The complex equivalent source method for propagation over an impedance plane. *Journal of the Acoustical Society of America*, 116(6):3304–3311, December 2004.

[68] M. E. Johnson, S. J. Elliot, K.-H. Baek, and J. Garcia-Bonito. An equivalent source technique for calculating the sound field inside an enclosure containing scattering objects. *Journal of the Acoustical Society of America*, 104(3):1221–1231, February 1998.

[69] American National Standard. *Method for calculation of the absorption of sound by the atmosphere*, ansi s1.26-1995 (asa 113-1995) edition, June 2009.

[70] H. Fastl, Eberhard Zwicker. *Psychoacoustcs : Facts and Models.* 3rd Ed, Springer, 2007.

[71] K. W. Henderson and W. H. Kautz. Transient responses of conventional filters. *IRE Transactions on Circuit Theory*, 5(4):333–347, December 1958.

[72] T. F. Quatieri. *Discrete-Time Speech Signal Processing*. Prentice Hall, November 2001.

[73] J. Klos. Vibro-acoustic response of buildings due to sonic boom exposure : July 2007 field test. TM NASA/TM-2008-215349, National Aeronautics and Space Administration (Nasa), Langley Research Center, Hampton, Virginia 23681-2199, September 2008.

[74] K. A. Riegel. *Propagation of Sonic Booms in Urban Landscapes*. PhD thesis, The Pennsylvania State University, Old Main, State College, PA 16801, 2011.

[75] G. Schulze, A. Jirasek, M. M. L. Yu, A. Lim, R. F. B. Turner, and M. W. Blades. Investigation of selected baseline removal techniques as candidates for automated implementation. *Applied Spectroscopy*, 59(5):545–574, January 2005.

[76] J. D. Leatherwood, B. M. Sullivan, K. P. Shepherd, D. A. McCurdy, and S. A. Brown. Summary of recent nasa studies of human response to sonic booms. *Journal of the Acoustical Society of America*, 111(1):586–598, January 2002.

[77] M. Vorländer. *Auralization: Fundamentals of Acoustics, Modelling, Simulation, Algorithms and Acoustic Virtual Reality*. Springer, 1st edition, November 2007.

[78] T. B. Gabrielson, S. M. Willits, T. M. Marston, E. A. Haering Jr, J. E. Murray, Lt. CoL. M. Stucky. Acoustic Background noise from sailplane-mounted microphones. Inter-Noise, Honolulu, Hawaii, December 2006.

[79] T. F. W. Embleton. Tutorial on sound propagation outdoors. *Journal of the Acoustical Society of America*, 100(1):31–48, July 1996.

[80] E. M. Salomons. *Computational Atmospheric Acoustics*. Kluwer Academic Publishers, Delft, The Netherlands, 2001.

[81] Template method for ground impedance. ANSI S1.18-1999, American National Standard, 1999, 2004.

[82] J. E. Piercy, T. F. W. Embleton, and L. C. Sutherland. Review of noise propagation in the atmosphere. *Journal of the Acoustical Society of America*, 61(6):1403–1418, June 1977.

[83] T. F. W. Embleton, J. E. Piercy, and N. Olson. Outdoor sound propagaton over ground of finite impedance. *Journal of the Acoustical Society of America*, 59(2):267–277, February 1976.

[84] S. Bradley. *Acoustic Atmospheric Remote Sensing.* CRC Press, Boca Raton, FL, 2008.

[85] P. Svensson. Acoustics group ntnu Trondheim Norway, edge diffraction toolbox, last checed sept. 2010 http://www.iet.ntnu.no/ svensson/software/index.html.

[86] P. U. Svensson and P. T. Calamia. Edge diffraction in room acoustics computer modeling. Inter-Noise, Honolulu, Hawaii, December 2006.

[87] W. C. K. Alberts, J. M. Nobel, and M. A. Coleman. Sound propagation in the vicinity of an isolated building an experimental investigation. *Journal of the Acoustical Society of America*, 124(2):733–742, August 2008.

Appendix A: BTM Validation

Contents

BTM Validation without scaling or averaging, fs=110kHz

```
fs was defined, such that the time domain IR matched

clear all
close all
clc

%Define Physical Properties
c=343;
rho=1.2;

%Define Geometrical Properties
theta_omega=270*(pi/180);
theta=225*(pi/180);
theta_o=45*(pi/180);
r=100;
ro=100;
Z=0;
epsilon=[.1,.5,1,10]*(pi/180); %penetration into the shadow zone
theta=theta+epsilon;
```

```
%Define Discrete Signals
fs=110000;
delta_t=1/fs;
n=0:110000*10;  %long enough that spectra converges
tau=n*delta_t;  %this is the time AFTER the "least time"
tau_o=(((r+ro)^2+Z^2)^(1/2))/c; %this is the "least time
t=tau_o+tau;    %this is the absolute time

%This is an ambigous scaling factor I quite dislike.
S=1;

Yarg=(c*c*t.*t-(r*r+ro*ro+Z*Z))./ (2*r*ro);
if (Yarg<0)
display ( 'error' )
end

Y=acosh(Yarg);
figure(3);
for (i=1:length(theta))

    Beta_Denom_pp=1-2*exp(-pi*Y/theta_omega)*cos((pi/theta_omega)* ...
        (pi+theta(i)+theta_o))+exp(-2*pi*Y/theta_omega);

    Beta_Denom_pm=1-2*exp(-pi*Y/theta_omega)*cos((pi/theta_omega)* ...
        (pi+theta(i)-theta_o))+exp(-2*pi*Y/theta_omega);

    Beta_Denom_mm=1-2*exp(-pi*Y/theta_omega)*cos((pi/theta_omega)* ...
        (pi-theta(i)-theta_o))+exp(-2*pi*Y/theta_omega);

    Beta_Denom_mp=1-2*exp(-pi*Y/theta_omega)*cos((pi/theta_omega)* ...
        (pi-theta(i)+theta_o))+exp(-2*pi*Y/theta_omega);

    Beta_Num_pp=sin((pi/theta_omega)*(pi+theta(i)+theta_o));
    Beta_Num_pm=sin((pi/theta_omega)*(pi+theta(i)-theta_o));
    Beta_Num_mp=sin((pi/theta_omega)*(pi-theta(i)+theta_o));
    Beta_Num_mm=sin((pi/theta_omega)*(pi-theta(i)-theta_o));

    Beta=Beta_Num_pp./Beta_Denom_pp + Beta_Num_pm./Beta_Denom_pm +...
        Beta_Num_mp./Beta_Denom_mp + Beta_Num_mm./Beta_Denom_mm;
```

```
    p(i,:)=((-S*rho*c)/(4*pi*theta_omega))*Beta.*((r*ro*sinh(Y)).^-1).*...
        exp(-pi.*Y/theta_omega);


    p(i,1)=p(i,2);
     p(i,1:3)
    plot(n,p(i,:))
    hold on
end


set(gca,'XScale','log')
set(gca,'YScale','log')
AX=legend('e=.1ą', 'e=.5ą ','e=1ą', 'e=10ą')
set(AX,'FontSize',16)
ylim([.1,5])
xlim([.99,5])
%axis tight
title('Fig. 2  Medwin 1982 Rep.','FontSize',16)
xlabel('n','FontSize', 16)
ylabel('Relative Pressure p(n?t)','FontSize',16)


R=ro+r;
freefield=zeros(size(p(i,:)));
%freefield(round((R/c)/delta_t))=(rho*S)/(4*pi*(ro+r)); //for phase
freefield(1)=(rho*S)/(4*pi*(ro+r));

[f,N,delta_f,delta_t,X,Gxx,Xrms]=Lind_PSD(freefield,fs);
Freefield=abs(Gxx);

shapes={'d','^','o','s'}
for i=1:length(theta)
    x=p(i,:);
    [f,N,delta_f,delta_t,X,Gxx,Xrms]=Lind_PSD(x,fs);
    P(i,:)=abs(Gxx);

    figure(4)
    semilogx(f,10*log10(P(i,:)./Freefield))
```

```
    hold on
end
hold off


    xlabel(’Frequency [Hz]’,’FontSize’, 16)
    ylabel(’dB re. Free field at r_o + r’,’FontSize’, 16)
    AX=legend(’e=.1ą’, ’e=.5ą ’,’e=1ą’, ’e=10ą’)
    set(AX,’FontSize’,16)
    xlim([1000,40000])
    title({’Power Spectral Density of the Diffracted Impulse Response’;...
    ’Divided by the PSD of FreeField IR’;...
    ’Free Field impulse as Kronicker delta’; ’fs=110kHz’}, ’FontSize’,16)

    filename=strcat(’1.png’)
    print(filename,’-dpng’)
    cd(’/Users/mandalin/Documents/MATLAB/BTM Confirmation’)
```

BTM Validation after scaling, without averaging, fs=110kHz

```
freefield IR scaled by the sampling period

clear all
close all
clc

%Define Physical Properties
c=343;
rho=1.2;

%Define Geometrical Properties
theta_omega=270*(pi/180);
theta=225*(pi/180);
theta_o=45*(pi/180);
r=100;
ro=100;
Z=0;
epsilon=[.1,.5,1,10]*(pi/180); %penetration into the shadow zone
theta=theta+epsilon;
```

```
%Define Discrete Signals
fs=110000;
delta_t=1/fs;
n=0:110000*10;  %long enough that spectra converges
tau=n*delta_t;  %this is the time AFTER the "least time"
tau_o=(((r+ro)^2+Z^2)^(1/2))/c; %this is the "least time
t=tau_o+tau;    %this is the absolute time

%This is an ambigous scaling factor I quite dislike.
S=1;

Yarg=(c*c*t.*t-(r*r+ro*ro+Z*Z))./ (2*r*ro);
if (Yarg<0)
display ( 'error' )
end

Y=acosh(Yarg);
figure(3)
for (i=1:length(theta))

    Beta_Denom_pp=1-2*exp(-pi*Y/theta_omega)*cos((pi/theta_omega)* ...
        (pi+theta(i)+theta_o))+exp(-2*pi*Y/theta_omega);

    Beta_Denom_pm=1-2*exp(-pi*Y/theta_omega)*cos((pi/theta_omega)* ...
        (pi+theta(i)-theta_o))+exp(-2*pi*Y/theta_omega);

    Beta_Denom_mm=1-2*exp(-pi*Y/theta_omega)*cos((pi/theta_omega)* ...
        (pi-theta(i)-theta_o))+exp(-2*pi*Y/theta_omega);

    Beta_Denom_mp=1-2*exp(-pi*Y/theta_omega)*cos((pi/theta_omega)* ...
        (pi-theta(i)+theta_o))+exp(-2*pi*Y/theta_omega);

    Beta_Num_pp=sin((pi/theta_omega)*(pi+theta(i)+theta_o));
    Beta_Num_pm=sin((pi/theta_omega)*(pi+theta(i)-theta_o));
    Beta_Num_mp=sin((pi/theta_omega)*(pi-theta(i)+theta_o));
    Beta_Num_mm=sin((pi/theta_omega)*(pi-theta(i)-theta_o));

    Beta=Beta_Num_pp./Beta_Denom_pp + Beta_Num_pm./Beta_Denom_pm +...
        Beta_Num_mp./Beta_Denom_mp + Beta_Num_mm./Beta_Denom_mm;
```

```
    p(i,:)=((-S*rho*c)/(4*pi*theta_omega))*Beta.*((r*ro*sinh(Y)).^-1).*...
        exp(-pi.*Y/theta_omega);


    p(i,1)=p(i,2);
     p(i,1:3)
    plot(n,p(i,:))
    hold on
end


set(gca,'XScale','log')
set(gca,'YScale','log')
AX=legend('e=.1ą', 'e=.5ą ','e=1ą', 'e=10ą')
set(AX,'FontSize',16)
ylim([.1,5])
xlim([.99,5])
%axis tight
title('Fig. 2  Medwin 1982 Rep.','FontSize',16)
xlabel('n','FontSize', 16)
ylabel('Relative Pressure p(n?t)','FontSize',16)


R=ro+r;
freefield=zeros(size(p(i,:)));
%freefield(round((R/c)/delta_t))=(rho*S)/(4*pi*(ro+r)); //for phase
freefield(1)=(rho*S)/(4*pi*(ro+r)*delta_t);

[f,N,delta_f,delta_t,X,Gxx,Xrms]=Lind_PSD(freefield,fs);
Freefield=abs(Gxx);

shapes={'d','^','o','s'}
for i=1:length(theta)
    x=p(i,:);
    [f,N,delta_f,delta_t,X,Gxx,Xrms]=Lind_PSD(x,fs);
    P(i,:)=abs(Gxx);

    figure(4)
    semilogx(f,10*log10(P(i,:)./Freefield))
```

```
    hold on
end
hold off

    xlabel('Frequency [Hz]','FontSize', 16)
    ylabel('dB re. Free field at r_o + r','FontSize', 16)
    AX=legend('e=.1ą', 'e=.5ą ','e=1ą', 'e=10ą')
    set(AX,'FontSize',16)
    xlim([1000,40000])
    title({'Power Spectral Density of the Diffracted Impulse Response';...
    'Divided by the PSD of FreeField IR';...
    'Free Field impulse as Dirac delta';'fs=110kHz'}, 'FontSize',16)

    filename=strcat('2.png')
    print(filename,'-dpng')
    cd('/Users/mandalin/Documents/MATLAB/BTM Confirmation')
```

BTM Validation after scaling, without averaging, fs=1.1GHz

```
increasing fs improved agreement with the spectra
"n" in the time domain plot IR would be need to n*10000

clear all
%close all
clc

%Define Physical Properties
c=343;
rho=1.2;

%Define Geometrical Properties
theta_omega=270*(pi/180);
theta=225*(pi/180);
theta_o=45*(pi/180);
r=100;
ro=100;
Z=0;
epsilon=[.1,.5,1,10]*(pi/180); %penetration into the shadow zone
theta=theta+epsilon;
```

```
%Define Discrete Signals
fs=110000*10000;
delta_t=1/fs;
n=0:110000*10;
tau=n*delta_t;  %this is the time AFTER the "least time"
tau_o=(((r+ro)^2+Z^2)^(1/2))/c; %this is the "least time
t=tau_o+tau;    %this is the absolute time

%This is an ambigous scaling factor I quite dislike.
S=1;

%Y=acosh( ((c A2)*(2*tau o*tau+tau. A2)/(2*r*ro)) + 1); //Alternate Form
Yarg=(c*c*t.*t-(r*r+ro*ro+Z*Z))./ (2*r*ro);
if (Yarg<0)
display ( 'error' )
end

Y=acosh(Yarg);
figure(3)
for (i=1:length(theta))

    Beta_Denom_pp=1-2*exp(-pi*Y/theta_omega)*cos((pi/theta_omega)* ...
        (pi+theta(i)+theta_o))+exp(-2*pi*Y/theta_omega);

    Beta_Denom_pm=1-2*exp(-pi*Y/theta_omega)*cos((pi/theta_omega)* ...
        (pi+theta(i)-theta_o))+exp(-2*pi*Y/theta_omega);

    Beta_Denom_mm=1-2*exp(-pi*Y/theta_omega)*cos((pi/theta_omega)* ...
        (pi-theta(i)-theta_o))+exp(-2*pi*Y/theta_omega);

    Beta_Denom_mp=1-2*exp(-pi*Y/theta_omega)*cos((pi/theta_omega)* ...
        (pi-theta(i)+theta_o))+exp(-2*pi*Y/theta_omega);

    Beta_Num_pp=sin((pi/theta_omega)*(pi+theta(i)+theta_o));
    Beta_Num_pm=sin((pi/theta_omega)*(pi+theta(i)-theta_o));
    Beta_Num_mp=sin((pi/theta_omega)*(pi-theta(i)+theta_o));
    Beta_Num_mm=sin((pi/theta_omega)*(pi-theta(i)-theta_o));

    Beta=Beta_Num_pp./Beta_Denom_pp + Beta_Num_pm./Beta_Denom_pm +...
        Beta_Num_mp./Beta_Denom_mp + Beta_Num_mm./Beta_Denom_mm;
```

```
    p(i,:)=((-S*rho*c)/(4*pi*theta_omega))*Beta.*((r*ro*sinh(Y)).^-1).*...
        exp(-pi.*Y/theta_omega);


    p(i,1)=p(i,2);
     p(i,1:3)
    plot(n,p(i,:))
    hold on
end


set(gca,'XScale','log')
set(gca,'YScale','log')
AX=legend('e=.1ą', 'e=.5ą ','e=1ą', 'e=10ą')
set(AX,'FontSize',16)
ylim([.1,5])
xlim([.99,5])
%axis tight
title('Fig. 2  Medwin 1982 Rep.','FontSize',16)
xlabel('n','FontSize', 16)
ylabel('Relative Pressure p(n?t)','FontSize',16)


R=ro+r;
freefield=zeros(size(p(i,:)));
%freefield(round((R/c)/delta_t))=(rho*S)/(4*pi*(ro+r)); //for phase
freefield(1)=(rho*S)/(4*pi*(ro+r)*delta_t);

[f,N,delta_f,delta_t,X,Gxx,Xrms]=Lind_PSD(freefield,fs);
Freefield=abs(Gxx);

shapes={'d','^','o','s'}
for i=1:length(theta)
    x=p(i,:);
    [f,N,delta_f,delta_t,X,Gxx,Xrms]=Lind_PSD(x,fs);
    P(i,:)=abs(Gxx);

    figure(4)
    semilogx(f,10*log10(P(i,:)./Freefield))
```

```
    hold on
end
hold off

    xlabel('Frequency [Hz]','FontSize', 16)
    ylabel('dB re. Free field at r_o + r','FontSize', 16)
    AX=legend('e=.1ą', 'e=.5ą ','e=1ą', 'e=10ą')
    set(AX,'FontSize',16)
    xlim([1000,40000])
     title({'Power Spectral Density of the Diffracted Impulse Response';...
     'Divided by the PSD of FreeField IR';...
     'Free Field impulse as Dirac delta';'fs=1.1GHz'}, 'FontSize',16)

    filename=strcat('3.png')
    print(filename,'-dpng')
    cd('/Users/mandalin/Documents/MATLAB/BTM Confirmation')
```

Appendix B: Finite Disk Approximation & Minimum Phase

Contents

Inputs, these must be approximed based on facet dimensions.

```
d=10; %Smallest Dimension of the Plane
R=100;%Distance From the Center of the Plane
```

Constants and DSP variables

```
co=343;
fs=48000;
T=5;

N=fs*T;
delta_t=1/fs;
delta_f=fs/N;
f_single=0:delta_f:fs/2;
k_freqs=(f_single*2*pi)/co;
t=0:delta_t:N*delta_t;
f_double=[fliplr(f_single(2:length(f_single)-1)),f_single];
```

Pressure Based on the disk approx. find the PSD of the freq. resp.

```
PSqrdR_over_PSqrdl = (sin ((k_freqs*(d/2)^2)/(2*R))).^2;
FreqAtt=sqrt(PSqrdR_over_PSqrdl);
    %maximum reflection coeff is 1 FreqAtt is the Linear
    %Spectrum of the pressure of the ref lected wave

ind1 = find(FreqAtt>=.9999, 1,'first');
Freq=ones(size(f_single)) ;
Freq(1:ind1)=Freq(1,1:ind1).*FreqAtt(1:ind1) ;
```

Minimum phase to complement the magnitude gives the the IR

```
%----See Damera-Venkata & Evans, reference (42)
clear ('y1')

H1 =[Freq,fliplr(Freq(2:length(Freq)- 1))].^2;
d1 =max(H1)-1;  %amount the real magnitude goes above 1
d2=0-min(H1);   %amount the real magnitude goes below O
S=4/(sqrt(1+d1+d2)+sqrt(1-d1+d2))^2;

H2=H1+d2 ;      %makes sure the magnitude never goes below 0
clear H1;
H3=H2*S;        %scales to keep the right relationship
HR=sqrt(H3)+1e-10;
clear H3;

y=dhtm(HR',N,2000);
clear HR;
y1 =real(y);
[h1]=freqz(y1,1,f_single,fs);
```

Appendix C: Hilbert Transform

Discrete Hilbert Transform for Calculating Minimum Phase Response

```
% dhtm.m
 function y=dhtm(mag,N,s)
 sig(1:(N/2))=sign(linspace(1,(N/2),(N/2)));
 sig((N/2)+1)=0;
 sig((N/2)+2:N)=sign(linspace(-1,-(N/2)-1,(N/2)-1));
 sig(1)=0;
 logmag=log(abs(mag));
 in=ifft(logmag);
 ph=-j*fft(sig'.*in);
 rec=mag.*exp(j*ph);
 recu=ifft(rec);
 y=recu(1:s);
 % End of program
```

Appendix D: Validated BTM Model Function

Contents

BTM function in matlab

```
function [Output] = BTMFuncValidate(theta_omega,theta,theta_o,r,ro,Z,...
    epsilon,calcFS, outputFS)
```

Define Physical Properties

```
c=343;
rho=1.2;


theta=theta+epsilon;
```

Define Discrete Signals

```
fs=calcFS;
delta_t=1/fs;
```

```
n=0:110000*10;  %long enough that spectra converges
tau=n*delta_t;  %this is the time AFTER the "least time"
tau_o=(((r+ro)^2+Z^2)^(1/2))/c; %this is the "least time
t=tau_o+tau;    %this is the absolute time
```

This is an ambigous scaling factor I used to quite dislike.

```
S=1;
```

Calculate

```
Yarg=(c*c*t.*t-(r*r+ro*ro+Z*Z))./ (2*r*ro);
if (Yarg<0)
display ( 'error' )
end

Y=acosh(Yarg);
figure(3)
for (i=1:length(theta))

    Beta_Denom_pp=1-2*exp(-pi*Y/theta_omega)*cos((pi/theta_omega)* ...
        (pi+theta(i)+theta_o))+exp(-2*pi*Y/theta_omega);

    Beta_Denom_pm=1-2*exp(-pi*Y/theta_omega)*cos((pi/theta_omega)* ...
        (pi+theta(i)-theta_o))+exp(-2*pi*Y/theta_omega);

    Beta_Denom_mm=1-2*exp(-pi*Y/theta_omega)*cos((pi/theta_omega)* ...
        (pi-theta(i)-theta_o))+exp(-2*pi*Y/theta_omega);

    Beta_Denom_mp=1-2*exp(-pi*Y/theta_omega)*cos((pi/theta_omega)* ...
        (pi-theta(i)+theta_o))+exp(-2*pi*Y/theta_omega);

    Beta_Num_pp=sin((pi/theta_omega)*(pi+theta(i)+theta_o));
    Beta_Num_pm=sin((pi/theta_omega)*(pi+theta(i)-theta_o));
    Beta_Num_mp=sin((pi/theta_omega)*(pi-theta(i)+theta_o));
    Beta_Num_mm=sin((pi/theta_omega)*(pi-theta(i)-theta_o));

    Beta=Beta_Num_pp./Beta_Denom_pp + Beta_Num_pm./Beta_Denom_pm +...
        Beta_Num_mp./Beta_Denom_mp + Beta_Num_mm./Beta_Denom_mm;
```

```
    p(i,:)=((-S*rho*c)/(4*pi*theta_omega))*Beta.*((r*ro*sinh(Y)).^-1).*...
        exp(-pi.*Y/theta_omega);

    p(i,1)=p(i,2);
    plot(p(i,:))

    hold on
end
```

Prepare Time Domain Plot

```
set(gca,'XScale','log')
set(gca,'YScale','log')
%axis tight
xlabel('n','FontSize', 16)
ylabel('p(n $\Delta$ t)','Interpreter','latex','FontSize',16)



R=ro+r;
%p=[p,zeros([1,22000000])]; %This is needs to be uncommented if you want to
%see full spectrum. Zeropadding to illuminate low freq spectrum.
```

Calcuate Scaling Factor

```
freefield=zeros(size(p(i,:)));
%freefield(round((R/c)/delta_t))=(rho*S)/(4*pi*(ro+r)); //for phase
freefield(1)=(rho*S)/(4*pi*(ro+r)*delta_t);

[f,N,delta_f,delta_t,X,Gxx,Xrms]=Lind_PSD(freefield,fs);
Freefield=abs(Gxx);
```

Calcuate Frequency Domain Plot

```
figure(10)
for i=1:length(theta)
    x=p(i,:);
    [f,N,delta_f,delta_t,X,Gxx,Xrms]=Lind_PSD(x,fs);
    P(i,:)=abs(Gxx);

    TransferFunc(i,:)=P(i,:)./Freefield;
```

```
    figure(4)
    semilogx(f,10*log10(TransferFunc(i,:)))

    hold on
end
hold off

    xlabel('Frequency [Hz]','FontSize', 16)
    ylabel('dB re. Free field at r_o + r','FontSize', 16)
    xlim([1,40000])
```

Output Solutions

```
for i=1:length(epsilon)
    Output.IR(i,:)=p(i,:);
    Output.TransferFunc(i,:)=P(i,:)./Freefield;
    Output.freefield=freefield;
    Output.Freefield=Freefield;
    Output.f=f;
    Output.delta_t=delta_t;
    Output.t=t;
    Output.ro=ro;
    Output.tau_o=tau_o;
end
```

Appendix E: Validated BTM Practical Application, Convolution, & Metric Calculation

Contents


```
% Load and Scale the Input Waveform For Isolated Wall
PLdBCalcFolder=...
'/Users/mandalin/Documents/Sort Me Now/DissertationPostProcessing';

InputFolder=...
strcat('/Users/mandalin/Documents/Sort Me Now/',...
'Dissertation_PLdB_PostProcessing/Inputs')
```

```
cd(InputFolder)
truncate_at=500;
load('Channel_188.mat')
%input = X_desired_fs/2;

%We need to do our own upsampling.... the upsampling above is wrong.
input_voltage_fs25600=Channel_188_Voltage;
input_pressure_fs25600=input_voltage_fs25600 / scaling_V_per_Pa;

input_pressure_fs25600x15 = interp(double(input_pressure_fs25600),15);
input_pressure_fs25600x15div8 = decimate(input_pressure_fs25600x15,8);
input=input_pressure_fs25600x15div8/2;
```

Load the Source and Receiver Positions corresponding to the Field Test

```
Qpos=[...
29308.603288793849
6662.516948284092
11096.71236590531];

QposSpec=[...
29308.603288793849
6662.516948284092
-11096.71236590531];

Ppos(202,:)=[... %pos 4 in Xcode]
0.91384297222625765,
-0.031912099784870529,
0.0031749999999999999];

Ppos(203,:)=[... %pos 5 in Xcode]
-0.063461317515712323
0.0022161180406160088
0.91757499999999992];

Ppos(201,:)=[... %pos 6 in Xcode]
-0.91384297222625765
0.031912099784870529
```

```
0.0031749999999999999
];

PropVector(201,:)=Qpos'-Ppos(201,:);
PropVector(202,:)=Qpos'-Ppos(202,:);
PropVector(203,:)=Qpos'-Ppos(203,:);

PropVectorSpec(201,:)=QposSpec'-Ppos(201,:);
PropVectorSpec(202,:)=QposSpec'-Ppos(202,:);
PropVectorSpec(203,:)=QposSpec'-Ppos(203,:);


PropogationDistance(201)=sqrt(PropVector(201,1)^2+PropVector(201,2)^2+...
    PropVector(201,3)^2);
PropogationDistance(202)=sqrt(PropVector(202,1)^2+PropVector(202,2)^2+...
    PropVector(202,3)^2);
PropogationDistance(203)=sqrt(PropVector(203,1)^2+PropVector(203,2)^2+...
    PropVector(203,3)^2);

PropogationDistanceSpec(201)=sqrt(PropVectorSpec(201,1)^2+...
    PropVectorSpec(201,2)^2+...
    PropVectorSpec(201,3)^2);
PropogationDistanceSpec(202)=sqrt(PropVectorSpec(202,1)^2+...
    PropVectorSpec(202,2)^2+...
    PropVectorSpec(202,3)^2);
PropogationDistanceSpec(203)=sqrt(PropVectorSpec(203,1)^2+...
    PropVectorSpec(203,2)^2+...
    PropVectorSpec(203,3)^2);

PropogationTime(201)=PropogationDistance(201)/343;
PropogationTime(202)=PropogationDistance(202)/343;
PropogationTime(203)=PropogationDistance(203)/343;

PropogationTimeSpec(201)=PropogationDistanceSpec(201)/343;
PropogationTimeSpec(202)=PropogationDistanceSpec(202)/343;
PropogationTimeSpec(203)=PropogationDistanceSpec(203)/343;
```

BTM Validation Case Sampled at 110Mhz

```
cd('/Users/mandalin/Documents/MATLAB/BTM Confirmation')
```

```
%Define Geometrical Properties
theta_omega=270*(pi/180);
theta=225*(pi/180);
theta_o=45*(pi/180);
r=100;
ro=100;
Z=0;
epsilon=[.1,.5,1,10]*(pi/180); %penetration into the shadow zone
outputFS=110000;
calcFS=110000*1000;
[Output] = BTMFuncValidate(theta_omega,theta,theta_o,r,ro,Z,epsilon,...
    calcFS,calcFS)
```

Prepare Figures

```
figure(4)
title({'Power Spectral Density of the Diffracted Impulse Response';...
    'Divided by the PSD of FreeField IR';...
    'Free Field impulse as Dirac delta';'fs=110MHz'}, 'FontSize',15)
AX=legend('e=.1ą', 'e=.5ą ','e=1ą', 'e=10ą')
set(AX,'FontSize',16)

figure(3)
title('Fig. 2  Medwin 1982 Rep.','FontSize',16)
AX=legend('e=.1ą', 'e=.5ą ','e=1ą', 'e=10ą')
set(AX,'FontSize',16)
ylim([.1,5])
xlim([.99,5]*1000)
```

Store Figures

```
figure(4)
cd('/Users/mandalin/Desktop/Dissertation/LindDissertationDocument/',...
    'LindDissertation/Chapter-4/Figures/FreqContent')
filename=strcat('3.eps')
%%%print(filename,'-depsc')
cd('/Users/mandalin/Documents/MATLAB/BTM Confirmation')

figure(3)
cd('/Users/mandalin/Desktop/Dissertation/LindDissertationDocument/',...
```

```
    'LindDissertation/Chapter-4/Figures/FreqContent')
filename=strcat('3time.eps')
%%%print(filename,'-depsc')
cd('/Users/mandalin/Documents/MATLAB/BTM Confirmation')
```

Validation for Downsampling to 110Hz to reproduce figure : Via Averaging

```
%Matches Perfectly
%---------------------------------------------------------------Time Domain
cd('/Users/mandalin/Documents/MATLAB/BTM Confirmation')
ratio = calcFS/outputFS;
inds=[1:floor(length(Output.IR(1,:))/ratio)]*ratio-ratio;
    %use this one with averaging


    figure()
for i=1:4
    for(l=1:length(inds))
        if (l==1)
            IR(i,l)=mean(Output.IR(i,1:ratio/2))/2;
        else
            IR(i,l)=mean(Output.IR(i,inds(l)-ratio/2:inds(l)+ratio/2));
        end
    end
        plot(IR(i,:))
    hold on
end

set(gca,'XScale','log')
set(gca,'YScale','log')
AX=legend('e=.1ą', 'e=.5ą ','e=1ą', 'e=10ą')
set(AX,'FontSize',16)
%ylim([.1,5])
xlim([.99,5])
%axis tight
title('Fig. 2  Medwin 1982 Rep.','FontSize',16)
xlabel('n','FontSize', 16)
ylabel('p(n $\Delta$ t)','Interpreter','latex','FontSize',16)
```

```
%---------------------------------------------------------------Freq Domain
delta_t=1/outputFS;
R=ro+r;
rho=1.2;
S=1;
freefield=zeros(size(IR(i,:)));
%freefield(round((R/c)/delta_t))=(rho*S)/(4*pi*(ro+r)); //for phase
freefield(1)=(rho*S)/(4*pi*(ro+r)*delta_t);
%freefield(1)=Output.freefield(1)/ratio; %this line and the one above are
%equivalent


[f,N,delta_f,delta_t,X,Gxx,Xrms]=Lind_PSD(freefield,outputFS);
Freefield=abs(Gxx);

figure()
for i=1:length(epsilon)
    x=IR(i,:);
    [f,N,delta_f,delta_t,X,Gxx,Xrms]=Lind_PSD(x,outputFS);
    P(i,:)=abs(Gxx);

    TransferFunc(i,:)=P(i,:)./Freefield;
    semilogx(f,10*log10(TransferFunc(i,:)))
    hold on
end

title({'Power Spectral Density of the Diffracted Impulse Response';...
    'Divided by the PSD of FreeField IR';...
    'Free Field impulse as Dirac delta';'fs=110MHz'}, 'FontSize',15)
AX=legend('e=.1ą', 'e=.5ą ','e=1ą', 'e=10ą')
set(AX,'FontSize',16)
cd(['/Users/mandalin/Desktop/Dissertation/LindDissertationDocument/',...
    'LindDissertation/Chapter-4/Figures/FreqContent'])
% %% Validation for Downsampling to 110Hz to reproduce figure : Via LPF
% clear IR
% %--------------------------------------------------------------Time Domain
% cd('/Users/mandalin/Documents/MATLAB/BTM Confirmation')
% %Lowpass Filter before Downsampling
% fc = outputFS*(1/1.2);
```

```
% [b,a] = butter(2,fc/(calcFS/2));
% %freqz(b,a)
%
% inds=[1:floor(length(Output.IR(1,:))/ratio)]*ratio-ratio/2;
%     %use this one without averaging
%     %Significantly different spectra without the ratio/2 term.
%
% clear Output.IR_LPF;
% clear IR;
%
% figure(5)
% for(i=1:4)
%     Output.IR_LPF(i,:) = filter(b,a,Output.IR(i,:));
%     IR(i,:)=Output.IR_LPF(i,inds);
%     %IR(i,:)=downsample(Output.IR_LPF(i,:),ratio) %also bad
%     %IR(i,:)=decimate(Output.IR_LPF(i,:),ratio); %bad
%     plot(IR(i,:))
%     hold on
% end
%
%
% set(gca,’XScale’,’log’)
% set(gca,’YScale’,’log’)
% AX=legend(’e=.1ą’, ’e=.5ą ’,’e=1ą’, ’e=10ą’)
% set(AX,’FontSize’,16)
% %ylim([.1,5])
% xlim([.99,5])
% %axis tight
% title(’Fig. 2  Medwin 1982 Rep.’,’FontSize’,16)
% xlabel(’n’,’FontSize’, 16)
% ylabel(’p(n $\Delta$ t)’,’Interpreter’,’latex’,’FontSize’,16)
%
% %------------------------------------------------------------Freq Domain
% delta_t=1/outputFS;
% R=ro+r;
% rho=1.2;
% S=1;
% freefield=zeros(size(IR(i,:)));
% %freefield(round((R/c)/delta_t))=(rho*S)/(4*pi*(ro+r)); //for phase
% freefield(1)=(rho*S)/(4*pi*(ro+r)*delta_t);
```

```
%
% [f,N,delta_f,delta_t,X,Gxx,Xrms]=Lind_PSD(freefield,outputFS);
% Freefield=abs(Gxx);
%
% figure()
% for i=1:length(epsilon)
%     x=IR(i,:);
%     [f,N,delta_f,delta_t,X,Gxx,Xrms]=Lind_PSD(x,outputFS);
%     P(i,:)=abs(Gxx);
%
%     TransferFunc(i,:)=P(i,:)./Freefield;
%     semilogx(f,10*log10(TransferFunc(i,:)))
%     hold on
% end
%
% title({'Power Spectral Density of the Diffracted Impulse Response';...
%     'Divided by the PSD of FreeField IR';...
%     'Free Field impulse as Dirac delta';'fs=110MHz'}, 'FontSize',15)
% AX=legend('e=.1ą', 'e=.5ą ','e=1ą', 'e=10ą')
% set(AX,'FontSize',16)
% cd(['/Users/mandalin/Desktop/Dissertation/LindDissertationDocument/',...
%     'LindDissertation/Chapter-4/Figures/FreqContent'])
```

Microphone 201 Case Incident

```
close all
cd('/Users/mandalin/Documents/MATLAB/BTM Confirmation')

%Define Physical Properties
c=343;
rho=1.2;

%Define Geometrical Properties
theta_omega=270*(pi/180);
theta_o=4.3476015612207322;
theta=1.5721641012842373;
ro=31104.948265573679;
r=2.3212898140096589;
Z=-7681.3138268098464;
epsilon=0;
```

```
outputFS=48000;
calcFS=120000*1000;

[Output] = BTMFuncValidate(theta_omega,theta,theta_o,r,ro,Z,epsilon,...
    calcFS,calcFS)
%%------------------------------------------Prepare Transfer Function Figure
figure(4)
title({'Transfer Function, Diffracted Contribution re. Free Field',...
    'Mic 201'},'FontSize',16)
%%---------------------------------------------Store Transfer Function Figure
cd(['/Users/mandalin/Desktop/Dissertation/LindDissertationDocument/',...
    'LindDissertation/Chapter-6/Figures'])
filename=strcat('BTMTF_Mic201.eps')
%%%print(filename,'-depsc')
cd('/Users/mandalin/Documents/MATLAB/BTM Confirmation')
%%-----------------------------------------------------------------Downsample
clear IR
ratio = calcFS/outputFS;
inds=[1:floor(length(Output.IR(1,:))/ratio)]*ratio-ratio;
    %use this version if inds one with averaging

for(l=1:length(inds))
    if (l==1)
        IR(l)=mean(Output.IR(1,1:ratio/2))/2;
    else
        IR(l)=mean(Output.IR(1,inds(l)-ratio/2:inds(l)+ratio/2));
    end
end

%%--------------------------------------------------------Scale by Free Field
figure(3)
IR_Scaled=ratio*IR/Output.freefield(1);
 %changed sampling rate so we need to scale by ratio!


%%----------------------------------------------------------Prepare IR Figure
figure()
plot(IR_Scaled,'LineWidth',2);
    %As expected, this one acts like a plane wave, independent of ro
```

```
title('Scaled by Freefield, and delta t','FontSize',16)
set(gca,'XScale','log')
set(gca,'YScale','log')
%ylim([.1,5])
%xlim([.99,5])
%axis tight
xlabel('n, sample index','FontSize', 16)
ylabel({'p(n $\Delta$ t)','Amplitude in [Pa]',...
    'Assuming Free-Field impulse is a Kronecker Delta',...
    'downsampled to fs=48Hz'},'Interpreter','latex','FontSize',16)
title('Simulated Diffracted Impulse Response at Mic 201')

%%-----------------------------------------------------------Store IR Figure
cd(['/Users/mandalin/Desktop/Dissertation/LindDissertationDocument/',...
    'LindDissertation/Chapter-4/Figures'])
filename=strcat('BTMIR_Mic201.eps')
%%%print(filename,'-depsc')
cd('/Users/mandalin/Documents/MATLAB/BTM Confirmation')


cd(['/Users/mandalin/Desktop/Dissertation/LindDissertationDocument/',...
    'LindDissertation/Chapter-4/Figures'])
filename=strcat('BTMIR_Mic201.eps')
print(filename,'-depsc')

%%--------------------------------------------------------------Convolution
figure()
FS=outputFS;
Y=conv(IR_Scaled,input); %input here is already divided by 2
Y=Y*2; %doubled to account for ground.


%%---------------------------------------------------------Calculate Metrics
cd(PLdBCalcFolder)
PLdBofY=PLdB(double(Y),FS);
PmaxofY=max(abs(Y))

%%----------------------------------------------------------------Time Aling
t=([1:length(Y)]-1)/outputFS;
onset_ind=find(input>.5,1,'first');
```

```
onset_time_input=t(onset_ind);
    %t_input=([1:length(input)]-1)/outputFS;
    %plot(t_input-onset_time_input,input)


%%------------------------------------------------Prepare Waveform Figure
figure(5)
time_aligned_time_201=t-onset_time_input+Output.tau_o-PropogationTime(201);
Y_201=Y;
plot(t-onset_time_input+Output.tau_o-PropogationTime(201),Y,'LineWidth',2);
delay_between_incident_and_diffracted=Output.tau_o-PropogationTime(201);
%tau_o is the least time path delay
%propagation time is the time from the source to the receiver
xlabel('Time [s]','FontSize',16);
ylabel('Pressure [Pa]','FontSize',16);
axis tight
ylim([min(Y)*1.1,max(Y)*1.1])
xlim([0,.2])
title({'Simulated Waveform - Mic 201';'Doubled to Account for Ground';...
    'Pmax = 9.69 Pa, PLdB = 74.5' },'FontSize',16);

%%--------------------------------------------------Store Waveform Figure
cd(['/Users/mandalin/Desktop/Dissertation/LindDissertationDocument/',...
    'LindDissertation/Chapter-4/Figures'])
filename=strcat('BTMWaveform_Mic201.eps')
print(filename,'-depsc')
cd('/Users/mandalin/Documents/MATLAB/BTM Confirmation')
save('simulated_diffracted_outputs_201.mat','Y_201',...
    'time_aligned_time_201','IR_Scaled',...
    'delay_between_incident_and_diffracted')
```

Microphone 201 Case Ground Reflection

```
close all
cd('/Users/mandalin/Documents/MATLAB/BTM Confirmation')

%Define Physical Properties
c=343;
rho=1.2;
```

```
%Define Geometrical Properties
theta_omega=270*(pi/180);
theta_o=5.07717639954864718987;
theta=1.5721641012842373;
ro=31104.948265573679;
r=2.3212898140096589;
Z=-7681.3138268098464;
epsilon=0;

outputFS=48000;
calcFS=120000*1000;
[Output] = BTMFuncValidate(theta_omega,theta,theta_o,r,ro,Z,epsilon,...
    calcFS,calcFS)
%%-----------------------------------------Prepare Transfer Function Figure
figure(4)
title({'Transfer Function, Diffracted Contribution re. Free Field',...
    'Mic 201'},'FontSize',16)
%%-------------------------------------------Store Transfer Function Figure
cd(['/Users/mandalin/Desktop/Dissertation/LindDissertationDocument/',...
    'LindDissertation/Chapter-6/Figures'])
filename=strcat('BTMTF_Mic201.eps')
%%%print(filename,'-depsc')
cd('/Users/mandalin/Documents/MATLAB/BTM Confirmation')
%%---------------------------------------------------------------Downsample
clear IR
ratio = calcFS/outputFS;
inds=[1:floor(length(Output.IR(1,:))/ratio)]*ratio-ratio;
    %use this version if inds one with averaging

for(l=1:length(inds))
    if (l==1)
        IR(l)=mean(Output.IR(1,1:ratio/2))/2;
    else
        IR(l)=mean(Output.IR(1,inds(l)-ratio/2:inds(l)+ratio/2));
    end
end

%%-------------------------------------------------------Scale by Free Field
figure(3)
IR_Scaled=ratio*IR/Output.freefield(1);
```

```
    %changed sampling rate...we need to scale by ratio!


%%-------------------------------------------------------Prepare IR Figure
figure()
plot(IR_Scaled,'LineWidth',2);
    %As expected, this one acts like a plane wave, independent of ro
title('Scaled by Freefield, and delta t','FontSize',16)
set(gca,'XScale','log')
set(gca,'YScale','log')
%ylim([.1,5])
%xlim([.99,5])
%axis tight
xlabel('n, sample index','FontSize', 16)
ylabel({'p(n $\Delta$ t)','Amplitude in [Pa]',...
    'Assuming Free-Field impulse is a Kronecker Delta',...
    'downsampled to fs=48Hz'},'Interpreter','latex','FontSize',16)
title({'Simulated Diffracted Impulse Response at Mic 201',...
    'Ground Reflected Source'})


cd(['/Users/mandalin/Desktop/Dissertation/LindDissertationDocument/',...
    'LindDissertation/Chapter-4/Figures'])
filename=strcat('BTMIR_Mic201_Spec.eps')
print(filename,'-depsc')


%%---------------------------------------------------------Store IR Figure
cd(['/Users/mandalin/Desktop/Dissertation/LindDissertationDocument/',...
    'LindDissertation/Chapter-4/Figures'])
filename=strcat('BTMIR_Mic201.eps')
%%%print(filename,'-depsc')
cd('/Users/mandalin/Documents/MATLAB/BTM Confirmation')


%%------------------------------------------------------------Convolution
figure()
FS=outputFS;
Y=conv(IR_Scaled,input); %input here is already divided by 2
Y=Y*2; %doubled to account for ground.
```

```
%%---------------------------------------------------------Calculate Metrics
cd(PLdBCalcFolder)
PLdBofY=PLdB(double(Y),FS);
PmaxofY=max(abs(Y))

%%----------------------------------------------------------------Time Aling
t=([1:length(Y)]-1)/outputFS;
onset_ind=find(input>.5,1,'first');
onset_time_input=t(onset_ind);
    %t_input=([1:length(input)]-1)/outputFS;
    %plot(t_input-onset_time_input,input)


%%---------------------------------------------------Prepare Waveform Figure
figure()
time_aligned_time_201=t-onset_time_input+Output.tau_o-...
    PropogationTimeSpec(201);
Y_201=Y;
plot(t-onset_time_input+Output.tau_o-...
    PropogationTimeSpec(201),Y,'LineWidth',2);
delay_between_incident_and_diffracted=Output.tau_o-...
    PropogationTimeSpec(201);
xlabel('Time [s]','FontSize',16);
ylabel('Pressure [Pa]','FontSize',16);
axis tight
ylim([min(Y)*1.1,max(Y)*1.1])
xlim([0,.2])
title({'Simulated Waveform - Mic 201 - Ground Reflected Source';...
    'Doubled to Account for Ground';...
    'Pmax = 9.69 Pa, PLdB = 74.5' },'FontSize',16);

%%-----------------------------------------------------Store Waveform Figure
cd(['/Users/mandalin/Desktop/Dissertation/LindDissertationDocument/',...
    'LindDissertation/Chapter-4/Figures'])
filename=strcat('BTMWaveform_Mic201_Spec.eps')
print(filename,'-depsc')
cd('/Users/mandalin/Documents/MATLAB/BTM Confirmation')
save('simulated_diffracted_outputs_201spec.mat','Y_201',...
```

```
    'time_aligned_time_201','IR_Scaled',...
    'delay_between_incident_and_diffracted')
```

Microphone 202 Case Incident

```
close all
cd('/Users/mandalin/Documents/MATLAB/BTM Confirmation')

%Define Physical Properties
c=343;
rho=1.2;

%Define Geometrical Properties
theta_omega=270*(pi/180);
theta_o=1.2060089;
theta=1.5694285523055558;
ro=31104.948;
r=2.321289;
Z=-7681.3;
epsilon=0;


outputFS=48000;
calcFS=120000*1000;
[Output] = BTMFuncValidate(theta_omega,theta,theta_o,r,ro,Z,epsilon,...
    calcFS,calcFS)
%%-------------------------------------------Prepare Transfer Function Figure
figure(4)
title({'Transfer Function, Diffracted Contribution re. Free Field',...
    'Mic 202'},'FontSize',16)
%%---------------------------------------------Store Transfer Function Figure
cd(['/Users/mandalin/Desktop/Dissertation/LindDissertationDocument/',...
    'LindDissertation/Chapter-6/Figures'])
filename=strcat('BTMTF_Mic202.eps')
%%%%print(filename,'-depsc')
cd('/Users/mandalin/Documents/MATLAB/BTM Confirmation')
%%-----------------------------------------------------------------Downsample
clear IR
ratio = calcFS/outputFS;
inds=[1:floor(length(Output.IR(1,:))/ratio)]*ratio-ratio;
```

```
    %use this version if inds one with averaging

for(l=1:length(inds))
    if (l==1)
        IR(l)=mean(Output.IR(1,1:ratio/2))/2;
    else
        IR(l)=mean(Output.IR(1,inds(l)-ratio/2:inds(l)+ratio/2));
    end
end

%%---------------------------------------------------------Scale by Free Field
figure(3)
IR_Scaled=ratio*IR/Output.freefield(1);
    %changed sampling rate...we need to scale by ratio!


%%-----------------------------------------------------------Prepare IR Figure
figure()
plot(IR_Scaled,'LineWidth',2);
    %As expected, this one acts like a plane wave, independent of ro
title('Scaled by Freefield, and delta t','FontSize',16)
set(gca,'XScale','log')
set(gca,'YScale','log')
%ylim([.1,5])
%xlim([.99,5])
%axis tight
xlabel('n, sample index','FontSize', 16)
ylabel({'p(n $\Delta$ t)','Amplitude in [Pa]',...
    'Assuming Free-Field impulse is a Kronecker Delta',...
    'downsampled to fs=48Hz'},'Interpreter','latex','FontSize',16)
title('Simulated Diffracted Impulse Response at Mic 202')


cd(['/Users/mandalin/Desktop/Dissertation/LindDissertationDocument/',...
    'LindDissertation/Chapter-4/Figures'])
filename=strcat('BTMIR_Mic202.eps')
print(filename,'-depsc')


%%----------------------------------------------------------------Convolution
```

```
figure()
FS=outputFS;
Y=conv(IR_Scaled,input); %input here is already divided by 2
Y=Y*2; %doubled to account for ground.


%%----------------------------------------------------------Calculate Metrics
cd(PLdBCalcFolder)
PLdBofY=PLdB(double(Y),FS);
PmaxofY=max(abs(Y))

%%-----------------------------------------------------------------Time Aling
t=([1:length(Y)]-1)/outputFS;
onset_ind=find(input>.5,1,'first');
onset_time_input=t(onset_ind);
    %t_input=([1:length(input)]-1)/outputFS;
    %plot(t_input-onset_time_input,input)


%%----------------------------------------------------Prepare Waveform Figure
figure()
time_aligned_time_202=t-onset_time_input+Output.tau_o-...
    PropogationTime(202);
Y_202=Y;
plot(t-onset_time_input+Output.tau_o-PropogationTime(202),Y,...
    'LineWidth',2);
delay_between_incident_and_diffracted=Output.tau_o-PropogationTime(202);
xlabel('Time [s]','FontSize',16);
ylabel('Pressure [Pa]','FontSize',16);
axis tight
ylim([min(Y)*1.1,max(Y)*1.1])
xlim([0,.2])
title({'Simulated Waveform - Mic 202';'Doubled to Account for Ground';...
    'Pmax = 32.01 Pa, PLdB = 89.2' },'FontSize',16);

%%------------------------------------------------------Store Waveform Figure
cd(['/Users/mandalin/Desktop/Dissertation/LindDissertationDocument/',...
    'LindDissertation/Chapter-4/Figures'])
filename=strcat('BTMWaveform_Mic202.eps')
print(filename,'-depsc')
```

```
cd('/Users/mandalin/Documents/MATLAB/BTM Confirmation')
save('simulated_diffracted_outputs_202.mat','Y_202',...
    'time_aligned_time_202','IR_Scaled',...
    'delay_between_incident_and_diffracted')
```

Microphone 202 Case Specular

```
close all
cd('/Users/mandalin/Documents/MATLAB/BTM Confirmation')

%Define Physical Properties
c=343;
rho=1.2;

%Define Geometrical Properties
theta_omega=270*(pi/180);
theta_o=1.93558374595885429592;
theta=1.5694285523055558;
ro=31104.948;
r=2.321289;
Z=-7681.3;
epsilon=0;


outputFS=48000;
calcFS=120000*1000;
[Output] = BTMFuncValidate(theta_omega,theta,theta_o,r,ro,Z,epsilon,...
    calcFS,calcFS)
%%-------------------------------------------Prepare Transfer Function Figure
figure(4)
title({'Transfer Function, Diffracted Contribution re. Free Field',...
    'Mic 202'},'FontSize',16)
%%---------------------------------------------Store Transfer Function Figure
cd(['/Users/mandalin/Desktop/Dissertation/LindDissertationDocument/',...
    'LindDissertation/Chapter-6/Figures'])
filename=strcat('BTMTF_Mic202.eps')
%%%%print(filename,'-depsc')
cd('/Users/mandalin/Documents/MATLAB/BTM Confirmation')
%%-----------------------------------------------------------------Downsample
clear IR
```

```
ratio = calcFS/outputFS;
inds=[1:floor(length(Output.IR(1,:))/ratio)]*ratio-ratio;
    %use this version if inds one with averaging

for(l=1:length(inds))
    if (l==1)
        IR(l)=mean(Output.IR(1,1:ratio/2))/2;
    else
        IR(l)=mean(Output.IR(1,inds(l)-ratio/2:inds(l)+ratio/2));
    end
end

%%--------------------------------------------------------Scale by Free Field
figure(3)
IR_Scaled=ratio*IR/Output.freefield(1);
    %changed sampling rate...we need to scale by ratio!


%%----------------------------------------------------------Prepare IR Figure
figure()
plot(IR_Scaled,'LineWidth',2);
    %As expected, this one acts like a plane wave, independent of ro
title('Scaled by Freefield, and delta t','FontSize',16)
set(gca,'XScale','log')
set(gca,'YScale','log')
%ylim([.1,5])
%xlim([.99,5])
%axis tight
xlabel('n, sample index','FontSize', 16)
ylabel({'p(n $\Delta$ t)','Amplitude in [Pa]',...
    'Assuming Free-Field impulse is a Kronecker Delta',...
    'downsampled to fs=48Hz'},'Interpreter','latex','FontSize',16)
title({'Simulated Diffracted Impulse Response at Mic 202',...
    'Ground Reflected Source'})

cd(['/Users/mandalin/Desktop/Dissertation/LindDissertationDocument/',...
    'LindDissertation/Chapter-4/Figures'])
filename=strcat('BTMIR_Mic202_Spec.eps')
print(filename,'-depsc')
```

```
%%------------------------------------------------------------Convolution
figure()
FS=outputFS;
Y=conv(IR_Scaled,input); %input here is already divided by 2
Y=Y*2; %doubled to account for ground.


%%-------------------------------------------------------Calculate Metrics
cd(PLdBCalcFolder)
PLdBofY=PLdB(double(Y),FS);
PmaxofY=max(abs(Y))

%%--------------------------------------------------------------Time Aling
t=([1:length(Y)]-1)/outputFS;
onset_ind=find(input>.5,1,'first');
onset_time_input=t(onset_ind);
    %t_input=([1:length(input)]-1)/outputFS;
    %plot(t_input-onset_time_input,input)


%%-------------------------------------------------Prepare Waveform Figure
figure()
time_aligned_time_202=t-onset_time_input+Output.tau_o-...
    PropogationTimeSpec(202);
Y_202=Y;
plot(t-onset_time_input+Output.tau_o-PropogationTimeSpec(202),Y,...
    'LineWidth',2);
delay_between_incident_and_diffracted=Output.tau_o-PropogationTimeSpec(202);
xlabel('Time [s]','FontSize',16);
ylabel('Pressure [Pa]','FontSize',16);
axis tight
ylim([min(Y)*1.1,max(Y)*1.1])
xlim([0,.2])
title({'Simulated Waveform - Mic 202 - Ground Reflected Source';...
    'Doubled to Account for Ground';...
    'Pmax = 23.16 Pa, PLdB = 87.0' },'FontSize',16);

%%---------------------------------------------------Store Waveform Figure
cd(['/Users/mandalin/Desktop/Dissertation/LindDissertationDocument/',...
    'LindDissertation/Chapter-4/Figures'])
```

```
filename=strcat('BTMWaveform_Mic202_Spec.eps')
print(filename,'-depsc')
cd('/Users/mandalin/Documents/MATLAB/BTM Confirmation')
save('simulated_diffracted_outputs_202_spec.mat','Y_202',...
    'time_aligned_time_202','IR_Scaled',...
    'delay_between_incident_and_diffracted')
```

Microphone 203 Case Incident - Edge 1

```
close all
cd('/Users/mandalin/Documents/MATLAB/BTM Confirmation')

%Define Physical Properties
c=343;
rho=1.2;

%Define Geometrical Properties
theta_omega=4.7123889803846897;
theta=5.1183766301589069;
theta_o=1.2060089076309388;
r=2.3234080766462446;
ro=31104.948265573679;
Z=-7681.3138268098473;
epsilon=0;

outputFS=48000;
calcFS=120000*1000;
[Output] = BTMFuncValidate(theta_omega,theta,theta_o,r,ro,Z,epsilon,...
    calcFS,calcFS)
%%----------------------------------------Prepare Transfer Function Figure
figure(4)
title({'Transfer Function, Diffracted Contribution re. Free Field',...
    'Mic 203'},'FontSize',16)
%%------------------------------------------Store Transfer Function Figure
cd(['/Users/mandalin/Desktop/Dissertation/LindDissertationDocument/',...
    'LindDissertation/Chapter-6/Figures'])
filename=strcat('BTMTF_Mic203.eps')
%%%%print(filename,'-depsc')
cd('/Users/mandalin/Documents/MATLAB/BTM Confirmation')
%%------------------------------------------------------------Downsample
```

```
clear IR
ratio = calcFS/outputFS;
inds=[1:floor(length(Output.IR(1,:))/ratio)]*ratio-ratio;
    %use this version if inds one with averaging

for(l=1:length(inds))
    if (l==1)
        IR(l)=mean(Output.IR(1,1:ratio/2))/2;
    else
        IR(l)=mean(Output.IR(1,inds(l)-ratio/2:inds(l)+ratio/2));
    end
end

%%-------------------------------------------------------Scale by Free Field
figure(3)
IR_Scaled=ratio*IR/Output.freefield(1);
    %changed sampling rate...we need to scale by ratio!


%%---------------------------------------------------------Prepare IR Figure
figure()
plot(IR_Scaled,'LineWidth',2);
    %As expected, this one acts like a plane wave, independent of ro
title('Scaled by Freefield, and delta t','FontSize',16)
set(gca,'XScale','log')
set(gca,'YScale','log')
%ylim([.1,5])
%xlim([.99,5])
%axis tight
xlabel('n, sample index','FontSize', 16)
ylabel({'p(n $\Delta$ t)','Amplitude in [Pa]',...
    'Assuming Free-Field impulse is a Kronecker Delta',...
    'downsampled to fs=48Hz'},'Interpreter','latex','FontSize',16)
title({'Simulated Diffracted Impulse Response at Mic 203','Edge1'})

cd(['/Users/mandalin/Desktop/Dissertation/LindDissertationDocument/',...
    'LindDissertation/Chapter-4/Figures'])
filename=strcat('BTMIR_Mic203_Edge1.eps')
print(filename,'-depsc')
%%--------------------------------------------------------------Convolution
```

```
figure()
FS=outputFS;
Y=conv(IR_Scaled,input); %input here is already divided by 2
%Y=Y*2; %doubled to account for ground.


%%---------------------------------------------------------Calculate Metrics
cd(PLdBCalcFolder)
PLdBofY=PLdB(double(Y),FS);
PmaxofY=max(abs(Y))

%%----------------------------------------------------------------Time Aling
t=([1:length(Y)]-1)/outputFS;
onset_ind=find(input>.5,1,'first');
onset_time_input=t(onset_ind);
    %t_input=([1:length(input)]-1)/outputFS;
    %plot(t_input-onset_time_input,input)


%%---------------------------------------------------Prepare Waveform Figure
figure()
time_aligned_time_203=t-onset_time_input+Output.tau_o-...
    PropogationTime(203);
Y_203=Y;
plot(t-onset_time_input+Output.tau_o-PropogationTime(203),Y,...
    'LineWidth',2);
delay_between_incident_and_diffracted=Output.tau_o-PropogationTime(203);
xlabel('Time [s]','FontSize',16);
ylabel('Pressure [Pa]','FontSize',16);
axis tight
ylim([min(Y)*1.1,max(Y)*1.1])
xlim([0,.2])
title({'Simulated Waveform - Mic 203 - Edge 1';...
    'Pmax = 5.67 Pa, PLdB = 80.1' },'FontSize',16);

%%-----------------------------------------------------Store Waveform Figure
cd(['/Users/mandalin/Desktop/Dissertation/LindDissertationDocument/',...
    'LindDissertation/Chapter-4/Figures'])
filename=strcat('BTMWaveform_Mic203_Edge1.eps')
print(filename,'-depsc')
```

```
cd('/Users/mandalin/Documents/MATLAB/BTM Confirmation')
save('simulated_diffracted_outputs_203_Edge1.mat','Y_203',...
    'time_aligned_time_203','IR_Scaled',...
    'delay_between_incident_and_diffracted')
```

Microphone 203 Case Specular - Edge 1

```
close all
cd('/Users/mandalin/Documents/MATLAB/BTM Confirmation')

%Define Physical Properties
c=343;
rho=1.2;

%Define Geometrical Properties
theta_omega=4.7123889803846897;
theta=5.1183766301589069;
theta_o=1.93558374595885429592;
r=2.3234080766462446;
ro=31104.948265573679;
Z=-7681.3138268098473;
epsilon=0;

outputFS=48000;
calcFS=120000*1000;
[Output] = BTMFuncValidate(theta_omega,theta,theta_o,r,ro,Z,epsilon,...
    calcFS,calcFS)
%%-----------------------------------------Prepare Transfer Function Figure
figure(4)
title({'Transfer Function, Diffracted Contribution re. Free Field',...
    'Mic 203'},'FontSize',16)
%%-------------------------------------------Store Transfer Function Figure
cd(['/Users/mandalin/Desktop/Dissertation/LindDissertationDocument/',...
    'LindDissertation/Chapter-6/Figures'])
filename=strcat('BTMTF_Mic203.eps')
%%%%print(filename,'-depsc')
cd('/Users/mandalin/Documents/MATLAB/BTM Confirmation')
%%-----------------------------------------------------------------Downsample
clear IR
ratio = calcFS/outputFS;
```

```
inds=[1:floor(length(Output.IR(1,:))/ratio)]*ratio-ratio;
    %use this version if inds one with averaging

for(l=1:length(inds))
    if (l==1)
        IR(l)=mean(Output.IR(1,1:ratio/2))/2;
    else
        IR(l)=mean(Output.IR(1,inds(l)-ratio/2:inds(l)+ratio/2));
    end
end

%%-------------------------------------------------------Scale by Free Field
figure(3)
IR_Scaled=ratio*IR/Output.freefield(1);
    %changed sampling rate...we need to scale by ratio!


%%---------------------------------------------------------Prepare IR Figure
figure()
plot(IR_Scaled,'LineWidth',2);
    %As expected, this one acts like a plane wave, independent of ro
title('Scaled by Freefield, and delta t','FontSize',16)
set(gca,'XScale','log')
set(gca,'YScale','log')
%ylim([.1,5])
%xlim([.99,5])
%axis tight
xlabel('n, sample index','FontSize', 16)
ylabel({'p(n $\Delta$ t)','Amplitude in [Pa]',...
    'Assuming Free-Field impulse is a Kronecker Delta',...
    'downsampled to fs=48Hz'},'Interpreter','latex','FontSize',16)
title({'Simulated Diffracted Impulse Response at Mic 203',...
    'Edge1, Ground Reflected Source'})

cd(['/Users/mandalin/Desktop/Dissertation/LindDissertationDocument/',...
    'LindDissertation/Chapter-4/Figures'])
filename=strcat('BTMIR_Mic203_Edge1_Spec.eps')
print(filename,'-depsc')

%%--------------------------------------------------------------Convolution
```

```
figure()
FS=outputFS;
Y=conv(IR_Scaled,input); %input here is already divided by 2
%Y=Y*2; %doubled to account for ground.


%%----------------------------------------------------------Calculate Metrics
cd(PLdBCalcFolder)
PLdBofY=PLdB(double(Y),FS);
PmaxofY=max(abs(Y))

%%-----------------------------------------------------------------Time Aling
t=([1:length(Y)]-1)/outputFS;
onset_ind=find(input>.5,1,'first');
onset_time_input=t(onset_ind);
    %t_input=([1:length(input)]-1)/outputFS;
    %plot(t_input-onset_time_input,input)


%%---------------------------------------------------Prepare Waveform Figure
figure()
time_aligned_time_203=t-onset_time_input+Output.tau_o-...
    PropogationTimeSpec(203);
Y_203=Y;
plot(t-onset_time_input+Output.tau_o-PropogationTimeSpec(203),Y,...
    'LineWidth',2);
delay_between_incident_and_diffracted=Output.tau_o...
    -PropogationTimeSpec(203);
xlabel('Time [s]','FontSize',16);
ylabel('Pressure [Pa]','FontSize',16);
axis tight
ylim([min(Y)*1.1,max(Y)*1.1])
xlim([0,.2])
title({'Simulated Waveform - Mic 203 - Edge1 - Ground Reflected Source';...
    'Pmax = 10.27 Pa, PLdB = 82.0' },'FontSize',16);

%%-----------------------------------------------------Store Waveform Figure
cd(['/Users/mandalin/Desktop/Dissertation/LindDissertationDocument/',...
    'LindDissertation/Chapter-4/Figures'])
filename=strcat('BTMWaveform_Mic203_Edge1_Spec.eps')
```

```
print(filename,'-depsc')
cd('/Users/mandalin/Documents/MATLAB/BTM Confirmation')
save('simulated_diffracted_outputs_203_Edge1_Spec.mat','Y_203',...
    'time_aligned_time_203','IR_Scaled',...
    'delay_between_incident_and_diffracted')
```

Microphone 203 Case Incident - Edge 2

```
close all
cd('/Users/mandalin/Documents/MATLAB/BTM Confirmation')

%Define Physical Properties
c=343;
rho=1.2;

%Define Geometrical Properties
theta_omega=4.7123889803846897;
theta=4.3064013306104725;
theta_o=4.34760156122073215812;
r=2.3234080766462446;
ro=31104.948265573679;
Z=-7681.3138268098473;
epsilon=0;

outputFS=48000;
calcFS=120000*1000;
[Output] = BTMFuncValidate(theta_omega,theta,theta_o,r,ro,Z,epsilon,...
    calcFS,calcFS)
%%-------------------------------------------Prepare Transfer Function Figure
figure(4)
title({'Transfer Function, Diffracted Contribution re. Free Field',...
    'Mic 203'},'FontSize',16)
%%---------------------------------------------Store Transfer Function Figure
cd(['/Users/mandalin/Desktop/Dissertation/LindDissertationDocument/',...
    'LindDissertation/Chapter-6/Figures'])
filename=strcat('BTMTF_Mic203.eps')
%%%%print(filename,'-depsc')
cd('/Users/mandalin/Documents/MATLAB/BTM Confirmation')
%%----------------------------------------------------------------Downsample
clear IR
```

```
ratio = calcFS/outputFS;
inds=[1:floor(length(Output.IR(1,:))/ratio)]*ratio-ratio;
    %use this version if inds one with averaging

for(l=1:length(inds))
    if (l==1)
        IR(l)=mean(Output.IR(1,1:ratio/2))/2;
    else
        IR(l)=mean(Output.IR(1,inds(l)-ratio/2:inds(l)+ratio/2));
    end
end

%%--------------------------------------------------------Scale by Free Field
figure(3)
IR_Scaled=ratio*IR/Output.freefield(1);
    %changed sampling rate...we need to scale by ratio!


%%---------------------------------------------------------Prepare IR Figure
figure()
plot(IR_Scaled,'LineWidth',2);
    %As expected, this one acts like a plane wave, independent of ro
title('Scaled by Freefield, and delta t','FontSize',16)
set(gca,'XScale','log')
set(gca,'YScale','log')
%ylim([.1,5])
%xlim([.99,5])
%axis tight
xlabel('n, sample index','FontSize', 16)
ylabel({'p(n $\Delta$ t)','Amplitude in [Pa]',...
    'Assuming Free-Field impulse is a Kronecker Delta',...
    'downsampled to fs=48Hz'},'Interpreter','latex','FontSize',16)
title({'Simulated Diffracted Impulse Response at Mic 203','Edge 2'})

cd(['/Users/mandalin/Desktop/Dissertation/LindDissertationDocument/',...
    'LindDissertation/Chapter-4/Figures'])
filename=strcat('BTMIR_Mic203_Edge2.eps')
print(filename,'-depsc')

%%---------------------------------------------------------------Convolution
```

```
figure()
FS=outputFS;
Y=conv(IR_Scaled,input); %input here is already divided by 2
%Y=Y*2; %doubled to account for ground.


%%----------------------------------------------------------Calculate Metrics
cd(PLdBCalcFolder)
PLdBofY=PLdB(double(Y),FS);
PmaxofY=max(abs(Y))

%%-----------------------------------------------------------------Time Aling
t=([1:length(Y)]-1)/outputFS;
onset_ind=find(input>.5,1,'first');
onset_time_input=t(onset_ind);
    %t_input=([1:length(input)]-1)/outputFS;
    %plot(t_input-onset_time_input,input)


%%---------------------------------------------------Prepare Waveform Figure
figure()
time_aligned_time_203=t-onset_time_input+Output.tau_o-...
    PropogationTime(203);
Y_203=Y;
plot(t-onset_time_input+Output.tau_o-PropogationTime(203),Y,...
    'LineWidth',2);
delay_between_incident_and_diffracted=Output.tau_o-PropogationTime(203);
xlabel('Time [s]','FontSize',16);
ylabel('Pressure [Pa]','FontSize',16);
axis tight
ylim([min(Y)*1.1,max(Y)*1.1])
xlim([0,.2])
title({'Simulated Waveform - Mic 203 - Edge2';...
    'Pmax = 9.84 Pa, PLdB = 74.6' },'FontSize',16);

%%-----------------------------------------------------Store Waveform Figure
cd(['/Users/mandalin/Desktop/Dissertation/LindDissertationDocument/',...
    'LindDissertation/Chapter-4/Figures'])
filename=strcat('BTMWaveform_Mic203_Edge2.eps')
print(filename,'-depsc')
```

```
cd('/Users/mandalin/Documents/MATLAB/BTM Confirmation')
save('simulated_diffracted_outputs_203_Edge2.mat','Y_203',...
    'time_aligned_time_203','IR_Scaled',...
    'delay_between_incident_and_diffracted')
```

Microphone 203 Case Specular - Edge 2

```
close all
cd('/Users/mandalin/Documents/MATLAB/BTM Confirmation')

%Define Physical Properties
c=343;
rho=1.2;

%Define Geometrical Properties
theta_omega=4.7123889803846897;
theta=4.3064013306104725;
theta_o=5.07717639954864718987;
r=2.3234080766462446;
ro=31104.948265573679;
Z=-7681.3138268098473;
epsilon=0;

outputFS=48000;
calcFS=120000*1000;
[Output] = BTMFuncValidate(theta_omega,theta,theta_o,r,ro,Z,epsilon,...
    calcFS,calcFS)
%%-----------------------------------------Prepare Transfer Function Figure
figure(4)
title({'Transfer Function, Diffracted Contribution re. Free Field',...
    'Mic 203'},'FontSize',16)
%%-------------------------------------------Store Transfer Function Figure
cd(['/Users/mandalin/Desktop/Dissertation/LindDissertationDocument/',...
    'LindDissertation/Chapter-6/Figures'])
filename=strcat('BTMTF_Mic203.eps')
%%%%print(filename,'-depsc')
cd('/Users/mandalin/Documents/MATLAB/BTM Confirmation')
%%---------------------------------------------------------------Downsample
clear IR
ratio = calcFS/outputFS;
```

```
inds=[1:floor(length(Output.IR(1,:))/ratio)]*ratio-ratio;
    %use this version if inds one with averaging

for(l=1:length(inds))
    if (l==1)
        IR(l)=mean(Output.IR(1,1:ratio/2))/2;
    else
        IR(l)=mean(Output.IR(1,inds(l)-ratio/2:inds(l)+ratio/2));
    end
end

%%-------------------------------------------------------Scale by Free Field
figure(3)
IR_Scaled=ratio*IR/Output.freefield(1);
    %changed sampling rate...we need to scale by ratio!


%%---------------------------------------------------------Prepare IR Figure
figure()
plot(IR_Scaled,'LineWidth',2);
    %As expected, this one acts like a plane wave, independent of ro
title('Scaled by Freefield, and delta t','FontSize',16)
set(gca,'XScale','log')
set(gca,'YScale','log')
%ylim([.1,5])
%xlim([.99,5])
%axis tight
xlabel('n, sample index','FontSize', 16)
ylabel({'p(n $\Delta$ t)','Amplitude in [Pa]',...
    'Assuming Free-Field impulse is a Kronecker Delta',...
    'downsampled to fs=48Hz'},'Interpreter','latex','FontSize',16)
title({'Simulated Diffracted Impulse Response at Mic 203',...
    'Edge 2, Ground Reflected Source'})

cd(['/Users/mandalin/Desktop/Dissertation/LindDissertationDocument/',...
    'LindDissertation/Chapter-4/Figures'])
filename=strcat('BTMIR_Mic203_Edge2_Spec.eps')
print(filename,'-depsc')

cd('/Users/mandalin/Documents/MATLAB/BTM Confirmation')
```

```
%%--------------------------------------------------------------Convolution
figure()
FS=outputFS;
Y=conv(IR_Scaled,input); %input here is already divided by 2
%Y=Y*2; %doubled to account for ground.


%%---------------------------------------------------------Calculate Metrics
cd(PLdBCalcFolder)
PLdBofY=PLdB(double(Y),FS);
PmaxofY=max(abs(Y))

%%----------------------------------------------------------------Time Aling
t=([1:length(Y)]-1)/outputFS;
onset_ind=find(input>.5,1,'first');
onset_time_input=t(onset_ind);
    %t_input=([1:length(input)]-1)/outputFS;
    %plot(t_input-onset_time_input,input)


%%---------------------------------------------------Prepare Waveform Figure
figure()
time_aligned_time_203=t-onset_time_input+Output.tau_o-...
    PropogationTimeSpec(203);
Y_203=Y;
plot(t-onset_time_input+Output.tau_o-PropogationTimeSpec(203),Y,...
    'LineWidth',2);
delay_between_incident_and_diffracted=Output.tau_o-...
    PropogationTimeSpec(203);
xlabel('Time [s]','FontSize',16);
ylabel('Pressure [Pa]','FontSize',16);
axis tight
ylim([min(Y)*1.1,max(Y)*1.1])
xlim([0,.2])
title({'Simulated Waveform - Mic 203 - Edge2 - Ground Reflected Source';...
    'Pmax = 9.84 Pa, PLdB = 74.6' },'FontSize',16);

%%-----------------------------------------------------Store Waveform Figure
cd(['/Users/mandalin/Desktop/Dissertation/LindDissertationDocument/',...
    'LindDissertation/Chapter-4/Figures'])
```

```
filename=strcat('BTMWaveform_Mic203_Edge2_Spec.eps')
print(filename,'-depsc')
cd('/Users/mandalin/Documents/MATLAB/BTM Confirmation')
save('simulated_diffracted_outputs_203_Edge2_Spec.mat','Y_203',...
    'time_aligned_time_203','IR_Scaled',...
    'delay_between_incident_and_diffracted')
```

Vita

Amanda B. Lind

Contact@AmandaLind.com

EDUCATION

Penn State, Graduate Program in Acoustics, State College, PA
M.S., Graduate Research Assistant, Doctoral Candidate
Emphasis in architectural acoustic modeling, auralization, and outdoor sound

University of Miami, Coral Gables, FL
B.S. in Electrical/Audio Engineering, May 2007
Emphasis in speech, acoustic signal processing and C++

POSITIONS HELD

Criterion Acoustics (Consultant), Jersey City, NJ
Acoustic Consultant: January 2017 - Present
Calculations, acoustic simulations in 3rd party software, authoring of Matlab scripts to guide and optimize architectural design.

Skybuds, New York, NY Acoustics/DSP R&D: July 2017 - October 2017

Zoox (Consultant), Menlo Park, CA (remote) Acoustic & Audio Systems Consultant: June 2017 - Present External Design Review

Symmetry Labs (Consultant), San Francisco, CA (remote)
Audio Developer (Consultant): November 2016 - Present Combined open source music feature extraction libraries. Communicated real time music features to Symmetry Labs LED pattern generation software.

Zoox, Menlo Park, CA Project Lead, Acoustic/Audio Engineer: Nov 2014 - Oct 2016 Single handedly created a proof of concept prototype; a purpose built multichannel audio communication system with a beautiful UI in 4 months. Acoustic design was guided by Matlab simulation. Demoed the system to investors 4x per week. Incrementally hardened the design with a small team. Executed schematic design through PCB layout in Altium, and coordinated fabrication and assembly. Contracted and coordinated mechanical engineering facets. Selected a DSP Platform -TI TMS320C6747. Wrote firmware and signal processing algorithm in Embedded C. Integrated in a closed loop with a sensor suite and AI stack and tuned latency.

Arup, San Francisco, CA Acoustic Consultant: April 2013 - Nov 2014 Acoustic analysis of 10+ Apple Retail stores and Apple campus. Executed acoustic measurements, some designed in house, others to verify compliance with legislation. Efficient creation of binaural and ambisonic auralizations of spaces from blueprint or 3d model. Experimented with binaural audio with head tracking for Google Glass.

Trade The News, New York, NY Chief Audio Engineer: May 2012 - April 2013 Vocal talent tuning, studio expansion, & maintenance of an investment advice radio station.

PATENTS Inventor on two Zoox patents: Application Numbers: 14/756,993(pending) and 9,630,619(granted)